BRAIN IMAGES ANALYSIS FOR SDH AND EDH TRAUMA CLASSIFICATION

Ph.D. THESIS

by

SOUMI RAY

DEPARTMENT OF ELECTRICAL ENGINEERING
INDIAN INSTITUTE OF TECHNOLOGY ROORKEE
ROORKEE- 247 667 (INDIA)
NOVEMBER, 2018

BRAIN IMAGES ANALYSIS FOR SDH AND EDH TRAUMA CLASSIFICATION

A. THESIS

Submitted in partial fulfilment of the requirements for the award of the degree

of

DOCTOR OF PHILOSOPHY

in

ELECTRICAL ENGINEERING

by

SOUMI RAY

DEPARTMENT OF ELECTRICAL ENGINEERING
INDIAN INSTITUTE OF TECHNOLOGY ROORKEE
ROORKEE- 247 667 (INDIA)
NOVEMBER, 2018

©INDIAN INSTITUTE OF TECHNOLOGY ROORKEE, ROORKEE-2018
ALL RIGHTS RESERVED

INDIAN INSTITUTE OF TECHNOLOGY ROORKEE
ROORKEE

CANDIDATE'S DECLARATION

I hereby certify that the work which is being presented in this thesis entitled "**BRAIN IMAGES ANALYSIS FOR SDH AND EDH TRAUMA CLASSIFICATION**" in partial fulfilment of the requirements for the award of the *Degree of Doctor of Philosophy* and submitted in the Department of Electrical Engineering of Indian Institute of Technology Roorkee, Roorkee is an authentic record of my own work carried out during a period from January, 2013 to November, 2018 under the supervision of Dr. R.S. Anand and Dr. Vinod Kumar, Professor, Department of Electrical Engineering, Indian Institute of Technology Roorkee, Roorkee and Dr. Niranjan Khandelwal, Professor and Head, Department of Radiology, Postgraduate Institute of Medical Education and Research, Chandigarh, India.

The matter presented in this thesis has not been submitted by me for the award of any other degree of this or any other Institution.

(SOUMI RAY)

This is to certify that the above statement made by the candidate is correct to the best of our knowledge.

(Niranjan Khandelwal)	(R. S. Anand)	(Vinod Kumar)
External Supervisor	Supervisor	Joint-Supervisor

The Ph. D. Viva-Voce Examination of **Ms. Soumi Ray**, Research Scholar, has been held on 8th April 2019.

Chairman, SRC **External Examiner**

This is to certify that the student has incorporated all the corrections in the thesis.

Signature of Supervisors **Head of the Department**

Date:

This thesis is dedicated

To

My parents

Mrs. Rashmoni Ray

&

Mr. Jagabandhu Ray

And

To my sweet little baby

পোঁটলু

aka

Sabuj

Abstract

Imaging is a potential way to preserve accurate information of a sense at a particular time for repetitive observation and analysis in future. Clinical brain imaging captures the information about actual condition of brain and presents it in pictorial form for observation. Brain hemorrhage is a common disorder with high death toll. As per Indian Head Injury Foundation report, every year 100000 lives have come to an end due to brain hemorrhage. An effective medical support system is, thus, in high demand to gain clinical control over hemorrhage by reducing the death rate and the pain of survivors with disabilities. In developing countries like India, Computed Tomography (CT) imaging is the majorly used scanning modality because of its cost and speed. Though different mathematical models are reportedly established for automatic or semi-automatic computation for hemorrhage detection and classification using CT images, better works are still in demand for commercialization. A commercially available Computer Aided Diagnosis (CAD), if used in different hospitals, will create homogeneous reports which will be easy to exchange and compare.

This research work is focused to support medical system by designing a CAD for hemorrhage detection and classification of Epidural Hemorrhage (EDH) and Subdural Hemorrhage (SDH). To make the CAD useful and acceptable, our objectives are as follows:

(1) Developing a simple but highly accurate system.
(2) Making the system affordable i.e. the implementation cost must be low.
(3) Designing fully automatic system, so that it can be used for
    (a) Mass screening during emergency,
    (b) In absence of practitioners for initial diagnosis,
    (c) To get lower subjectivity and no tiredness.
(4) Sensitivity of the system must be high enough to make the decisions of machine acceptable.
(5) Designed CAD must offer reliable and dependable performance.

Outline of the entire research work is presented as follows. The analysis of images involves segmentation, feature extraction and classification. Segmentation is done in two steps. In the first step the region of interest (ROI) which is the brain area encapsulated within skull is extracted from head scan images. In the second step, hemorrhage is segmented from diseased affected ROIs. As different hemorrhage has different shape, using the shape features hemorrhages are classified. Results of each step are discussed and compared with recently reported potential research outcomes.

Image analysis depends on features which are extracted from descriptors of the target image. Commonly used image features are color, shape and texture features. For easy and quick information extraction, a single threshold based binary descriptor is proposed. From this descriptor, three major

binary image features called Information Packing Factor (IPF), Compactness (C) and Porousness (P), and two auxiliary features Scatterness (S) and total pore area (w) are calculated to handle multi-slice brain image dataset. These features describe the availability and spared of foreground information of an image and are useful for the purpose of brain CT image indexing. These are used in different steps of the research to improve CAD performance.

To narrow down hemorrhage search area, the brain region is segmented from head scan image. In the pre-processing stage dataset cleaning and arranging in anatomical order are done. Dataset cleaning is done by removing images having no significant brain information. Pore count and IPF feature have efficiently handled this requirement. Using stereo matching the cleaned dataset is arranged in expected anatomical order. Image with maximum brain area in the pre-processed dataset is selected as master image to create mask for brain segmentation. Two masks are created by automatic seed point finding and region growing method. One covers only the intracranial area of master image and another includes its skull area too. The larger mask is used as global mask for the dataset, but the smaller one propagates as adaptive mask. First, it segments the brains of the adjacent images of master image; then it is redefined by adjacent area search and used to segment the next adjacent images. This method efficiently segments the brain image dataset with 98.17% accuracy and 100% sensitivity.

The extracted brain images are considered as input for hemorrhage segmentation process. To locate the threshold intensity for the hemorrhage, brain image histogram and expected histogram are considered. The expected histogram is the intensity distribution which is calculated from actual histogram history. Threshold intensity of an image is found by locating the crossover point, addressed as ‘upset point’ in this thesis, between actual histogram and expected histogram. The threshold intensity search is kept limited in the region beyond the maximum intensity of brain histogram. Normal dataset are removed to reduce load on system. Segmented images of a dataset are fused linearly to locate highest potential area which is then converted into a mask for hemorrhage segmentation. Proposed method has reported average accuracy as 93.19%, average sensitivity as 93.47% and dice coefficient as 92.05% which are much higher than other popular methods. The potential of this method is its speed, accuracy and sensitivity. The higher dice co-efficient of end result has proved that the upset point separates hemorrhage from brain matter without much loss.

Segmented hemorrhages are classified in two steps using decision tree classifier. Initially the target classes are separated from other hemorrhages. Target class is then classified into EDH and SDH. For better performance of classifier secondary shape features are calculated from primary features and, to reduce input load on classifier, feature selection is done using their separability index. Target classes are separated from other hemorrhage types with 100% accuracy. EDH and SDH dataset are also classified with 100% accuracy. Each image of a dataset is classified. The class which contains more images is considered as the class of that dataset. The important observations of the described classification technique are listed below.

(1) Target hemorrhage classes stay in the immediate vicinity of brain boundary. This single feature is strong enough to separate them from other classes

(2) Secondary shape features have more potential than primary shape features for classification because of their higher dependency on object shape.

(3) IPF and compactness have demonstrated noticeable strength in classification of EDH and SDH.

The proposed CAD has significantly high accuracy in segmentation and classification. No false negative result is reported in any step of the entire process. This feature has made the system highly sensitive and dependable for commercial use. The proposed CAD can handle any size of dataset for hemorrhage inspection and classification, even when the scanned images are not in the expected anatomical order. The research target has achieved successfully and the journey has offered some useful bi-products which can also be used for other brain disease detection. The significant bi-products are the master image selection technique, arranging CT images in anatomical order and upset point finding.

Acknowledgment

I would like to take the chance to express my gratitude to my supervisors, Dr. Vinod Kumar, Professor of Department of Electrical Engineering, Indian Institute of Technology Roorkee for giving me a chance to be a part of his laboratory, where I got the association with beautiful minds like Dr. Subramanya M. B., Dr. Padma Ganasala, Dr. Ashok K. Dohare, Dr. H. Nagendra, Dr. Arun Balodi, Shanti Chanda, Prachi Sharma, Ashish Rohila and Gaurav. This journey without their support would have been impossible. I have no word to thank Dr. Nishant Jain for his continuous support in all technical and non-technical issues since the day of our introduction.

I was fortunate to associate with Dr. R. S. Anand who was initially chairman of my Student Research Committee (SRC) and became my supervisor after the retirement of Dr. Vinod Kumar. Irrespective of the type of association, he was always helpful and supportive since my days of course work. I am grateful to my external supervisor, Dr. Niranjan Khandelwal, Professor, Department of Radiology, and his team from Postgraduate Institute of Medical Education and Research (PGIMER), Chandigarh for their support and co-operation by providing medical images, interpretations and medical perspectives for the present research work. I am very much thankful to my student research committee members - Prof. Indra Gupta, Department of Electrical Engineering and Prof. R. Balasubramanian, Department of Electronics and Computer Engineering for their valuable evaluation at each stage of Ph.D. research.

I would like to express my sincere thanks to all the faculties, non-teaching staffs, office staffs and technical staffs of laboratories who always remained supportive and helpful. I sincerely acknowledge the co-operation and support of Mr. Dinesh Sharma, Biomedical Instrumentation Laboratory, Mr. Ameer Ahmed, departmental workshop and Mr. Rishav Verma of Department officials. My heartfelt gratitude to Prof. Indra Gupta, Prof. Biswarup Das, and Prof. Pramod Agarwal for their guidance, patience, care and support which have helped me to overcome all unwanted, unexpected difficulties at different levels during my studentship. Because of them, the campus became the second home for me.

Moreover, admission in full-time Ph.D. program in Indian Institute of Technology Roorkee meant, to be able to stay amongst the lush green, beautifully organized campus. My designated quarter in the year-old D.S. Barracks was my favorite home with its high ceiling, large windows and a long balcony. It is an ideal place for research. I was lucky to get a chance here, away from pollution and population, crowd and noise for a few years in my life. I am thankful to the Ministry of Human Resources and Development and to the institute for this once in a lifetime opportunity, added with a stipend, to lead a peaceful life during my research days here.

I would like to acknowledge, Dr. Apurba Ghosh, University Institute of Technology, Burdwan, West Bengal and late Prof. Satyabroto Sinha, Indian Institute of Technology, Kharagpur, as a constant source of inspiration and motivation in my life. Their support and faith in my capability increased my self-confidence to move ahead with challenges.

I must mention the name of the duo, my college friends, who are very close to my heart and my standby powers for all odd conditions, software professional Oishee Pal and young entrepreneur Soumy Sarkar. They are my mental strength. Because of them only, I was able to handle the toughest days in the last few years and came out safe. I am lucky and blessed to have two such real friends. Another software professional, Mitu Roy who always tries her best to help me in all adverse situations, deserves a salute for her tireless proofreading of most of the chapters and articles even in odd times. I am also thankful, for his valuable time, to Dr. Tanmay Ghosh, my childhood friend, who has enriched my knowledge by sharing his expertise in radiology.

I am thankful to the teachers of my school, Midnapore Mission Girls' High School, West Bengal, who taught me to follow my dream and to work hard to achieve success honestly. Since the starting of my career, neglecting the lucrative salary of corporate sectors, I continued in research and academics because of my passion for learning. The urge to know more, the hunger for perfection, the zeal for innovation and research, were cultivated in me by my parents who educated me to be responsible, balanced, passionate and dedicated in life. Without their sacrifices and dedication, love and affection, I could never think of studying the highest degree in such an esteemed institute. Their honesty and selflessness are the benchmarks of my life.

Before concluding, I must thank all of them who helped me to become more confident, strong and organized by creating negative and difficult situations in this journey.

SOUMI RAY

INDEX

ABSTRACT i

ACKNOWLEDGEMENT v

LIST OF FIGURES x

LIST OF TABLES xiii

LIST OF ABBREVIATIONS xiv

Chapter 1: INTRODUCTION **1-21**

1.1 Preface 3
1.1.1 Importance of medical imaging 4
1.1.2 Neuroimaging 5
1.2 Motivation 6
1.2.1 Brain hemorrhage 6
1.2.2 Computed Tomography (CT) 8
1.3 Image computation 9
1.3.1 Feature extraction 9
1.3.2 Result analysis 11
1.4 Literature review 12
1.4.1 Reported works 13
1.4.2 Research gaps 16
1.5 Objectives 17
1.6 Database 18
1.7 Thesis outline 19
1.8 Conclusion 20

Chapter 2: BINARY IMAGE FEATURES **23-47**

2. 1 Motivation 25
2.2 Available Image features 26
2.3 Proposed Features 29
2.3.1 Information Packing Factor 30
2.3.2 Information Compactness 30
2.3.3 Image Porousness 32
2.3.3.1. Advanced analysis of porousness 33
2.4 Methodology 33
2.4.1 Pre-processing of images: 33
2.4.2 Information extraction 34
2.5 Performance Analysis 37
2.6 Discussion 44
2.7 Conclusion 46

Chapter 3: BRAIN SEGMENTATION **49-74**

3.1 Introduction 51
3.2 Database and CAD outline 52
3.3 Methodology 53
3.3.1 CT image intensity distribution 54
3.3.2 Pre-processing of data 55
3.3.2.1. Skull thresholding 56
3.3.2.2. Dataset cleaning 57
3.3.3 Master image selection 58
3.3.4 Arranging images 59
3.3.5 Automatic Seed point definition 60
3.3.6 Mask Area Definition 61
3.4 Result 64
3.4.1 Skull thresholding and dataset cleaning 64
3.4.2 Master image selection 65
3.4.3 Arranging images 66
3.4.4 Seed point & Mask 67
3.4.5 Segmentation 68
3.5 Result analysis 68
3.6 Conclusion 73

Chapter 4: HEMORRHAGE SEGMENTATION **75-95**

4.1 Introduction 77
4.2 Methodology 79
4.2.1 Segmentation of hemorrhage by population histogram 80
4.2.2 Removal of normal dataset 84
4.2.3 Fusion and Mask definition 87
4.3 Result 89
4.4 Discussion & Conclusion 95

Chapter 5: EDH & SDH CLASSIFICATION **97-120**

5.1 Introduction 99
5.2 Image Features 101
5.3 Hemorrhage features 105
5.3.1 Shape features 105

5.3.2 Additional features 106
5.3.3 Derived shape features 108
5.4 Feature optimization and classification 111
5.5 Conclusion 117

Chapter 6: CONCLUSION **121-127**

6.1 Introduction 123
6.2 Research potential 123
6.2.1 Proposed features 123
6.2.2 Image pre-processing 124
6.2.3 Hemorrhage segmentation 125
6.2.4 Classification 125
6.3 Limitations 126
6.4 Future works 126
6.5 Closing note 127

PUBLICATION 129

APPENDIX A 131
B 135
C 141

REFERENCES 145

List of Figures

Figure 1.1:	Diagnosis practices	4
Figure 1.2:	Imaging planes (a) axial, (b) coronal and (c) sagittal	6
Figure 1.3:	Computed tomography	9
Figure 1.4:	Confusion matrix and derived parameters	12
Figure 1.5:	(a) research work flow, (b) segmentation steps visualized	21
Figure 2.1:	(a) & (b) Compact information, (c) Scattered information	31
Figure 2.2:	(a) Sea, land and islands (b) Land with volcanic crater	34
Figure 2.3:	(a) Information extraction process, (b) Feature tabulation chart	35
Figure 2.4:	(a)-(b) Binary image of 2.1 (a)-(b) - the Compact information, (c) Binary image of 2.1 (c) - the Scattered information (d) Binary image of 2.2 (b) - the Porous information	36
Figure 2.5:	(a) Brain MR scan image and (b) its binary equivalent image	39
Figure 2.6:	(a)-(c) Features plot for MR dataset 1 and (d)-(f) Features plot for MR dataset 2	40
Figure 2.7:	(a) Skull removed brain CT scan, (b) its equivalent image and (c) Sull image	41
Figure 2.8:	Features plot for CT dataset, in each graph, x-axis is presenting the images and y-axis is presenting the value of respective feature	41
Figure 2.9:	(a) Faulty brain scan (b) Skull removed image	42
Figure 2.10:	Confusion matrix of classification using features extracted from skull removed images	42
Figure 2.11:	Confusion matrix of classification using mixed features from both skull removed and skull images	42
Figure 2.12:	Comparison of features after 90° rotation of image	45
Figure 3.1 :	Process flowchart for segmentation of brain CT scan dataset	53
Figure 3.2:	(a) intensity varies with density in CT image (b) CT image	55
Figure 3.3:	(a) Intensity histogram, (b) Background neglected histogram, (c) Histogram with upper 1/3rd span and skull threshold, (d) Skull removed image, (e) Removed skull part (binary image)	57
Figure 3.4:	Skull threshold finding flowchart	58
Figure 3.5:	Head images with no brain information	59

Figure 3.6:	Skull after thresholding a nasal image	59
Figure 3.7:	Arranging images in expected sequence	60
Figure 3.8:	Binary images of different reference images	61
Figure 3.9:	Splitting an image into 4 sub-images and seed point of each sub-image for region growing	62
Figure 3.10:	Brain segmented by inner masking only	63
Figure 3.11:	CT scan after thresholding	64
Figure 3.12:	(a) Image dataset with master image, (b) Removed images during cleaning (c) Dataset after arranging the images with master image, (d) The graph of change in size before and after arranging the images	65
Figure 3.13:	Seed point location marked by $^{+}$	66
Figure 3.14:	(a)-(b) Inner mask and outer mask of figure 13(a), (c)-(d) Inner mask and outer mask of figure 13(b) respectively	66
Figure 3.15:	Segmented brain for figure 12(a) dataset	67
Figure 3.16:	(a) Holes created during skull removal, (b) Restoration result	67
Figure 3.17:	Dataset used to test potential of cleaning operation	72
Figure 3.18:	Segmented brain images from different method	72
Figure 4.1:	Brain hemorrhage from pathology to radiology	77
Figure 4.2:	CAD process flow	79
Figure 4.3	(a) population of intensity with and without background (b) image under test (c) background threshold (d) background removed image	80
Figure 4.4:	Intensity population distribution of image 1, 2, 3	82
Figure 4.5:	Intensity population for images with hemorrhage	82
Figure 4.6:	(a) PDR and threshold (b) segmented image	82
Figure 4.7:	Thresholding result of normal brain image	84
Figure 4.8:	Vertically divided image	84
Figure 4.9:	(a) Feature array to subsets, (b) Confusion matrix, (c) Selected hemorrhage	85
Figure 4.10:	(a) Original image (hemorrhage is marked by circle) (b) Segmented image (c) Output after morphological operation.	87
Figure 4.11:	Segmented hemorrhage	88
Figure 4.12:	Thresholded images are compared.	90
Figure 4.13:	Comparison of %sensitivity of three methods	92
Figure 4.14:	Comparison of %accuracy of three methods	92

Figure 4.15:	Comparison of dice coefficient of three methods	92
Figure 4.16:	Comparison of average of %sensitivity, %accuracy and %Dice coefficient	93
Figure 4.17:	Comparison of segmentation time (in seconds) of three methods (k value varies for traditional methods, for proposed method it is 2 for both the cases.)	93
Figure 4.18:	(a) Original image (b) Skull removed by threshold 225 (c) Background removed by threshold 100 (d) Adaptive thresholding for skull and background	94
Figure 5.1:	(a) Hemorrhage classes (b) EDH (c) SDH (d) SAH (e) IPH and (f) IVH	100
Figure 5.2:	Cranial meninges	101
Figure 5.3:	Image features	103
Figure 5.4:	Performance of classifier	104
Figure 5.5:	Different hemorrhage shape features (a)-(b) Hemorrhage and ROI spans (c) Hemorrhage area (d) Best fit rectangle (e) Best fit circle (f) Convex hull	107
Figure 5.6:	Skull vicinity	108
Figure 5.7:	(a) Different hemorrhage area with same ROI size, (b) Same hemorrhage area with different ROI size	108
Figure 5.8:	IPF varies with (a) Constant ROI area (b) Constant hemorrhage area	109
Figure 5.9:	Features are compared for different types of hemorrhage	112
Figure 5.10:	Separability	114
Figure 5.11:	Skull vicinity distribution	115
Figure 5.12:	Distribution of potential features for EDH and SDH	117
Figure 5.13:	Confusion matrix of EDH-SDH classifier	118
Figure 5.14:	Confusion matrix of three class classifier	119
Figure 6.1:	Classifier performance (a) Without local_IPF feature, (b) Without compactness feature	124

List of Tables

Table 1.1:	Image features	10
Table 2.1:	IPF, compactness and porousness measure	36
Table 2.2:	In-depth calculation of porousness for each pore	38
Table 2.3:	% accuracy of different confusion matrices of different feature combinations	44
Table 2.4:	Performance analysis	44
Table 2.5:	Performance potential comparison	44
Table 3.1:	Pictorial presentation of TP, absfp, FN, TN	69
Table 3.2:	(a) Analysis of segmentation performance of proposed method on patients' dataset	70
	(b) Analysis of segmentation performance of proposed method on normal dataset	71
Table 3.3:	Comparison of segmentation sensitivity	71
Table 4.1:	Sensitivity, accuracy and dice coefficient analysis of proposed method	91
Table 4.2:	Comparison chart of Shahangian, Bhadauria and proposed methods' results	95
Table 5.1:	Disease category	99
Table 5.2:	Shape features	106
Table 5.3:	IPF of ROI calculation for figure 5.7 images	108
Table 5.4:	Separability of different features	114
Table 5.5:	Skull vicinity value of different dataset	116

List of Abbreviations

2D	Two Dimensional
3D	Three Dimensional
AI	Artificial Intelligence
ANN	Artificial Neural Network
APF	Atomic Packing Factor
BRISK	Binary Robust Invariant Scalable Keypoints
CAD	Computer Aided Diagnosis
CBIR	Content Based Image Retrieval
CCV	Color Coherence Vector
CSF	Cerebrospinal Fluid
CT	Computed Tomography
DICOM	Digital Imaging And Communication In Medicine
EDH	Epidural Hemorrhage
EM	Expectation Maximization
FREAK	Fast Retina Keypoint
GLCM	Gray Level Co-Occurrence Matrix
GLDM	Gray Level Different Matrix
GLN	Gray-Level Nonuniformity
GLRLM	Gray Level Run Length Matrix
HU	Hounsfield Unit
ICH	Intracranial Hemorrhage
IPF	Information Packing Factor
IPH	Intra-Parenchymal Hemorrhage
IVH	Intra-Ventricular Hemorrhage
KNN	K- Nearest Neighbour
LabVIEW	Laboratory Virtual Instrument Engineering Workbench
LBP	Local Binary Patterns
LDT	Local Derivative Pattern
LRE	Long Run Emphasis
LTrP	Local Tetra Patterns
MCMCM	Modified Color Motif Co-Occurrence Matrix
MLP	Multi-Layer Perceptron
MRI	Magnetic Resonance Imaging

MSER	Maximally Stable Extremal Regions
MSP	Mid-Sagittal Plane
NPV	Negative Predictive Value
PPV	Positive Predictive Value
RLN	Run-Length Nonuniformity
ROI	Region Of Interest
RP	Run Percentage
SAH	Subarachnoid Hemorrhage
SDH	Subdural Hemorrhage
SIFT	Scale Invariant Feature Transform
SONAR	Sound Navigation And Ranging
SRE	Short Run Emphasis
SURF	Speeded Up Robust Features
SVM	Support Vector Machine
TIFF	Tag Image File Format
USG	Ultrasonography
wl	Window Level
ww	Window Width

Chapter 1

Introduction

Overview

This chapter lays the foundation of the research work which has been conducted for the degree of doctor of philosophy in the field of *medical image analysis*. “Brain hemorrhage”, which is a common problem with a high death toll, is my research object here. To classify by frequency and severity, epidural and subdural hemorrhages are considered as the target classes for classification in this work. In order to support medical practitioners, several methods for computer based detection and classification of brain hemorrhages are reported by different research groups in the last two decades. Potential and popular research works are reviewed to understand current trends of the research potentials. Different features of gray image with equations are also discussed in this chapter. Result evaluation approach used in this thesis are briefed with equations. The objective of the research work and information about the data used in this research are included in this chapter. The chapter is finally concluded with research methodology discussion and thesis organisation.

1.1. Preface

Medical images offer technical support to the medical practitioners in diagnosis and treatment. Different imaging techniques are successfully established by researchers and engineers to make diagnosis easy, fast and more accurate. Image data is considered as more reliable because of its advantage of visual interpretation over descriptive narrations or signal information. Each and every human has his/her own explanation style, interpretation capability and imagination power. Same disease is described in different ways by different patients. Same description creates a different interpretation in different practitioners. In case of an image, the information available in pictorial format is replica of actual physical condition of the disease stage. It reduces the ambiguity. Other advantages of imaging are easy and fast understanding of the information. A long elaborated description of few pages can be presented in a standard postcard size image which is much easier to read, understand, handle and exchange. These are the reasons for which imaging has gained high importance in medical practice. Medical images are technically different from normal images. Normal images use visible lights to capture photo, whereas medical images are captured using invisible range of electro-magnetic frequencies. It is an advanced stage of photography.

In general, the image is a pictorial presentation of any sight and a combination of shades which can be gray or colorful. It can be a painting drawn by an artist or a photograph captured by camera. Potential of imaging technique lies in preservation of a scene or sight in analogue or digital format, exchangeability with others and use of captured scene for information analysis. Painting is a very old technique which has been modified and advanced with human evolution. The oldest image, still found, is the cave painting in El Castillo cave in Spain[1]. As per scientists' prediction, those paintings were made around 40,000 years ago. Capturing of sights as photo is quite new with respect to painting. The first photo which was captured using a camera was taken by Nicephore Niepce in 1822 [2]. That earliest known surviving photograph was taken by exposing the photographic plate to light for around eight hours. Due to fast development of technology, present day's photography has reached some other dimension. Digital photographs are now the most common form of photos.

1.1.1. Importance of medical imaging

In medical imaging, using modern techniques, photography of inner body structures which are not visible in bare eyes is possible. Such information is very important for better treatment and accurate diagnosis. In medical science, doctors are taught to understand different symptoms some of which are visible in normal eyes, rest are described by patients in term of different levels of discomforts. Depending on those symptoms, doctors suggest test(s) if required for better diagnosis. Previously there was no option of imaging of internal parts of body. Depending on doctors' knowledge and pathological tests diagnosis took place. After invention of X-Ray technique the scenario has been changed. Then gradually different other imaging technologies emerged and established their potential through successful contributions in medical science. Now a wide range of medical imaging modalities are available to image the anatomy, physiology or functionality of different parts of human body.

Using different imaging technologies like analog x-ray, digital x-ray, Computed Tomography (CT) scanning, nuclear imaging, Magnetic Resonance (MR) imaging or ultrasonography (USG) imaging inner structures, muscles, blood flow, vessels can be imaged. Though x-ray dominates the medical imaging segment [3], each imaging modality has its own advantages and limitations. Experts' eyes can identify the abnormalities from images and thus a better diagnosis can be offered. Even early stages of different diseases can be detected by proper analysis of medical images. Medical imaging technology can be considered as the third eye of doctors which help them in deeper understanding.

Practitioners detect a disease and its severity by analyzing patients' described symptoms, pathological reports and medical image information. This process is pictorially simplified in figure 1.1. The practice of this process is called diagnosis. Treatment to heal or control a disease completely depends on proper diagnosis.

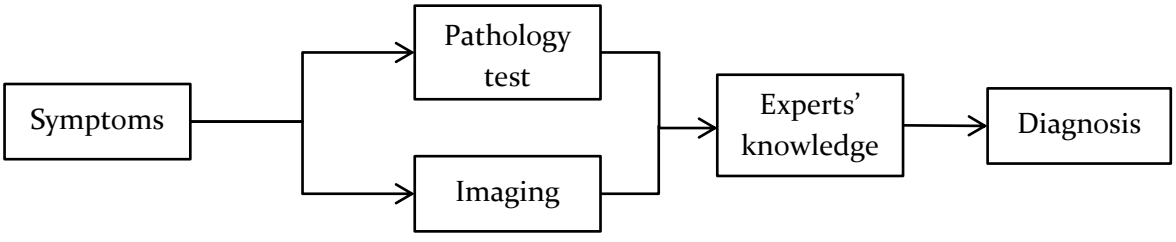

Figure 1.1: Diagnosis practices

Researches are carried out for the advancement of imaging techniques as well as of analysis process to extract more useful and valuable information. Digital images which are either acquired digitally or converted from analogue are used for research purpose. A digital image is a collection of pixels which are the smallest detectable unit of a digital display. A three dimensional scenario is stored in sequential rectangular two dimensional spaces, pixels of which contain equivalent color and intensity information of their respective location in the three dimensional space. For computation, each two dimensional digital image is converted into a two-dimensional numerical array, elements of which correspond the color and intensity information of respective pixels. Total Number of pixels in an image varies with the size and resolution of that image. A large size, high resolution image requires higher number of pixels to store all the information. During analysis these pixel information which are stored in an array can be computed mathematically to extract different features of the image. Medical images are mostly gray scale images. Each pixel of a gray scale image contains the intensity information of the respective location in terms of numeric value ranging 0 to 255.

1.1.2. Neuroimaging

Medical images are captured through scanning. When any body part is scanned, area under projection is saved as image. With movement of scanner, several layers are recorded one after another. When brain which is spherical in shape, is imaged the result offers complex pattern. Along with traditional scanning systems, some hybrid imaging techniques are also proposed by researchers for more information, specially for brain [4, 5]. To capture the complete brain, several cross-sectional images are taken in sequence at a predefined gap. Nasal bones and orbits get scanned at base level of skull where the pattern of information distribution is quite complex. As brain contains soft tissues, CT scan, instead of traditional x-ray, and MRI offer very good imaging results. Each modality has some benefits over another. Choice of the modality depends on different parameters. It has been discussed in details later in this chapter.

Neuroimaging can be of two types – structural imaging, functional imaging. In structural imaging anatomical details of brain are captured. The diagnosis of brain injury, trauma, strokes etc. is supported by structural images.

In functional imaging the functionality of a target area is scanned. It can be blood flow, metabolism, local chemical reaction etc. To record functionality normally contrast agents are injected. Contrast agents are radioactive substrates which are transmitted through blood purposefully to enhance image contrast at target area. fMRI needs no external agents and so less harmful than other methods.

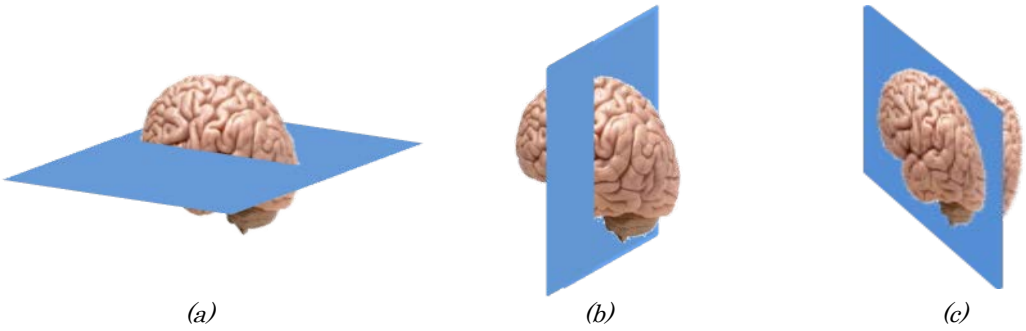

Figure 1.2: Imaging planes (a) axial, (b) coronal and (c) sagittal

Brain can be scanned in three different planes – axial or transverse plane, coronal plane and sagittal plane as shown in figure1.2. Scanner moves from start to end of a particular plane to capture images of different layers. A conventional CT scanner scans brain mainly in axial plane and other planes are reconstructed from recorded axial images. It come with digital recording system in which received information is stored as image. CT has sufficiently high resolution to examine extent of trauma, find its location and type of tumors.

1.2. Motivation

A discussion with practitioners about different diseases reveals that brain hemorrhage, a common and fatal problem with high death toll, is still suffering from diagnosis difficulties. An automatic diagnosis support system can help to improve the situation by escalating the treatment.

1.2.1. Brain hemorrhage

Hemorrhage is a Greek word which is adopted in English dictionary. It is actually a combination of two words - 'hamia' (blood) and 'rhegnunai' (burst). A clinical condition when due to rupture in one or more blood vessels blood is accumulated within local vicinity is referred as hemorrhage [6]. An intracranial bleeding is clinically identified as brain hemorrhage. The word 'intracranial' itself signifies physical location of the hemorrhage. Intra means 'within' and cranial means related to cranium i.e. 'skull'.

Intracranial Hemorrhage (ICH) is an unfortunate incident. Each year, brain injuries, the main reason for hemorrhage, account for thousands of deaths and a significant number of people suffer temporary and permanent disability [7]. The rate of head injury in India is very high and as per Indian Head Injury Foundation, it is the highest in the world [8]. Here, more than 100000 dies every year and over 1 million suffer from serious issues due to head injuries. Human intracranial content consists of 80% brain, 10% blood and 10% cerebrospinal fluid. The mean intracranial pressure in a normal human is 10 mmHg. Because of leakage, blood takes up space and increases intracranial pressure. Among several reasons, the most common reason for 'brain injury' is 'head injury' due to accidents, though every head injury is not necessarily a brain injury. Statistics says that, in India, more than 50% brain traumatic injuries are caused by road accidents [9]. In accidental cases, bleeding in the brain usually occurs at the time of injury. However, symptoms such as headaches, nausea, vomiting may develop immediately or progress gradually over time depending on the severity of the impact. People lacks normal neuronal potential for response as brain injury affects the communication network [10]. Symptoms of general hemorrhage cases can arise anytime and do not last for long in preliminary stages, but with time get worse. Immediate medical care should be sought for the patients not fully awake after an injury. Some hemorrhages can be treated by medication, some may require neurosurgery to remove blood clots and relieve pressure on the brain to save lives.

In India, 1 out of 6 trauma patients dies, whereas in the United States the proportion is only 1 out of 200 [11]. Radiologist per hospital sometimes is not sufficient to attend all the cases on time. In remote areas, availability of radiologist during emergencies is questionable. On contrary, accurate measurement and flawless detection of hemorrhage are not easy for non-specialist radiologists and practitioners [11]. We also cannot neglect the human error factors due to fatigue, rush or some other reasons. To overcome those difficulties a fast, easy to use, sufficiently accurate and fully automatic method for detection of hemorrhage is proposed in this thesis. Using this method a commercial Computer Aided Diagnosis (CAD) system can be developed to support clinical diagnosis system. The advantages of CAD can be listed as -

1. Mass screening, instead of one by one screening, will be possible if multiple numbers of systems remain available in a hospital. It will be very helpful

for any unfortunate incident like bus or train accident or major natural calamities like earthquake, landslide etc.

2. Fast detection with increased accuracy and reduced subjectivity will be possible as everything will be done automatically by the machine after scanning the subject.

3. Mass effect i.e. displacement within brain due to hemorrhage is now implicit by visual understanding of radiologist. This can be improved and standardized by the use of a CAD.

4. Hospitals using same CAD will have homogeneous reports.

5. Hospitals with CT machine but no field expert will be able to offer initial diagnosis to accelerate treatment.

1.2.2. Computed Tomography (CT)

"Tomo" and "graphia" are Greek prefix and suffix. Tomo means "slice" and graphia means writing or describing.

Our brain is composed of different layers of tissues. The entire target is considered as a combination of several thin slices as shown in figure 1.2. Each slice contains different layers, each of which has different attenuation coefficient for x-ray. During scan, every slice is examined from different angles to gather maximum information. The captured information of each slice is then converted into a two dimensional image by inbuilt mathematical model of the scanner. Multi-slice scanner can scan multiple slices at a time. Gap between two slices is called pitch. Intensity distribution and understanding of non-contrast CT images are discussed in details in chapter 3.

In detection and diagnosis of hemorrhage, CT imaging modality plays very important role because of its speed, low cost [12] and capability of capturing reasonably good contrast images for precise investigation [13]. This painless imaging offers information about soft tissues, blood vessels, CerebroSpinal Fluid (CSF) as well as bone with clear distinguishable boundaries. CT imaging is less sensitive to movements [13] and widely available in hospitals, even in rural areas. It has advantages over MRI for the patients having ferromagnetic or electrical implants or claustrophobia. MRI also suffers from thermal noise and long scanning time [14]. Hemorrhage patches are captured as bright distinguishable homogeneous areas within the brain in a CT image. No other disease offers similar

artifacts creating any confusion in observation. These benefits of CT scanning make the choice of imaging modality easier [15-18]. Considering these practical advantages, our work remains limited to CT brain image only.

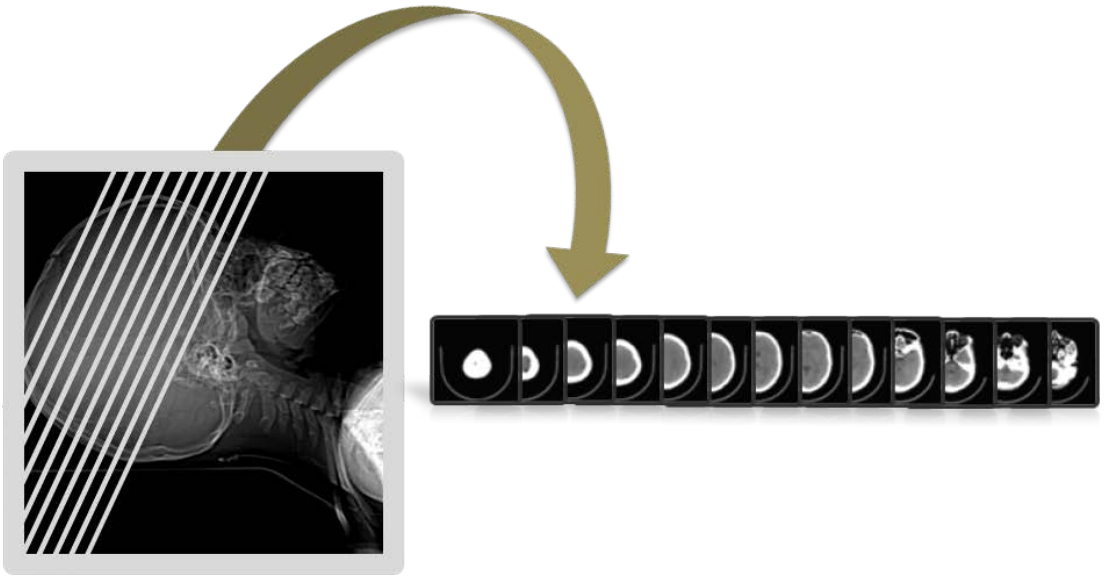

Figure 1.3: Computed tomography

1.3. Image computation

For mathematical computation of an image, array operations are performed on the equivalent array of an image under test. Any image contains two significant types of data – background and foreground. Foreground data contains information about the target object, whereas background represents the base on which the image is displayed. For any analysis the foreground part is important; but background also supports the computation process indirectly.

1.3.1. Feature extraction

To understand an image systematically, different description values are calculated from image body. These descriptive parameters are called features. Features help to distinguish one image from another depending on dissimilarity. Commonly used features for brain CT image analysis are texture features and shape features. Texture epitomizes the intensity distribution pattern of the image surface. Direct evaluation of image pixel intensity results into primary texture features like mean, standard deviation, kurtosis, skewness etc. A deeper analysis for better understanding is conducted to evaluate higher order texture features. Relative intensity value of an image pixel is considered for higher order

calculation. These relative values explore the intensity changing pattern of the field of distribution. Gray Level Co-Occurrence Matrix (GLCM) [19] and Gray Level Run Length Matrix (GLRLM) [20] are some popularly used derived matrix for higher order feature extraction. Few of the commonly used features in medical image analysis and the associated mathematical formulae are collated in table 1.1.

Features extracted from periphery of an image are identified as boundary features. Different edge detection techniques are used to extract boundary features [21-23]. Encapsulation pattern of an image is exclusively extracted by boundary features. Similar images with different backgrounds can be classified based on their boundary features. Shape parameters describe the spread of an image. Features like major axis, minor axis, best fit circle, equivalent circle etc. measure the geometrical pattern of target. These features are discussed in details in chapter 5 of the thesis.

Primary Features	
Mean	$= \frac{1}{MN}\sum_{i=1}^{M}\sum_{j=1}^{N} I(i,j)$
Variance	$\sigma^2 = \frac{1}{(MN-1)}\sum_{i=1}^{M}\sum_{j=1}^{N}[I(i,j)-\mu]^2$
Standard deviation	σ
Skewness	$\frac{1}{MN}\sum_{i=1}^{M}\sum_{j=1}^{N}\frac{[I(i,j)-\mu]^3}{\sigma^3}$
Kurtosis	$\frac{1}{MN}\sum_{i=1}^{M}\sum_{j=1}^{N}\frac{[I(i,j)-\mu]^4}{\sigma^4}$
Energy	$\frac{1}{MN}\sum_{i=1}^{M}\sum_{j=1}^{N}[I(i,j)]^2$
*M*N is the image array size, i, j are two variables denotes image pixel position at any instant.*	
Secondary features	
GLCM	
Entropy	$-\sum_{i=1}^{N_g-1}\sum_{j=1}^{N_g-1} p(i,j) * \log(p(i,j))$

Dissimilarity	$\sum_{i=1}^{N_g}\sum_{j=1}^{N_g}\|i \quad j\|p(i,j)$
Contrast	$\sum_{n=0}^{N_g-1} n^2 \left\{ \underbrace{\sum_{i=1}^{N_g}\sum_{j=1}^{N_g} p(i,j)}_{\|i-j\|=n} \right\}$
Homogeneity	$\sum_{i=1}^{N_g}\sum_{j=1}^{N_g}\frac{p(i,j)}{1+\|i \quad j\|}$
Correlation	$\sum_{i=1}^{N_g-1}\sum_{j=1}^{N_g-1}\frac{(i \quad \mu_x)(j \quad \mu_y)*p(i,j)}{\sigma_x\sigma_y}$
Autocorrelation	$\sum_{i=1}^{N_g}\sum_{j=1}^{N_g}(ij)*p(i,j)$
Sum Entropy	$-\sum_{i=2}^{2N_g} p_{x+y}(i)*\log\{p_{x+y}(i)\}$
N_g represents number of available gray levels. μ_x, μ_y and σ_x, σ_y represents mean and variance of p_x and p_y.	
GLRLM	
SRE (short run emphasis)	$\frac{1}{n_r}\sum_{i=1}^{M}\sum_{j=1}^{N}\frac{p(i,j)}{j^2}$
LRE (long run emphasis)	$\frac{1}{n_r}\sum_{i=1}^{M}\sum_{j=1}^{N}p(i,j)*j^2$
GLN (Gray-level nonuniformity)	$\frac{1}{n_r}\sum_{i=1}^{M}\left(\sum_{j=1}^{N}p(i,j)\right)^2$
RLN (Run-length non-uniformity)	$\frac{1}{n_r}\sum_{j=1}^{N}\left(\sum_{i=1}^{M}p(i,j)\right)^2$
RP (Run percentage)	$\frac{n_r}{n_p}$
P(i, j) is (i, j)th entry in gray level run length matrix, n_r is total number of runs and n_p is the total number of pixels	

Table 1.1: Image features

1.3.2. Result analysis

The result obtained through any proposed method should be evaluated to understand the system's performance. Validation is done by quantitative measure

of success of a system. Four major parameters which can define a system's acceptability are sensitivity, specificity, positive predictive value (PPV) and negative predictive value (NPV). A simple observation table is used to demonstrate easy evaluation of these parameters. This table is called confusion matrix or error matrix. This matrix contains basic information of system performance from which validation parameters are computed. Input and output information of a system are divided into two parts. One part is the target and another is non-target. The input that presents the target part is called Positive information, rest is identified as Negative information. At output, part of result which satisfies the ground truth is marked as 'True' outcome and rest are as 'False' outcome. This concept is presented in matrix form in figure 1.4. Derived features to evaluate system performance are also presented in the extended wings with mathematical equations.

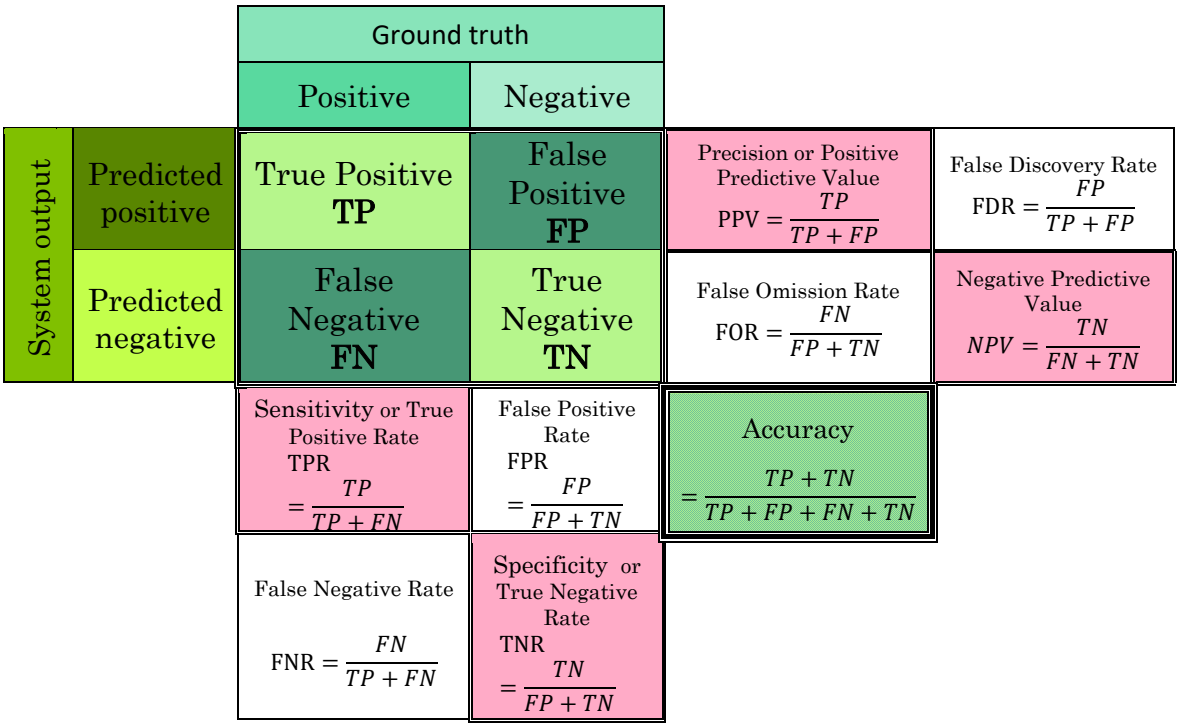

Figure 1.4: Confusion matrix and derived parameters

1.4. Literature review

In the process of identification and classification of hemorrhage from CT brain images, major challenge is accurate segmentation of target from head image dataset. Segmentation method involves two major steps. First step identifies the intracranial part in an image as Region Of Interest (ROI). In the second step, the hemorrhage is identified within the ROI and segmented for classification. A brain

CT image contains information about soft tissue, blood vessels, cerebrospinal fluid, skull, soft tissue edema (if any), air and sometimes the headrest too. Skull and headrest show highest intensity of pixels whereas CSF and air show lowest intensity of pixels. Blood vessels, soft tissue, skin etc. have an overlapping intensity of pixels and are not easily distinguishable. For accurate, errorless computation through a computer, removal of objects having no clinical information is very important. Higher intensity skull and headrest are also removed to reduce computational complexity and thus increase efficiency. The literature survey is reported in an organized way. First, I have summarized the research articles about intracranial part segmentation. Reported articles about hemorrhage segmentation are considered separately and followed by the articles about hemorrhage classification to understand the status of research in the present scenario.

1.4.1. Reported works

Several computer aided diagnosis systems for brain image analysis and hemorrhage diagnosis are designed and presented in different research articles for decades. Though brain CT images are very important clinically, number of reported works on segmentation of brain from CT images is not very large [24, 25]. Majorly MR images are evaluated for analysis and segmentation of different brain diseases [26]. Though limited, but in some research works, brain CT images are segmented into different objects [27] and then analysis of each object is carried out by feature extraction [17] to identify the target. Skull and brain matter extraction from CT images, is reported in a number of articles as a part of image pre-processing for disease identification [28-30] or disease patch segmentation [24, 31-34]. From CT images, extraction of brain area which is affected by target disease, using thresholding, region growing, Mid-Sagittal Plane (MSP) finding, supervised and unsupervised methods - are reported by different research groups during different times as discussed below. During survey it has been noticed that, shape guided segmentation methods are not much explored for brain disease extraction from CT images [35].

Thresholding and region growing methods are old, easy, simple but fast methods. It is not a very potential one for segmentation of complex regions with overlapping or very close intensity level. Thresholding can be done to segment

entire image into two segments, one is above the threshold and the other is below the threshold. The pixels having the threshold value can be combined with any of the segments. A modification can be done by multi-thresholding [36] approach, in which more than two segments can be extracted. The threshold can be user defined [28, 31] or automatically adapted from the image [24].

Region growing method offers good accuracy for abnormalities like hemorrhage which have significant intensity difference from surroundings. Satisfactory results are reported in different CT segmentation works using region growing technique [37-39]. Region based hemorrhage segmentation with good accuracy has been reported by few researchers, [31, 40-43] in the last few decades. This technique works based on pixel intensity or edge information. The major disadvantage of this method, in case of automation, is the requirement of expert's interaction for seed point definition.

Most of the MSP finding techniques depend on brain symmetry [44-47]. It suffers from non-negligible error in case of the midline (the bright line in CT image to segment brain into two hemispheres) shifting due to disease severity. This method requires user interpretation and the computation time is also large [48]. Liu et al. and few others proposed a hemispheric symmetry detection approach to detect brain lesions [28, 49-52]. In some literature, midline shift is considered as a positive indicator for hemorrhage [28, 50]. On contrary, EL Yuh et al. calculated that midline shifting is a supportive finding to establish the existence of hemorrhage [53]. This method checks the symmetry for each slice and any abnormal region at one side referred as hemorrhage.

Supervised techniques are popularly implemented for segmentation of target region using area based classification. Supervised methods require training data preparation by domain experts. Large and versatile database is required during training, to avoid overfitting problem of the system [54]. This training process and data requirement makes supervised methods slow and difficult [55]. Paying the cost of the complex algorithm, unsupervised segmentation techniques like k-mean segmentation [56], expectation maximization [57], fuzzy C-means algorithms [58] can be used. For unsupervised method, parameter initialization overwrites the requirement of training data set.

Hemorrhage finding is mostly done by locating threshold on the histogram. Threshold identification is done automatically through artificial intelligence using

different algorithms like fuzzy C-means [18, 59], Hopfield neural network [60, 61], 2D entropy [18], fuzzy maximal likelihood estimation [43], probabilistic neural network [59], genetic algorithm [41]. To detect hemorrhage few more approaches like - knowledge based detection [32], histogram-based K-means clustering [62], wavelet-based texture analysis [63] are also proposed in the literatures. Comparatively less number of researches have reported unsupervised clustering and backtracking tree search method [64, 65]. As hemorrhage is detected by searching hyperdense region within the image [62], no image registration is required; but still, one research paper has presented image registration between two hemispheres [28]. Pre-processing of images using morphological operation [28], and median filter [18, 42] have included in few research works to enhance accuracy in the final outcome.

In recent time, deep learning methods are also in use for abnormality segmentation [66-69]. Most of them are supervised techniques which require a large dataset. This requirement itself is a disadvantage of these methods [55, 70]. Different deep learning techniques are also outperformed by the traditional k-means method used in an unsupervised system which involves a limited data [71].

Due to higher similarity in intensity dependent surface information of different types of hemorrhage, impact of texture features in brain hemorrhage classification is not useful. On the contrary, shape features have shown good potential because of physical form and size difference between classes. Several researchers have reported success in classification of brain hemorrhage, segmented from CT image, with high accuracy using shape features as classifier input [24, 40, 57, 72]. For hemorrhage classification, different studies are reported the use of decision tree [72, 73], Support Vector Machine (SVM) [74, 75], Multi-Layer Perceptron (MLP) [76], K- Nearest Neighbour (KNN) [77], K-means and Expectation Maximization (EM) [57] methods.

To understand the underlying difficulties and to bridge the gaps between expectations and achievements, in hemorrhage segmentation and classification, the most relevant works reported in the last decade are analyzed. Study of state-of-the-art creates a strong foundation for the research by identifying the available techniques, difficulties in this field and the shortcomings. Work reported by Tianxia Gong et al. [40], classified normal images from diseased with good accuracy, but the accuracy of hemorrhage classification is not much impressive.

They proposed preprocessing of images before segmentation and classification. Skull area was removed during preprocessing of images taking a fixed value as threshold. Brain area was segmented using two fixed threshold values - upper and lower threshold, and taking skull as the boundary. The abnormality was detected by suppressing intensities, which are less than and equal to the intensity of the highest peak in the histogram, to zero. Median of the resulted image was considered to detect hemorrhage. The classification was done with the help of shape features. Quantitative analysis of segmentation is not reported. Bardera et al. [31], proposed a semi-automated method, in which seed point for region grow was selected manually. In this article, an experimentally fixed value was used as stop criteria of growing region with an option of alteration depending on user satisfaction. They had attempted to segment hemorrhage directly from the brain image without any preprocessing. Though the reported results were promising, the method lacked automation and suffered from hard thresholds. Bhadauria et al. [78] introduced a hybrid approach for hemorrhage segmentation. They utilized the advantages of both FCM and active contour methods. Using FCM, they segmented brain images to extract hemorrhagic area. Segmented candidates were used for initializing the level set function. A modified data fitting function was proposed incorporating fuzzy membership matrix. Their method was able to break the limitations of conventional active contour method by adaptively estimating the controlling parameters. This work had demonstrated a significant improvement in performance with respect to region growing and fuzzy clustering technique. In a more recent work, Bahareh et al. [24] used a modified level set method, Distance Regularized Level Set Evolution, which needed no reinitialization. Before implementing the level set function, images were preprocessed to remove skull, ventricle, and soft tissue edema. To remove skull, threshold value is adjusted by trial and error method. For classification, shape features were considered. The work claimed a significant improvement in accuracy over conventional process.

1.4.2. Research gaps

Some research works reported direct segmentation of hemorrhage from dataset. but extraction of the brain region in the preprocessing stage of hemorrhage segmentation is important to reduce the noise and improve the efficiency of the CAD [79]. The method of segmentation varies keeping the central

focus on the fact that it is a homogeneous and bright part in CT images. The deficiencies observed in the available methods are listed as follows;

i. Most of the reported works handle a single 2D CT image at a time, for analysis. The execution steps are repeated for each image of the multi-slice head scan dataset. This process is time consuming.

ii. Handling nasal images from the base of skull is a challenging task. The underlying reason is the porous structure of the skull which includes several large compartments and contains brain information in one or multiple segments. The degree of difficulty has enforced avoidance of the discussion of lesion segmentation from such images, in most of the articles. The connections of intracranial matter with the skull outside soft tissues through paranasal sinuses, suppress the capacity of the skull to isolate the brain from outside. Only in limited number of articles, nasal images are inspected for hemorrhage, using separate analysis process for those images.

iii. Even after advancement of technology, no reliable, low cost CAD system is available for medical support in hemorrhage detection and classification.

We have tried to overcome these gaps in our designed CAD for hemorrhage segmentation and classification.

1.5. Objectives

Hemorrhage can be of several types depending on its location in brain. The major two classes are intra-axial and extra-axial hemorrhage and these are further divided into different subclasses. After discussing with radiologists and studying several papers it was concluded that among all types of hemorrhages, Subdural hemorrhage (SDH), Epidural hemorrhage (EDH) and Intracranial hemorrhage (ICH) are the most common cases received in hospitals [80]. Subdural and Epidural hemorrhage are the major subclasses of extra-axial hemorrhage. Among all types of hemorrhages, these two are very common in accident cases and fatal too. They demand fast, reliable and automatic screening for treatment initialization during emergency. To satisfy this requirement, these two types of hemorrhage have been considered as the research target to develop an automatic

Computer Aided Diagnosis system for detection and classification of the same. The distinct steps followed during research to achieve the goal were as follows:-

(1) Acquiring domain knowledge to understand the brain hemorrhage in CT images.
(2) Brain boundary identification and brain segmentation
(3) Segmentation of hemorrhage
(4) Feature extraction, feature selection and classification.

We put our efforts to develop an advanced methodology to address the gaps in this field. Images from a dataset can be analyzed separately as multiple 2D images or can be handled as a 3D volume. Volumetric analysis, as voxels are considered instead of area, involves higher computational complexity and longer execution time. Consideration of relations between neighbor images in a dataset promotes the potential of 3D analysis in the 2D domain. Our objective is designing a less complex method which will execute the 2D brain images in the dataset and offers results comparable with 3D image analysis results to collapse the heterogeneity between 2D and 3D domains.

Nasal images become unavoidable for volumetric analysis. Independent evaluation of each nasal image also deviate us from our objective. The wish of simultaneous evaluation of nasal images triggers the requirement of intellectual preprocessing of the dataset. Lossless extraction of the brain with less inclusion of non-intracranial area from the base of skull is one of the challenging objectives of this research. Our objective, in short, is to design a highly accurate dependable method, for hemorrhage segmentation and classification, which will bridge the gaps mentioned in section 1.4.2.

1.6. Database

Multiple slice head CT scan of different subjects, both diseased and normal, collected from Postgraduate Institute of Medical Education and Research, Chandigarh, are included in the database. Total 27 patients' dataset and 16 normal dataset are considered for hemorrhage segmentation and classification. For training purpose separate isolated images are used. Each of EDH and SDH case has 50 images, SAH has 31 images and intra-axial hemorrhage case has another 31 images. The number of images of a dataset, under test, varies from 12 to 34 for different subjects depending on practitioner's decision and machine

capability. Some online dataset [81-83] are used in different stages for brain image pattern analysis and training of neural network. Advance CT machines store images in Digital Imaging and Communication in Medicine (DICOM) format which is an international standard for medical images [84]. DICOM images are converted into 8-bit gray scale Tag Image File Format (TIFF) and stored in local computer hard disk for further analysis. Algorithms are developed for complete automation. In this thesis, the word 'dataset' indicates the collection of images of a patient acquired by CT machine during one full length scan. And the entire collection of data used in this work is referred as 'database'. For computation, each two dimensional (2D) CT scan slice of a dataset is considered as a 2D image array, elements of which contain value between 0 and 255.

1.7. Thesis outline

We have pre-processed each dataset to prepare it for actual analysis. All images are converted to array of 512X512. The noise reduction is made by eliminating skull and all extra-cranial objects. The resultant brain matter is taken as ROI for hemorrhage segmentation. Hemorrhage segmentation is done by histogram thresholding and morphological operation. Segmented hemorrhages are classified based on their shape features in two steps. In the first step decision tree removes the non-target hemorrhages to narrow down input volume. In final stage artificial neural network classifier is used to classify target group into EDH and SDH. The flow of proposed method is depicted in figure 1.5.

The actual research work is composed and presented in four main chapters. Total six chapters and necessary appendixes are written to complete the thesis for partial fulfillment of doctoral degree. A brief of each chapter is given below.

Chapter 1: this is the introductory chapter with brief discussion about motivation, image computation techniques, objective of the work and outline of the thesis.

Chapter 2: three binary features, information packing factor, compactness and porousness, are proposed in this chapter. Features are defined, mathematically described, computed and applied on brain CT image data to examine the potential.

Chapter 3: the process of skull encapsulated brain extraction as ROI is explained. Region grow approach with an automatic seed point finding is proposed. Multiple slice dataset is evaluated by two steps masking. One of the masks changes its definition adaptively with progress.

Chapter 4: hemorrhage is segmented from respective ROI by histogram thresholding. The threshold value is computed by comparing actual histogram and expected histogram value from moving average of past. Morphological operation and fusion is used to finalize the hemorrhage location.

Chapter 5: this chapter contains details about derivation of second order shape features from segmented hemorrhage. These features are more relevant to the class of a hemorrhage than primary features. With the help of shape features, decision tree and neural networks classify the database into EDH, SDH and rest of the segmented hemorrhages are tagged as 'other'.

Chapter 6: reported work is summarized and concluded here. Limitations are discussed to foresight possible extension of this research in future.

1.8. Conclusion

Motivation, necessity and objective of this research work are discussed as foundation of the thesis. Information is briefed about CT brain images, image analysis techniques and database used in this research. Literature survey is done to understand the present status of researches in this field. Thesis organization is given at the end of this chapter as a quick reference. In the next chapter, three potential but easy to compute binary images are proposed and discussed.

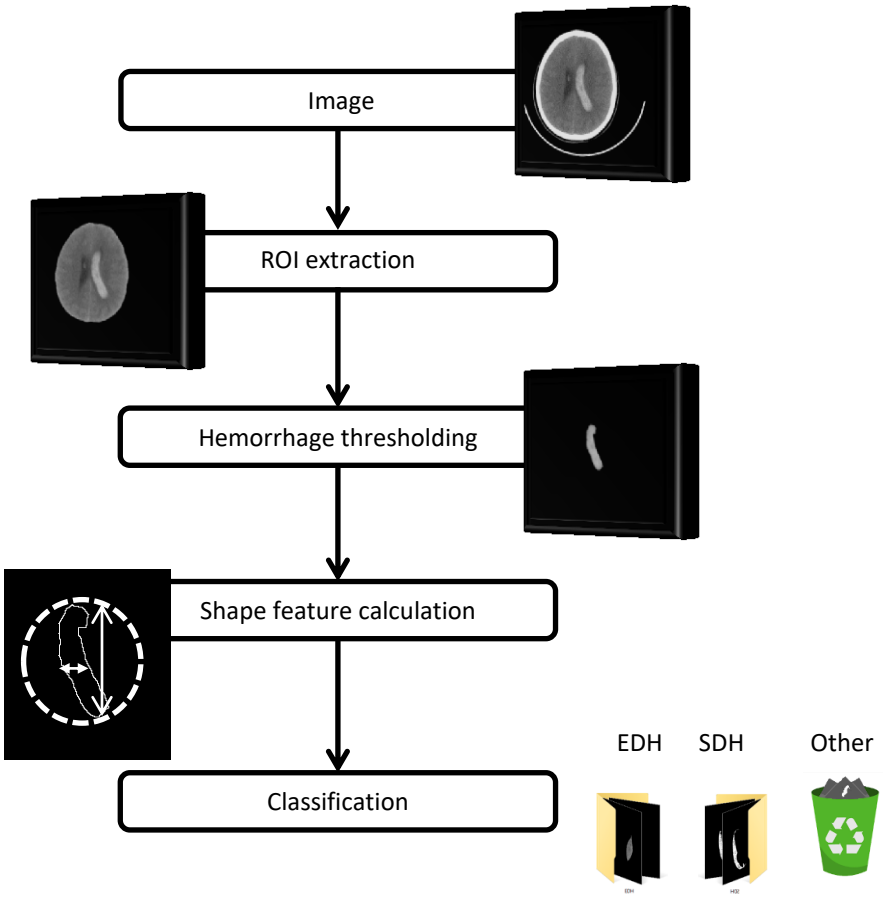

(a)

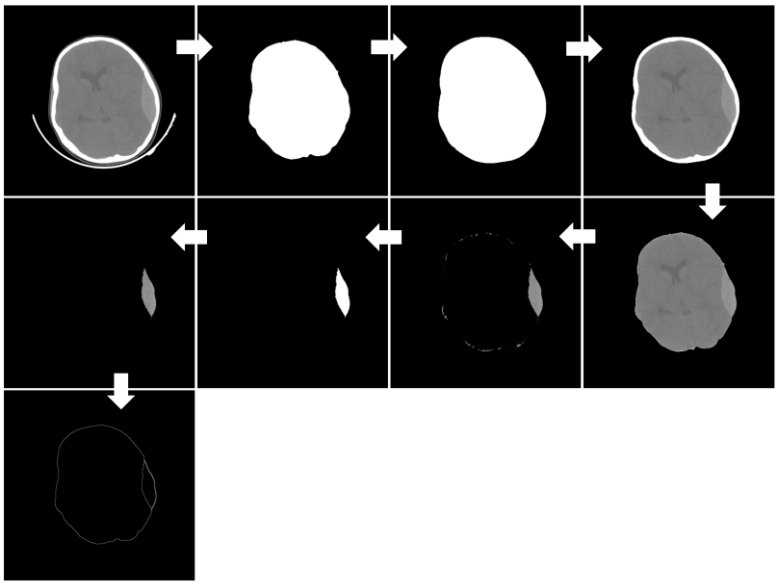

(b)

Figure 1.5: (a) Research work flow, (b) Segmentation steps visualized

Chapter 2

Binary image features

Overview

This chapter presents three fast and easy computable image features to improve computer vision by offering more human-like vision power. These features are neither based on image pixels' absolute or relative intensity informationnor based on shape or color. These are based on the existance and spread of foreground information. To calculate different features, computer needs to scan an image pixel by pixel. It is like seeing an image with maximum zoom. This kind of reading is done by human only when a higher level of details of an image is required. Normally, first we look at an image for overall idea to understand whether it deserves further investigation or not. This capacity of getting an overall idea 'at a glance' is analysed and three basic features are introduced to facilitate computer vision similar capacity with low computational load. Features are proposed and described usning regular images and satellite images. To test and establish the potential and versatility of proposed features in medical imaging domain, different brain image datasets are examined. performance of the features in classification of datasets is compared with reported work. It demonstrates possibilities and potential of the proposed features in image processing to enhance computer vision capacity.

2.1. Motivation

In this research, our target data are brain scan images which are acquired using computed tomography (CT) technique. With advancement in technology, CT machines become capable to acquire large number of slices during scanning. It can be 4, 8, 16, 32 or 64 slices. Even 128, 256 and 320 slice CT machines are also available; but for higher cost they are mainly used for critical diagnosis and research purposes. Normally 32 and 64 slices CT machines are used in hospitals. For detection of hemorrhage, the use of entire dataset of a multiple slice scan is advantageous than inspecting each slice separately. Normally, CT scan is done sequentially from bottom to top of the head. In some cases it is done in reverse order too. So, the resulting images have sufficient correlation in information distribution with adjacent slices. This is a potential feature to improve accuracy in end result of hemorrhage detection.

Though in normal practice, CT scanning is done in a sequence, sometimes re-scanning of certain part is required due to technical faults or practitioners' interest. In such cases, sequence of the saved image may be out of order [63]. Looking at a dataset, a human can easily predict whether it is in order or not. And if it is not in order, out of order images can be identified by visual inspection. Sequential scan also includes complex nasal area images in which brain part gets connected with non-intracranial parts through paranasal sinuses. Intensity and texture features of those parts are very similar with brain part of the image. Sometimes, during sequential CT scan, terminal head part having no brain or having only scalp get scanned and saved in the dataset. Human intelligence automatically can identify these issues and take proper actions to reduce error in further analysis. To do the same pre-processing tasks, a computer needs to calculate several higher order features from each image slice. Only after computing that information it can decide the status of the dataset and classify slices accordingly [85]. The simple task, thus, becomes complex for a computer because of computational load and time consumption. But why computer vision has this problem? In reality, there are several gaps between human and computer vision which need to be addressed [86].

To offer computer a more human like vision, first we need to understand human vision system. Instead of discussing the biological details in depth, a rough

outline of human vision system is given here. Human eyes take image information from surrounding and interpret it to make a sense about the scene. Eyes work like convex lens through which rays pass and create inverted image in focus plane [87]. Our brain nerves then analyze this image and help us to understand. So, basically human eyes read an image of a scene from a distance. Distance varies depending on the type of the scene. During reading of books, newspapers or leaflets distance will be more or less within 1.5 to 2 feet. For landscape it can be anywhere from few feet to infinity (for sky, stars, sun, moon etc.). In all the cases, the inverted images are created in the focus plane of eyes. When we look into any scene, we gather an overall idea about the scenario first, and then observe the details in depth depending on our requirements and interests [88, 89]. On the contrary, a computer always reads an image like reading a datasheet. It reads out each and every pixel sequentially like a scanning machine to gather complete details at first. Required information is extracted later from collected details.

This difference in observation style sometimes put an unwanted computational load on computer during image processing and analysis. Machine vision also lacks the feature of human vision called 'glance'. In this chapter, rather than focusing on fine details of well-known image features like color, brightness, size, shape, boundary and texture, three image features and their computation from a binary descriptor are proposed to empower computer vision with the capacity of extraction of some quick initial facts from an image with low computation load. These features will help to gather overall average information about information distribution within an image.

2.2. Available Image features

Most prominent characteristic of an image is its color [90, 91]. Based on the color of an image, it can be categorized as one of the four major types, binary image, gray image, color image and multispectral image [92]. Binary, gray and color images are visible in bare eyes and easy to understand. Multispectral images are captured through electromagnetic spectrums beyond our perceptual range or using SONAR (SOund Navigation And Ranging) system. The captured information is then mapped into the visible spectrum to enable inspection by human. All medical images fall in this category. Digital color world has several color spaces like RGB (red, green and blue), CIE (International commission on illumination),

HSV (hue, saturation and brightness) [90, 93] etc. Multispectral images are mapped into any of these color spaces. During mapping loss of information happen if the actual image contains higher number of spectral bands than the destination space. Other than color, texture and shape are two major properties which are useful to understand, analysis and classify an image [86, 94-97]. Several valuable features are extracted from all three above mentioned properties of an image to enhance digital vision of a computer or robot.

All available image features can be classified as low level features and high level features based on the type of mathematical models used for feature extraction [98]. Features, directly calculated from image array, using array elements' values, are classified as low level features. High level features are calculated from low level features or from a secondary array computed from the image array. Another popular way of feature classification is based on the target area of an image which is used in extraction process. Here, features are classified in three different categories - pixel level features, local features and global features [98]. Pixel level features are calculated directly from the independent value of image array elements. It can be intensity, color information, location etc. Local features are extracted from region of interest i.e. from keypoints of an image, whereas, for calculation of global features, entire image is taken into account [99, 100]. Some well-known local feature descriptors are Scale Invariant Feature Transform (SIFT) [101], Speeded Up Robust Features (SURF) [102], Local Binary Patterns (LBP) [103, 104], Binary Robust Invariant Scalable Keypoints (BRISK) [105], Maximally stable extremal regions (MSER) [106], Fast Retina Keypoint (FREAK) [107], local derivative pattern (LDT) [108], newly introduced Local Tetra Patterns (LTrP) [109]. Commonly used global features are image mean, image moments, image histogram, texture histogram [110] etc. These features become local when extracted only from target location of an image for survey purpose like object detection, image matching, image stitching etc. Features like histogram [111, 112], moments [113-115], color coherence vector (CCV) [116], color correlogram [117], Gray level co-occurrence matrix (GLCM) [19], gray level run length matrix (GLRLM) [20], modified color motif co-occurrence matrix (MCMCM) [118] etc. have significant contribution in color and gray image processing.

Shape features offer an idea about the shape and size of image or object [119, 120]. Two different types of shape features can be calculated. One is contour based, using which boundary features can be calculated, and another one is region based. In region based technique, the pixels within that shape area are considered for extraction of different features [120].

Tactile qualities of image surface are depicted by texture features of an image [121]. Depending on extraction technique, a texture feature can be structural, statistical, model based or transform feature [122]. Though these features are equally potential for all kinds of images, a significant use of texture features are observed in gray image analysis and classification. In medical imaging field, non-contrast multispectral images are majorly mapped into gray scale images and their texture features are extracted for further analysis and disease detection [123]. Texture and shape features play an important role for disease classification too; because, in maximum cases, the target object i.e. the disease patch in the image changes its shape and size with progress of disease. Statistical texture features are further classified into three categories based on their computation processes, first order, second order and higher order [124, 125]. Higher order texture features offer more details about an image like relative pixel intensity, patterns etc. but first order features are good for basic idea about the image.

Image segmentation and classification are critically depended on efficient feature extraction [126]. Large numbers of features are available for in depth analysis of an image. Simple to complex mathematical calculations are involved in extraction of all these features. For content based image retrieval (CBIR) binary image descriptors are widely used for its computational simplicity and speed [127]. Pixel based features and local features offer better information about part of an image, whereas global features offer an overall idea about the entire image under test. Still the 'glimpse' capacity of digital vision is missing even after some significant efforts which are made towards this direction by finding object boundary, coarseness and different spatial relationship features[88,89,99,100,128].

With advancement of AI, expectations have increased. We expect computer to reflect human perception more accurately in its vision. Human brain analyses an image first by overall condition of the image [88]. The facts observed are mainly

the amount of useful information in an image, image quality and the information distribution. Color, contrast, brightness, identification of objects etc. are being noticed subsequently. It is also observed that global features are very good in scene perception [100]. For example, an image can have information arranged closely or distributed in an unorganized way or arranged in a pattern as shown in figure 2.1(a) to (c) respectively. An idea about image information distribution can be assessed by calculating and combining different higher order texture features like contrast, correlation, energy, entropy etc. But a direct measurement of distribution of information will offer a better human like fast observation power to computer vision.

In the following sections of the chapter, three features are discussed to provide computer a fast 'over all' idea of an image. For simplicity of understanding, color images are not considered in the discussion of this chapter. Only gray scale images having intensity ranging from 0 to 255 are considered here. So, numerical value of array elements will remain bounded between 0 and 255. After discussing the basic concepts of proposed features, methods for extraction of these features from an image are elaborated and followed by the application, mainly in medical image analysis. Qualitative analysis of the results and potential of the features are demonstrated through confusion matrix evolution. In the discussion section, characteristics of each feature are investigated. Details like definitions with formula, range of feature values, programing algorithms for implementation of these features to develop CAD are given in the appendices A and B at the end of the thesis. These features are used to improve CAD performance in different stages of our research. Its potential in enhancement of computer vision, related to our work, is discussed in the subsequent chapters.

2.3. Proposed Features

Any image, technically, has two parts-foreground and background. The foreground contains image information which is useful for further analysis. Rest of the information collectively contributes in formation of image background. Foreground can be continuous as shown in figure 2.1(a) or distributed over the area as shown in figure 2.1(c). Generally image analysis is done by extracting intensity information of each pixel. In this chapter, instead of each pixel, the groups of pixels are considered for feature extraction. The entire image is

converted into two groups of pixels, foreground and background, using a suitable threshold value. Three major features namely information packing factor (IPF), compactness (C), porousness (P), and two minor features namely scatterness (S), total pore area (w), are proposed to get a quick idea about the image under test. In this research, these features are mostly used to pre-process dataset before analysis and increase accuracy of proposed method in different steps.

2.3.1. Information Packing Factor (IPF):

The measure of available foreground information in an image.

In crystallography, there is a term called atomic packing factor (APF) which defines the fraction of volume of a crystal that is occupied by atoms [129]. Using the same concept, information packing factor is proposed here to describe the foreground image information density with respect to the total image size. For a (nXm) image where n is number of rows and m is number of columns of the image array, if total u number of pixels belong to foreground and z number of pixels belong to background, then

$$\text{Information Packing Factor (IPF)} = u / (n \times m)$$

$$\text{And} \quad n \times m = u + z$$

$$\text{So, IPF} = u/(u+z)$$

$$= 1/(1+z/u) \qquad (2.1)$$

When u=0, IPF=0. It means image contains no information. When z=0, IPF=1 i.e. there is no background in the image. When z=u, IPF=0.5 as per equation 2.1. With increase in z, the value of IPF decreases as per the above equations. This simple observation will offer an overall idea about the amount of available foreground information in an image.

2.3.2. Information Compactness (C):

Measurement of tightness in distribution of foreground information in an image.

Another quick observation of human eyes is the spread of foreground within the total available area of image. Images without and with gaps in information distribution are shown in figure 2.1. Figure 2.1(a) has high- compact information. No significant gap is there in the image information distribution.

Such arrangements offer higher compactness value. Figure 2.1(b)-(c) have one or multiple area(s) where there is (are) gap(s) between information. With increase in gaps, compactness value decreases. If all foreground information is placed side by side without any gap, it can be considered as completely compact. The highest compactness value should be 1. If u number of foreground pixels are there in a (nXm) image, and y number of background pixels are placed within the foreground information distribution, then compactness is the ratio of image information to total area covered by foreground information along with in-between background pixels.

$$\text{Compactness (C)} = u/(u+y) \tag{2.2}$$

As y increases with constant u, the numerical value of compactness decreases. With no gap between information i.e. y=0, compactness becomes 1.

(a) *(b)* *(c)*

Figure 2.1: (a) & (b) Compact information, (c) Scattered information [130]

The opposite characteristic introduced by the background pixels which are placed within foreground, can be measured by deducting compactness value from unity which is the maximum possible compactness or by directly taking ratio of in-between background pixels to the total area covered by the same and foreground information pixels. This characteristic is addressed as scatterness in this chapter.

$$\text{Scatterness (S)} = \bar{C}$$
$$= 1 - C$$
$$= 1 - [u / (u + y)]$$
$$= y/(u+y) \tag{2.3}$$

When y=0, equation 2.3 evaluates the value of S as 0. In other words, if compactness is 1, there will be 0 scatterness.

2.3.3. Image Porousness (P):

Measure of background information completely confined within foreground information of an image.

Porousness can be created due to several reasons. It can be due to the nature of the image, due to presence of some information having very close intensity value to background. Generally such non-informative homogeneous parts trapped within foreground are filled by background intensity value which is most commonly 0 or 255 in case of gray images. Each separate confined area is denoted as pore in our work.

It is apparently difficult to differentiate porousness from scatterness. In both the cases, there are background pixels between foreground pixels.

In case of scatterness the gaps are created due to unattached spread of foreground information. Porousness can be identified as the non-peripheral part of scatterness. Pores should have no link with background of the image. It should be completely confined within foreground. To explain, an example of an image of islands in a sea, shown in figure 2.2(a), is taken. In this image, lands are not connected to each other but they are complete on their own. If sea is considered as background then the gaps between islands, due to sea, lower the compactness of the image. This situation offers high scatterness and low compactness measure. Let's zoom into an image of a single island. If we find an unexpected gap in the image of the land, that gap may belong to porousness because a land itself is expected to be continuous. As shown in figure 2.2(b) due to volcanic crater there is an unexpected low intensity area in the land image. Such a view is not normally expected for any landscape or island. This artifact contributes in the measure of porousness.

Porousness is measured as the ratio of background pixels which belong to pore to the total of foreground information pixels and pore pixels.

$$\text{Porousness (P)} = w/(u+w), \quad w \leq y \leq z.$$
$$= 1/(1+u/w) \tag{2.4}$$

Where, w is the total number of pixels belonging to pores or total pore area of the image. Equation 2.4 demonstrates that for no pore the porousness will be zero.

2.3.3.1. Advanced analysis of porousness

As discussed above, pores remain confined within the image foreground area without having any link to the image background. The count of such pores offers the number of porous parts. When w>1, the total porous area can be divided into one or several pores. Each pore contributes to the porous area of an image. Using any established connected area labeling method [131, 132], pore count and volume measurement of each pore can be done.

For an example, if there are q pores in an image which has u numbers of foreground pixel, and pixel count of the pores are w_1, w_2, ….. w_q respectively, then

Total pore area $w = \sum_{i=1}^{q} w_i$

Pore count (n_p) = q

And, porousness contribution P_i of i^{th} pore is

$$P_i = w_i/(u + \sum w_j) \text{ where } j = 1 \text{ to } q$$

$$= w_i/(u + w)$$

So, $P = \sum P_i$ and the range of P_i is same as P.

Sometimes, very fine gaps in compact images also offer porousness. Volume of such pores normally remains very low. This fact has been discussed later in this chapter.

2.4. Methodology

2.4.1. Pre-processing of images

In all above mentioned features, images are considered as a combination of two levels – foreground and background. This assumption leads to binarization of an image. One level contains background information and second level contains foreground information. For a gray scale image, in most of the cases, background color remains black or white. Otherwise, it can be user defined. And any other intensity level, beyond background intensity range, is considered as foreground information.

This binarization can be done by user defined threshold value. Depending on user's understanding, a particular intensity value or a range of intensity values can be selected to divide the image into two pixel groups for further analysis. To do thresholding automatically, any established binary thresholding method [36, 133] can also be used. In this chapter, Otsu bi-level thresholding is used to convert the

gray images to binary images. The threshold calculated by software, is mentioned for each case.

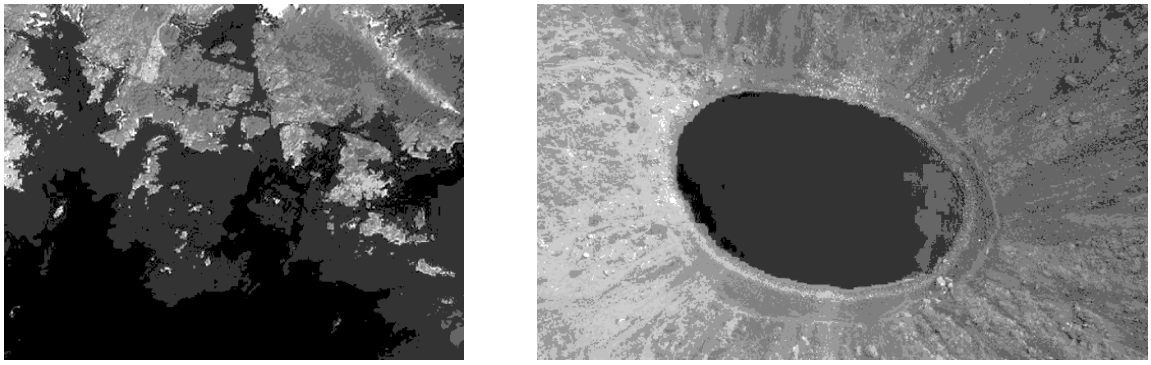

(a) *(b)*

Figure 2.2: (a) Sea, land and islands [134] (b) Land with volcanic crater [135]

2.4.2. Information extraction

For computation, a binary image is mathematically represented by an array of two elements. To keep it simple we have considered 0 and 1 as array elements. 0 presents the background and 1 represents the foreground elements. A binary image array (I) is considered to describe the feature calculation process. The pictorial demonstration is shown in figure 2.3(a). In this array, all 0s are representing background information (BI) location and 1s are presenting foreground information (FI) location. Total length of foreground information spread (L) for each row is calculated from the image array and presented in 'foreground information length' array. Similarly, count of available foreground information per row and background pixels within that are calculated and presented in 'foreground information count' and 'scatterness count' array. From scatterness count array, pore pixels are extracted. The scattered pixels having no background pixel as neighbor are considered as pore pixels. For pore pixel selection 8-connected neighborhood search is taken into account. The details of extraction are highlighted for row3 (R3) of image array. The scattered pixels of R5 and R6 are not contributing in pores. 2nd scattered pixel of R6 has a background neighbor. This particular scattered pixel is neighbor of another scattered pixel of R6 and the scattered pixel of R5. So, none of these three have any contribution in porousness.

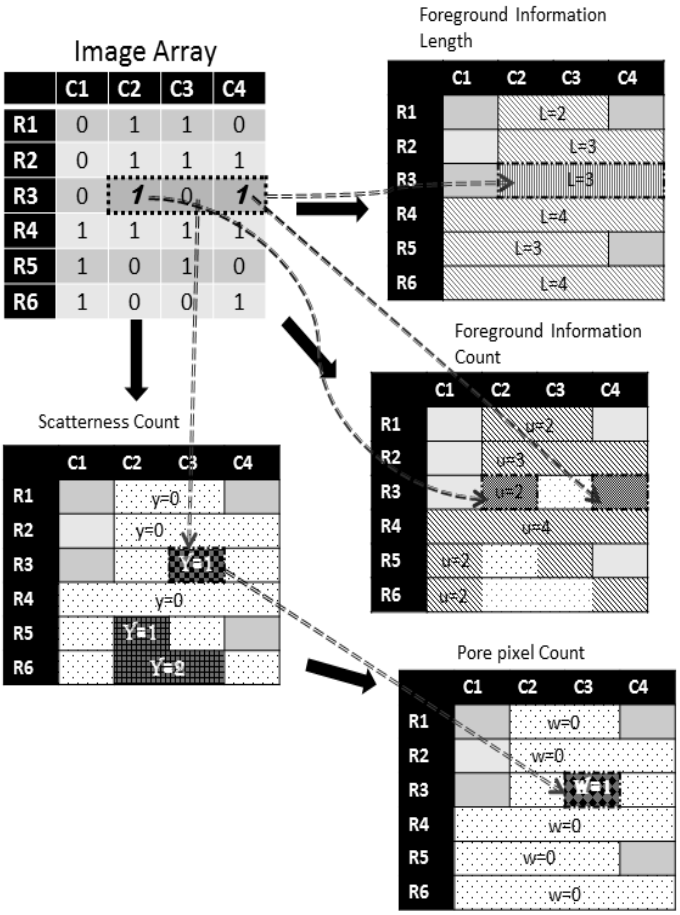

(a)

	C1	C2	C3	C4
R1	0	1	1	0
R2	0	1	1	1
R3	0	1	0	1
R4	1	1	1	1
R5	1	0	1	0
R6	1	0	0	1

Serial number of rows	FI length L_i	FI count u_i	BI count z_i	Scatterness count y_i	Pore pixel count w_i
R1	2	2	2	0	0
R2	3	3	1	0	0
R3	3	2	2	1	1
R4	4	4	0	0	0
R5	3	2	2	1	0
R6	4	2	2	2	0
Total	19	15	9	4	1

image size =24

(b)

Figure 2.3: (a) Information extraction process, (b) Feature tabulation chart

A tabulation chart can be formed from image array for easy calculation of the features. The formation of tabulation chart is presented in figure 2.3(b). This chart provides all information required to calculate the values of IPF, C, S and P.

Images, given in figure 2.1(a)-(c) and 2.2(b), are converted into binary images as shown in figure 2.4(a)-(d) respectively before further analysis. Display images have black (intensity 0) background and foreground is presented in white

(intensity 255). Foreground information intensity value is selected as 255 for presentation purpose only, as 0 and 1 offer no visible significance in digital gray images. Binarization is done by Otsu thresholding. Threshold values selected by Otsu method are 86, 80, 72, 148 for figure 2.4(a) to (d), respectively.

(a) *(b)* *(c)*

(d)

Figure 2.4: (a)-(b) Binary image of 2.1 (a)-(b) - the Compact information, (c) Binary image of 2.1 (c) - the Scattered information (d) Binary image of 2.2 (b) - the Porous information

Image	Image size nXm	Info. Size p	Scatter size q	Total pore area w	Pore count n_p	IPF	C	P
Fig.2.4(a)	786432	197719	27484	3038	29	0.2514	**0.8780**	0.0151
Fig.2.4(b)	786432	**274513**	46127	5871	77	**0.3491**	0.8561	**0.0209**
Fig.2.4(c)	122500	36697	17364	8	4	0.2996	0.6788	***0.0002***
Fig.2.4(e)	26015	20041	5895	5463	114	0.7704	0.7727	0.2142

Table 2.1: IPF, compactness and porousness measure

Table 2.1 shows the IPF, C and P calculation of figure 2.4(a)-(d). Human visual perception at a glance is reflected in this calculation. As per human vision, figure 2.1(b) has highest density of information among first three images. This fact is satisfied as the calculated value of IPF is maximum for 2.4(b). Human perception regarding figure 2.1(a) and 2.1(c) as highly compact and highly scattered respectively, is also reflecting in calculated values of proposed feature shown in table 2.1. Porousness is maximum for figure 2.2(b) among all, and figure 2.1(c) has almost no porousness. Thus all the calculated features are completely satisfying human visual perception.

Area and porousness of each pore can be calculated for every single image. In table 2.2, results for figure 2.4(a) to (d) are presented in descending order. Except for figure 2.4 (c), only highest 11 pores are presented. Rest parts are avoided due to the presence of huge number of very small pores.

The result shows that fine gaps in foreground in a compact image or small gaps due to scatterness sometimes unexpectedly contribute in porousness measurement. But those volumes are too low to be considered as shown in table 2.2. Here, only figure 2.4(d) has a significant pore which is emphasized by bold font in table. The threshold for considerable pore volume must be application specific and can be determined by end users.

2.5. Performance Analysis

Using these features, primary classification of a set of images can be done to reduce complexity and computational load on advanced steps of analysis. IPF presents volume of available information in an image. This is very basic but a required feature. Classification based on information size can be powered by IPF. Compactness (also scatterness) and porousness illustrate distribution of foreground information within an image. Porousness pixels are also counted in scatter counting, whereas all scattered pixels are not necessarily considered during porousness calculation. All these features are extracted from the level of individual pixel intensity with respect to threshold, keeping the computation fast and light weight.

In several applications like medical image processing, satellite image analysis, remote sensing, robotic vision, document processing, automatic inspection etc. feature extraction is required for image analysis, processing and decision making. Knowledge about information density and its distribution will help in almost all the cases to understand images in a better way.

In case of brain diseases like dementia - Alzheimer brain size starts shrinking over time. In a longitudinal brain scan, brain size changes from slice to slice. Using impact of this change, scanned slices can be classified primarily by IPF. In a transverse multi-slice brain scan, brain area in different slice is different. At the base of skull, nasal bones and orbits get scanned and the actual brain area becomes low in the image. Scanning, generally, starts from this level and gradually moves towards the top of the head. Approximately at the middle of

the scanning range, lateral ventricle level of brain is scanned. Scanned slices are automatically saved in the scanning order by computer. Close observation shows that this order of scans offers a particular pattern to IPF, compactness and porousness volumes. Two healthy brain transverse MR scan dataset are collected from open-source internet database [81, 82] to perform a test. Background threshold values are selected by Otsu method. One scan image and its binary equivalent are shown in figure 2.5(a) and 2.5(b) respectively. The variation of IPF, C and w of a MR dataset are shown in figure 2.6(a)-(d) and the same of another in figure 2.6(e)-(h).

Image	Pore count n_p	Pore area per pore (pixel count)	% Porousness per pore	Image	Pore count n_p	Pore area per pore (pixel count)	% Porousness per pore
Fig.2.4(a)	29	2011	1.0020	Fig.2.4(c)	4	3	0.0082
		385	0.1918			2	0.0054
		317	0.1579			2	0.0054
		141	0.0702			1	0.0027
		36	0.0179				
		32	0.0159				
		21	0.0105				
		19	0.0095				
		15	0.0075				
		14	0.0070				
		5	0.0025				
Fig.2.4(b)	77	1473	0.5254	Fig.2.4(d)	114	**5190**	20.35
		1137	0.4055			27	0.1059
		827	0.295			20	0.07842
		527	0.188			15	0.05881
		500	0.1783			7	0.02745
		320	0.1141			7	0.02745
		304	0.1084			6	0.02353
		180	0.0642			6	0.02353
		159	0.05671			6	0.02353
		95	0.03388			6	0.02353
		83	0.0296			6	0.02353

Table 2.2: In-depth calculation of porousness for each pore

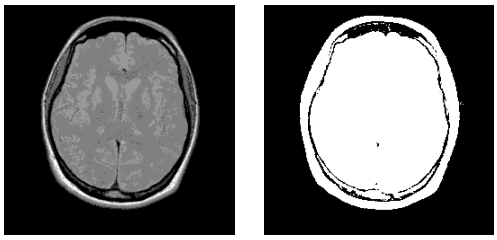

(a) (b)

Figure 2.5: (a) Brain MR scan image [81] and (b) its binary equivalent image , threshold value is 70

Another dataset of 32 slice brain CT of normal subject, collected from internet archive site [83], has been used for further investigation. The collected dataset is pre-processed to remove the skull. The image of one skull removed CT scan and its binary equivalent are shown in figure 2.7(a)-(b). Removed skull image, shown in 2.7 (c), is the by-product of this process. Skull removed images are taken to extract IPF, compactness, porousness and pore area. Extracted values are plotted and shown in figure 2.8(a)-(d). The main difference in MR and skull removed CT images, is that the intensity value for lateral ventricle is high for MR but fall in the range of background for CT.

IPF and compactness remain always higher for ventricle level brain slices where largest area of brain is captured during scanning. Porousness is high for slices at the base of the skull where eyes are included in scan and lower for the rest. In this CT dataset, the last slice displayed in figure 2.9(a), is showing very high porousness. The binary equivalent of skull removed image of figure 2.9(a) has no brain but background trapped within a circular brain like patch as shown in figure 2.9(b). This CT image contains no brain information in reality. For further analysis of porousness, average pore area of CT dataset is calculated by using the formula stated in equation 2.5. The plot of the same is shown in figure 2.8(e). Error is significantly amplified in this plot and very easily recognizable.

$$\text{Average pore area} = w_{avg} = w/n_p \tag{2.5}$$

To explore the potential of the proposed features, classification of brain CT scan dataset is performed using IPF, compactness (C) and porousness (P). Total 729 CT scan slices in which 226 slices are of nasal area i.e. have brain as well as eyes in scan, 441 slices have brain only and 62 slices have no brain in head scan as shown in figure 2.9(a) have been used. The dataset is collected from free online data source [83]. Complete set is classified using Neural Network Pattern Recognition (nprtool) toolbox of Matlab. A subset of 55% of entire dataset is

utilized to train the network and testing is performed on 35% of dataset volume. The combined classification accuracy presented by all confusion matrix of figure 2.10, is 94.2%.

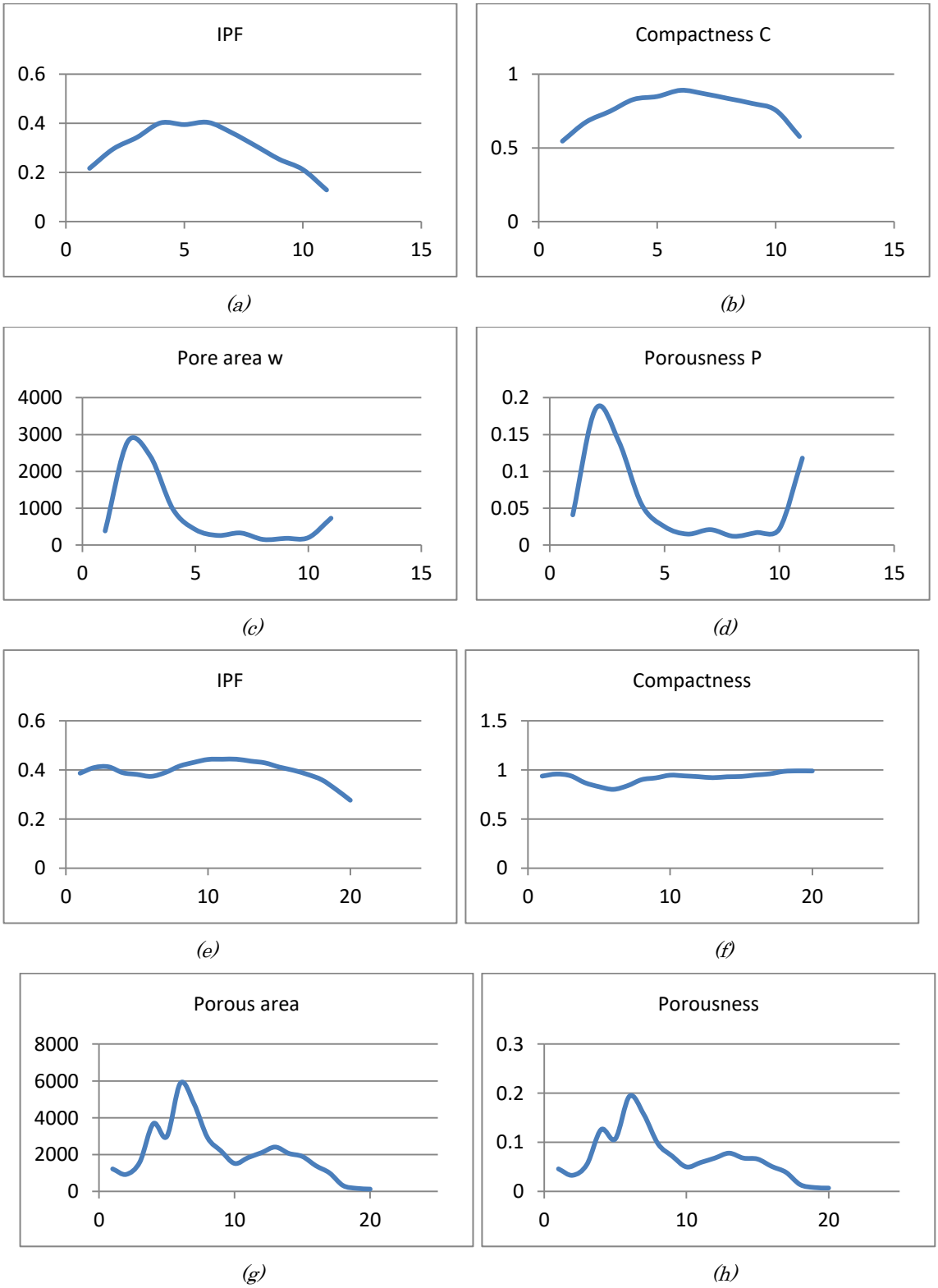

Figure 2.6: (a)-(c) Features plot for MR dataset 1 and (d)-(f) Features plot for MR dataset 2

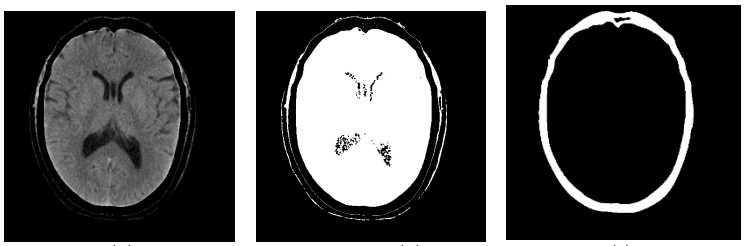

(a) (b) (c)

Figure 2.7: (a) Skull removed brain CT scan [83], (b) its equivalent image and (c) Skull image

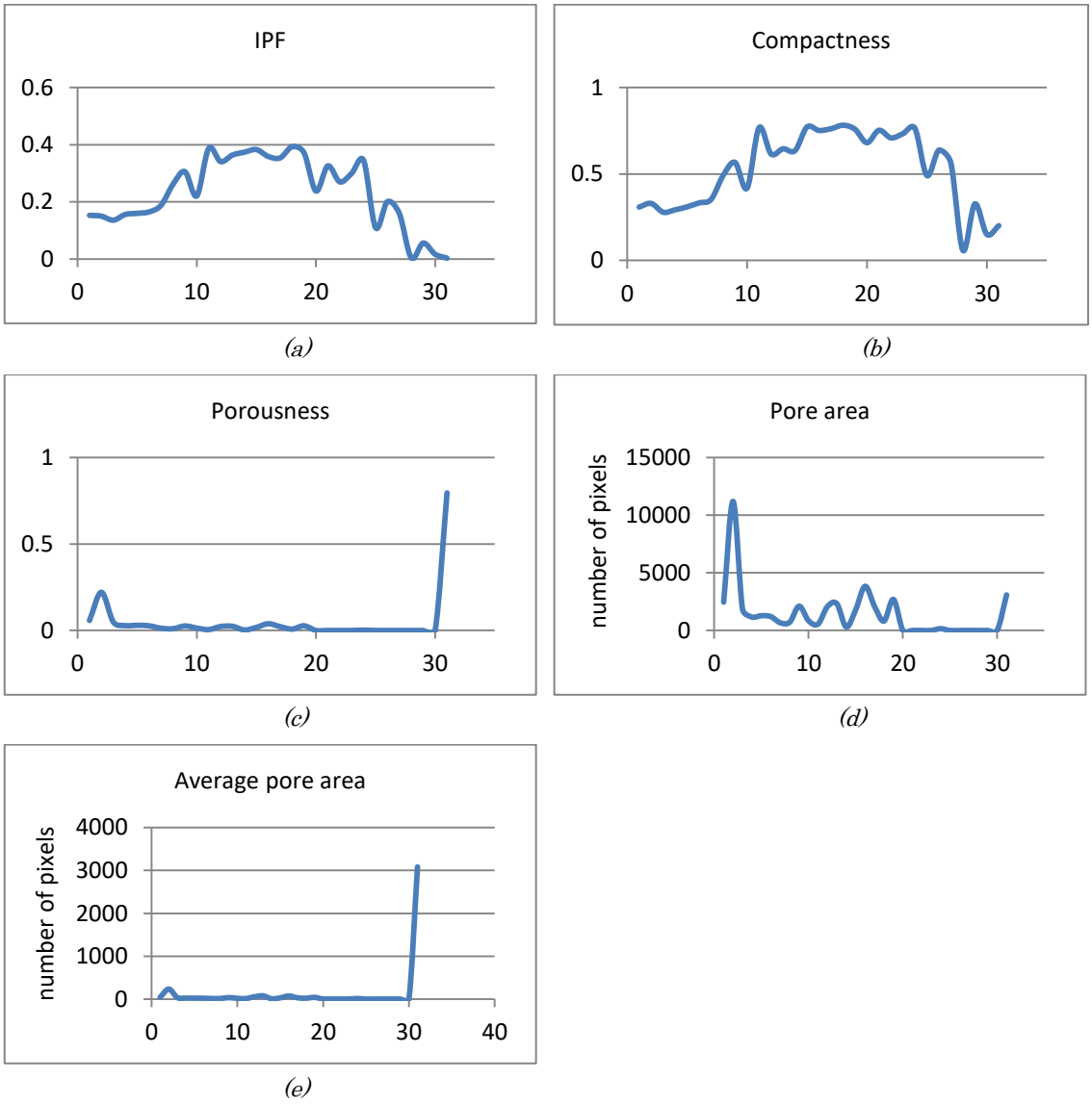

(a) (b) (c) (d) (e)

Figure 2.8: Features plot for CT dataset, in each graph, x-axis is presenting the images and y-axis is presenting the value of respective feature

The classification accuracy increases when porousness values of skull removed images are replaced by corresponding porousness value of skull images. The classifier performance for this input combination is presented in figure 2.11. The overall accuracy has increased to 95.9%.

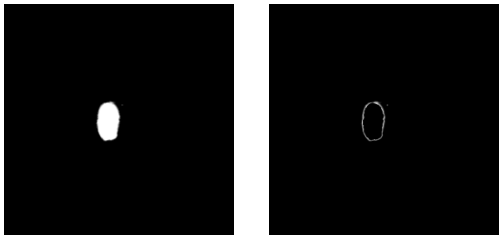

Figure 2.9: (a) Faulty brain scan [83] (b) Skull removed image

Figure 2.10: Confusion matrix of classification using features extracted from skull removed images

Figure 2.11: Confusion matrix of classification using mixed features from both skull removed and skull images

To classify this database in the above mentioned three classes, more features can be included in different combination to observe the change in classification accuracy. Along with IPF, C and P, pore count n_p and porous area w are also included in input. The input feature combinations used to check classification potential are as follows:-

Combination 1 [C1]: IPF, C, w

Combination 2 [C2]: IPF, C, w, np

Combination 3 [C3]: IPF, C, w, P

Combination 4 [C4]: IPF, C, w, np, P

Every time, randomly a subset of 55% of complete dataset has been used for training and 35% of dataset has been left for testing of trained neural network. For each combination, 10 test results are collated in table 2.3. The standard deviation offers an approximate overview of classification potential of each neural

network. When the neural network classifies all subsets with almost equal potential, the standard deviation remains low. The performance observations of different networks for different combinations are as follows:

- C1 has demonstrated poor performance in classification with respect to other three combinations, though smallest standard deviation is achieved.
- C2 also offers reasonably low standard deviation between classification accuracies in more than one cases.
- C3 and C4 demonstrated very similar performance with good classification potential.
- Maximum accuracy obtained in training set classification is 100% by C4. The same network offers 96.5% overall accuracy but a poor standard deviation.
- Maximum accuracy obtained in overall classification is 97.9% by C3 with reasonably low standard deviation.

C3 and C4 can be considered as powerful combinations as per the observation table.

A large number of input combinations are possible from these 5 features. Any feature set can be replaced by its corresponding feature set obtained from skull images. End users can determine the best suitable combination for their specific applications. The best performing network obtained from those combinations can be saved for further use.

The performance of this work, reported in figure 2.11, is evaluated and presented in table 2.4. It shows significant improvement in brain CT image classification with respect to the most similar work reported by Liu et al. [85]. Using shape and other features, Liu et al. had proposed a method of indexing. This method suffers from the mathematical burden of complex feature extraction and rotation correction. To evaluate their proposed method they used 80 CT image dataset which had 446 nasal slices, 802 brain slices and 311 top slices. The comparison result is collated in table 2.5. A significant improvement in classification is noted.

	C1				C2				C3				C4			
	Training	Test	All	Std. Dev.	Training	Test	All	Std. Dev.	Training	Test	All	Std. Dev.	Training	Test	All	Std. Dev.
1	94.9	90	93	***2.02***	87.2	92	87.3	***2.24***	97.4	98	97.9	***0.26***	97.4	96	97.2	***0.62***
2	87.2	68	80.3	***7.94***	93.6	88	91.5	***2.31***	69.2	70	68.3	***0.69***	100	94	96.5	***2.46***
3	89.7	78	85.9	***4.87***	92.3	82	89.4	***4.34***	93.6	96	95.1	***0.99***	94.9	86	92.3	***3.74***
4	85.9	80	81	***2.58***	74.4	76	74.6	***0.71***	94.9	86	91.5	***3.67***	89.7	84	88.7	***2.49***
5	66.7	60	63.4	***2.74***	73.1	68	72.5	***2.28***	98.7	92	96.5	***2.79***	69.2	70	69	***0.43***
6	96.2	96	95.8	***0.16***	74.4	66	72.5	***3.60***	70.5	60	66.9	***4.36***	96.2	92	95.1	***1.78***
7	78.2	70	75.4	***3.40***	92.3	88	90.8	***1.78***	94.9	96	95.8	***0.48***	89.7	82	87.3	***3.22***
8	84.6	82	83.8	***1.09***	97.4	86	93	***4.69***	92.3	90	91.5	***0.95***	62.8	72	67.6	***3.76***
9	94.9	96	91.5	***1.92***	89.7	90	90.1	***0.17***	91	76	83.8	***6.13***	96.2	92	93.7	***1.72***
10	91	72	84.5	***7.88***	97.4	80	91.5	***7.23***	94.9	96	95.8	***0.48***	97.4	94	95.8	***1.39***

Table 2.3: % accuracy of different confusion matrices of different feature combinations

Index	***Precision %***	***Sensitivity %***	***Specificity %***	***Accuracy %***	***F-score %***
1	*94.67*	*92.21*	*97.75*	*96.08*	*93.42*
2	*96.13*	*97.39*	*94.12*	*96.08*	*96.75*
3	*100*	*100*	*100*	*100*	*100*
Avg.	*96.07*	*96.08*	*95.79*	*96.46*	*96.07*

Table 2.4: Performance analysis

Method	***Precision %***	***Sensitivity %***	***Accuracy %***	***F-score %***
Liu et al. [85]	79.73	81.42	86.58	80.22
Proposed method	**96.07**	**96.08**	**96.46**	**96.07**

Table 2.5: Performance potential comparison

2.6. Discussion

Images with usable information are processed by users to extract required data. In this chapter 'usable' information is identified as 'foreground' information after image binarization. If an image has no such usable information, user needs not to process it. So, practically an image under process must have some foreground information i.e. u>0; though theoretically it can be zero. In appendix A, the theoretical and practical ranges of all proposed features along with their definitions and calculations are summarized.

To calculate the features, entire image is converted into two levels based on the value of absolute intensity of each pixel in the image. Pixel having intensity

equal to or higher than the threshold value, receive membership of 'foreground' level and labeled as 'high'. Rest are assigned to 'background' and labeled as 'low'. After conversion, pixel intensity values are not used for further calculation. To keep the system simple and fast only the membership labels are considered. Image features are standardized as first order, second order or higher order depending on their extraction methods. First order features are calculated from absolute pixel intensity values. Second and higher order features are extracted from relative intensity values of pixels. Proposed methods are calculated from binary image where absolute intensity values are not directly considered for calculation. Binary levels are used for feature extraction. So, these features can be categorized as 'binary features' or following the already used standard nomenclature pattern can be addressed as 'zero order features'. The coding steps to write a program for feature extraction from a binary image are discussed in appendix B.

Let us observe the effects of rotation of an image on the proposed features. IPF and porousness features are image orientation independent. Rotation of image has no effect in these feature values. Let us rotate the image array shown in figure 2.3(a) by 90 degree. The new image array I' is shown in figure 2.12. L, u, z, y and w from I' are extracted and compared with the respective values of I. The results presented in the figure are demonstrating no change in u, z and w. But a significant change in L and y are observed.

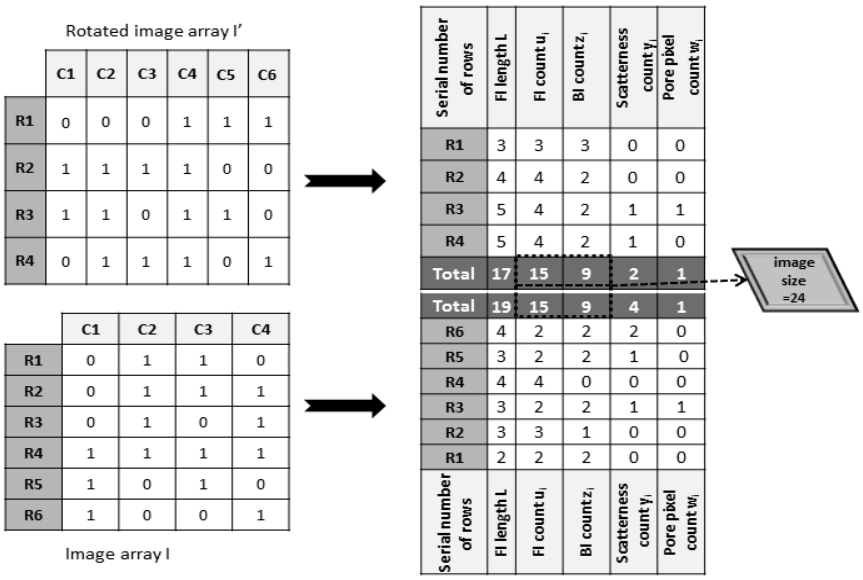

Figure 2.12: Comparison of features after 90° rotation of image

By proposed definition, IPF = u/(u+z) where u+z = image size.

So, we can say, IPF α u. Image size retains same even after rotation. As u is not affected by rotation, IPF remains unchanged after rotation. Porousness P is a function of u and w and both of these values remain unaffected by rotation. Hence, P also remains unaltered after rotation.

Compactness depends on u and y where y changes after rotation of image. So, compactness as well as scatterness is image orientation dependent features. But if the image is just flipped i.e. the total rotation is 180 degree, no features proposed in this chapter will be affected.

Hence, the key facts of proposed features can be listed as

- Images under process must have some usable information.
- Proposed features can be addressed as 0^{th} order features.
- Rotation of image will not affect IPF and porousness values.
- Compactness and scatterness are image orientation dependent features until and unless the rotation angle is multiple of 180 degree.

Features, except IPF, are calculated with respect to the target area, majorly covered by foreground information. Entire image i.e. image including background area, is not taken into account. So, it can be concluded that IPF is a global feature and rest are local features.

2.7. Conclusion

Three major quickly computable image features, IPF, compactness and porousness, are proposed in this work. These features seem to have impressive applicability in different types of image data. Proposed features are extracted from both CT and MR image of brain for result analysis. Initial outcomes are promising. Degree of accuracy can be increased by using these features in combination with higher order texture features at a cost of computational load. Depending on requirement, that can be decided by user. It has been observed that without doing detail pixel by pixel intensity evaluation, fast sorting of CT brain images depending on its foreground volume and information spread is possible. Unusual information gap in an image can be identified quickly by porousness feature. All these results can provide guidance for further in depth analysis of an image or image dataset. These features are promising for identification, initial selection, indexing or classification of images. The enhancement of computer vision lies in

the quick initial selection capacity which is intuitive in human beings. These features will help to grab the 'overview first' to make a basic understanding of an image.

In this chapter, image descriptor is created from gray image. To extract the same features from color images additional investigations are necessary. Mathematical model needs to be modified to convert the color image into its equivalent binary.

In the next chapter, extraction of skull encapsulated part of brain which is the target ROI for hemorrhage segmentation is discussed. These proposed features are used in different steps of segmentation to enhance accuracy of the CAD system described in the following chapters. These features also have significant contribution in hemorrhage classification, discussed in chapter 5.

Chapter 3

Brain Segmentation

Overview

Brain hemorrhages, irrespective of its type, physically remain confined within the skull. This knowledge helps us to narrow down hemorrhage search area and reduces computational load. In this presented research work, intracranial section of a head image is considered as region of interest (ROI) for hemorrhage segmentation. In this chapter an automatic and robust brain segmentation method is proposed to segment the intracranial part from CT scan dataset as a part of the final CAD system for hemorrhage segmentation and classification. Adaptive thresholding, automatic seed point finding, knowledge driven region growing and multilevel masking are key potentials of this method. For mask definition, best suitable brain image of a dataset is selected as master image. Two types of masks are created from this master image. One mask is used to segment brain matter and another one to restrict inclusion of the non-intracranial area of nasal images. This second mask is a global reference mask and is designed for all images in a dataset. Brain matter mask is implemented on adjacent images of master image and is automatically updated for the next image. This mask propagates independently in two different directions keeping master image at center. Segmentation result shows highest sensitivity and reasonably good accuracy in all cases. Performance of proposed method is compared with other popular brain segmentation methods.

3.1. Introduction

As already discussed in previous chapters, any image array contains two significant types of data – background and foreground. For medical analysis the foreground part is important, but background also supports the computation process indirectly. Scan images often contain some unwanted external information which can introduce errors during computation and analysis through a computer. To reduce such noises in final analysis, images are pre-processed during which external parts along with non-contributing parts are removed from an image.

There are some reported works on interactive or adaptive brain segmentation. Prominent works have been discussed in literature review section of chapter 1. In most of the cases, there is always a requirement of radiology expert to initiate the process. Work reported by Chan, 2007 [28], proposed removing non-intracranial part by deleting everything not connected with largest brain part. This method tends to introduce error in nasal images by deleting parts of the brain not connected to largest segment and considering non-intracranial parts which are connected to the brain through paranasal sinuses. Bardera et al. (2009) [31] proposed segmentation by interactive region growing technique. Their proposed Computer Aided Diagnosis (CAD) needs manual feeding of seed point, threshold and tuning to improve segmentation accuracy. Threshold finding from histogram is proposed by Liao et al., 2010 [80]; though the automation algorithm is not proposed. In this proposal, segmentation is done separately on each two dimensional (2D) image following the concept of Chan, 2007 [28]. The negativities of this method are high computational load and lower accuracy in the segmentation of nasal images. It has been observed that region growing technique is mostly used because of its ease and accuracy, but automatic seed point finding is a challenge. To define the boundary of the growing region, thresholds are either given interactively or adapted computationally from the histogram, with some user defined constant cost factor [24,79]. Segmentation of nasal images, is addressed in a very limited number of works and the establishment of the potential of algorithms is missing. Before proposing a method the key challenges in this area are listed:-

(1) Automatic seed point finding for region grow technique

(2) Effective segmentation of nasal images

(3) Handling complete dataset at a time

The method proposed here is designed to address above mentioned challenges to roll out completely automatic, highly accurate brain matter segmentation system. The segmented brain can also be used for clinical assistance to diagnose and treat brain disorders other than hemorrhage. This method is comparatively more robust and faster. It is capable of carrying out batch processing of the multi-slice head CT dataset of a patient. One master image is selected automatically for mask creation. A modified thresholding and region growing technique is proposed to create the mask. Instead of creating separate mask for each and every image, mask propagation is used that reduces the computational load. Any information outside the skull and the skull itself is removed completely to get final segmented image. Proposed modified region growing technique is completely automatic. There is no need of seed point or Region of Interest (ROI) selection by the end-user.

In the succeeding part of this chapter, details methodology is described, followed by results and its analysis. The proposed method is applied on several datasets and the results are presented with graph and images. Analysis of achievement is calculated and potential of the work is discussed at the end.

3.2. Database and CAD outline

Multiple slice head CT scan of different subjects are taken for segmentation of brain matter. A model is designed for complete automation. Extracted brain images are named after their original name and saved automatically in a new folder in the same location of the source folder.

The CAD system's sequential operational steps are described in the flowchart given in figure 3.1. An entire dataset of multiple 2D images is read and processed for pre-processing steps like thresholding, master image selection, arranging images in anatomical sequence and computation of masks definition. Masking is done in two stages, having an in-between step where the complete dataset is split into two parts with respect to master image which is selected automatically by CAD.

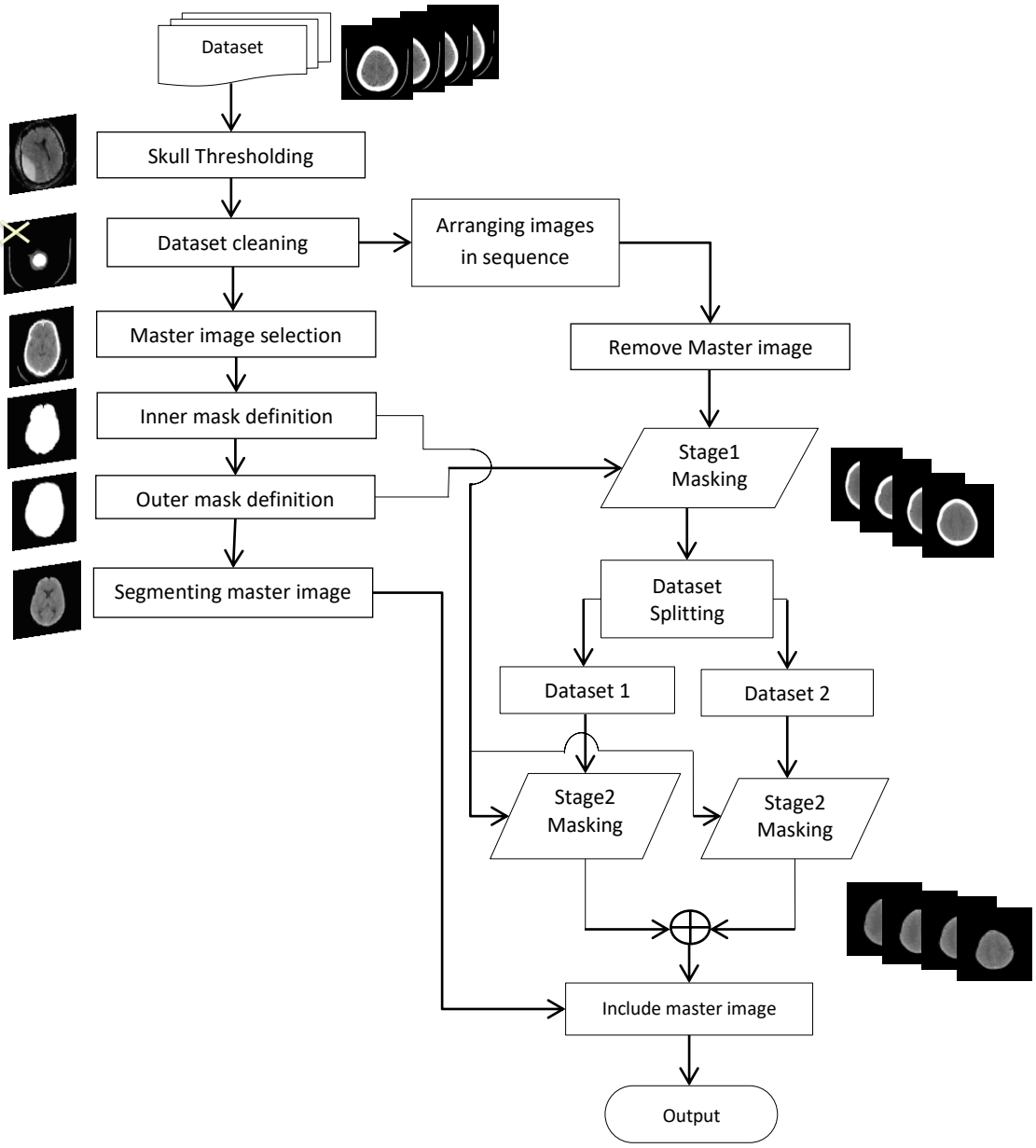

Figure 3.1 : Process flowchart for segmentation of brain from head CT scan dataset

3.3. Methodology

For each dataset, one image, which has been referred as the master image in this chapter is selected from that dataset only. This master image is used as a reference to define the mask for that dataset. Use of single global reference image for all datasets is avoided to make the system tolerant to artifacts like ring artifacts, noise, motion artifacts, varying brain shape etc. It will also help to neutralize the error due to patient's alignment [136]. Rather than a manual selection of reference image [79], an automatic selection method is designed. For automation, intensity distribution in a head CT scan is thoroughly studied.

3.3.1. CT image intensity distribution

CT images are acquired using x-ray exposure. Absorption amount of x-ray is different for different tissues. The complete range i.e. from no absorption to complete absorption is presented using Hounsfield Unit (HU) scale where air is presented by -1000 HU, water as 0 HU and bone has the highest value from several hundred to +3000 HU.

This HU scale is designed using linear transformation of actual attenuation coefficient. The transformation computation is performed by following equation,

$$\mathrm{HU} = \frac{\mu_x - \mu_{h_2o}}{\mu_{h_2o} - \mu_{air}} \times 1000$$

where μ_x presents attenuation coefficient of matter called X, μ_{air} and μ_{h_2o} are attenuation coefficient of air and water. Matter with attenuation coefficient less than water will return negative Hounsfield unit.

HU is mapped to the intensity range [0,255] to display gray scale image digitally. Depending on practitioners' requirement a range of HU is emphasized and rest is suppressed to the nearest boundary value. This method is called windowing, where a window is defined using two parameters window width (ww) and window level (wl). Window width is the complete length of HU which is considered to be mapped into gray level. Window level is the mid-HU value of that width.

All types of hemorrhage introduce bright homogeneous spots in the head CT image. Depending on the amount of collected blood, the brightness slightly varies. Denser layers offer brighter spot in image. On the other hand, the brightness of hemorrhage is always significantly lower than that of bone or skull, but higher than brain matter. To detect hemorrhage, brain window scanning mode is used. In this mode, default wl value is 40 HU [137]. Value of ww is different (100 or 400) for different datasets in use.

Figure 3.2(a) presents the gradual change in brain image pixels' intensity i.e. HU values [138, 139] with the change in density of different parts of brain. The example of a head CT image is shown in figure 3.2(b). The skull and headrest are presented by the brightest part of the image. As observed, hemorrhage patches are significantly brighter than the surrounding, but have satisfactorily lower intensity

than skull. The transition from one part to another part offers gradual change in pixel intensity making the boarder less significant.

Density property	Brain matters	HU values
Hypodense	Air	-1000
	Fat	-84
	Water	0
	CSF	4-16
	White matter	30
	Gray matter	38
	Hemorrhage	40 - 90
Hyperdense	Bone	>1000

(a)

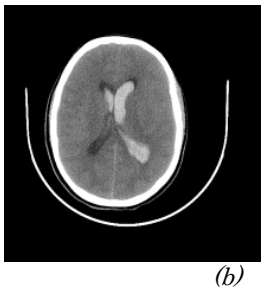

(b)

Figure 3.2: (a) Intensity varies with density in CT image (b) CT image

3.3.2. Pre-processing of data

Before segmentation, pre-processing of CT images is important to increase sensitivity and accuracy of a CAD system. As discussed in previous chapter, any inclusion of unwanted terminal images having only skull or scalp needs to be removed. For any CT image, the background and skull which offers no clinical information are respectively the darkest and brightest part of the image. The intensity value remains mostly zero for background. Skull as a whole, different external parts like headrest and disorder like calcification offer very high intensity region in the image. These areas contain no information about hemorrhage. Any presence of soft tissue oedema outside the skull gets imaged during scan. These parts introduce noise in segmentation and thresholding process due to its matching intensity level with brain matters and sometimes with hemorrhage. Removal of all these non-relevant parts from image is required before processing the data for hemorrhage segmentation.

As already discussed, each digital image is basically a 2D numeric array which can readily be used for mathematical computation. Removal of high volume background and high intensity skull reduces load in further data computation. For each image, designed CAD dynamically selects threshold for skull from its intensity population curve. Histogram shown in figure 3.3(a) has a large peak at lower intensity level which represents the large number of low intensity information i.e. background and another large peak near maximum available intensity representing the skull. None of these two areas contains any disease

relevant information. The 3rd highest peak in histogram represents the population of brain matter.

3.3.2.1. Skull thresholding

Each image is read separately as an independent image. To remove the skull from it, threshold intensity value is calculated from image histogram. In clinical CT, skull lays in very high-intensity level where no disease other than calcification is present and the maximum available intensity is guaranteed to belong to the skull. In the histogram, shown in figure 3.3 (b), the highest peak belongs to the skull and the second highest peak represents the brain when the background population of figure 3.2(b) is neglected. An easy but effective method is proposed to locate the cut-off intensity automatically between these two peaks.

The method is a knowledge driven thresholding method. Observation of histograms of large number of head CT scan data yields two important facts,

i) *The population of intensity becomes almost even before high volume skull intensity and*
ii) *In any 8-bit gray CT image, major skull information is confined within the highest 1/3rd intensity span of available intensity range of the image.*

Using these two known information, a thresholding algorithm is developed. Maximum and minimum available intensity in a dataset is considered to find the target span. This span is used as a global reference for all images in the respective dataset.

In the population curve, absolute slope of each intensity level with respect to the next level is calculated. The most even part nearest to the high volume skull is considered as the boundary between brain and skull. Intensity value that offers minimum value of function f(x), described in equation 3.1, denotes the threshold for skull. f(x) is a function of slope weighted by a distance cost factor, d, where the distance is the difference between the highest available intensity and intensity of corresponding slope.

$$f(x) = \frac{\partial P}{\partial i} * d \tag{3.1}$$

∂P and ∂i presents deviation in population and intensity respectively at the point of measurement;

at i^{th} instant, $\partial p = |p_{i-1} - p_i|$ and $\partial i = |I_{i-1} - I_i|$

The resulted threshold value along with span is plotted on the graph shown in figure 3.3(c). Threshold point is calculated for each image of a dataset separately. Image without skull and the removed skull image of original image shown in figure 3.2(b) are shown in figure 3.3(d)-(e). The flowchart of automatic threshold selection process is presented in figure 3.4.

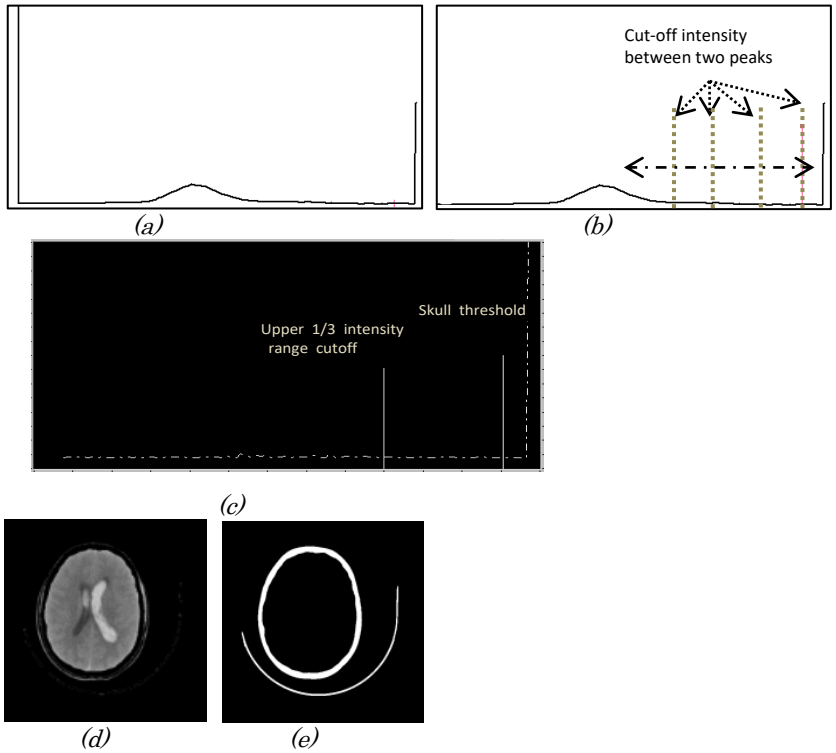

Figure 3.3: (a) Intensity histogram, (b) Background neglected histogram, (c) Histogram with upper 1/3rd span and skull threshold, (d) Skull removed image, (e) Removed skull part (binary image)

3.3.2.1. Dataset cleaning

After removing skull from the image dataset, a cleaning operation is performed to optimise the dataset. Skull image of each image data is generated as a by-product in the previous step of thresholding. Brain is an encapsulated portion within the skull. It can't be present without a skull; neither can be present in an image where skull offers no vacancy within it. Those images need no inspection for hemorrhage and hence are removed from the dataset. In the skull images, images with no skull information are identified and removed first. Image data without skull is shown in figure 3.5 (a).

The pores are then counted in the skull images. If any image returns no pore, that image is also removed from dataset. Head images without any pore are shown in figure 3.5 (b) to (d).

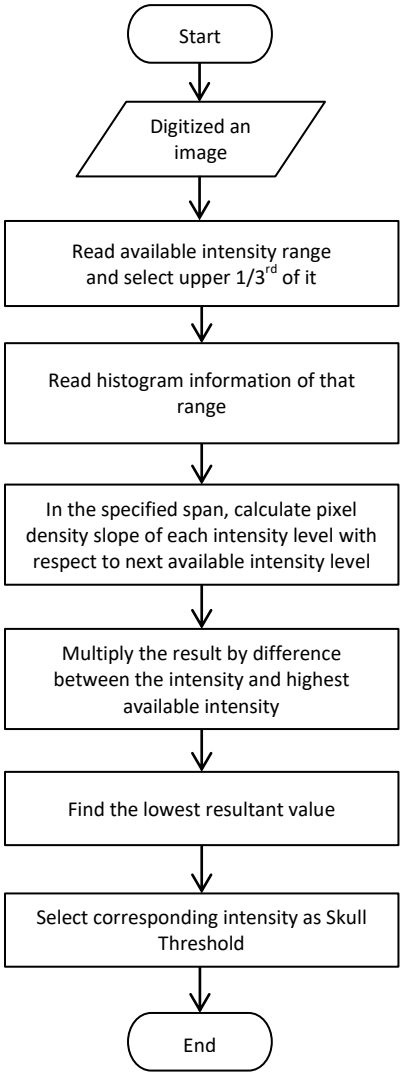

Figure 3.4: Skull threshold finding flowchart

3.3.3. Master image selection

Skull images have great potential in master image identification. These images mainly contain the skull part surrounding the brain matter along with some low volume higher intensity information located outside the brain. To create a mask for segmentation, the objective is selecting the image with maximum brain area as the master image. Anatomically brain matter is the highly compact largest connected part in a head image. In a multi-slice dataset, produced by end to end head scan, nasal information gets included in some images where brain area is low and divided into lobes. To select master image the image having largest compact brain area in the dataset needs to be identified.

Skull images created from an end to end head scan are considered to study the brain matter availability pattern in CT images. At ventricle level, CT images

offer largest continuous brain area for inspection. Skull pattern changes significantly, from base of skull i.e. nasal area to ventricle level. Around nasal area, bony structures other than the skull are also imaged during scan. Those bones create several porous regions in the image dividing the brain into more than one part as shown in figure 3.6. The total brain area is also low here. On the contrary, a single large brain area is available inside the elliptical skull near brain ventricular region. A query runs to find largest pore area from each image. The image having highest value of largest pore area is selected as master image of the dataset under test.

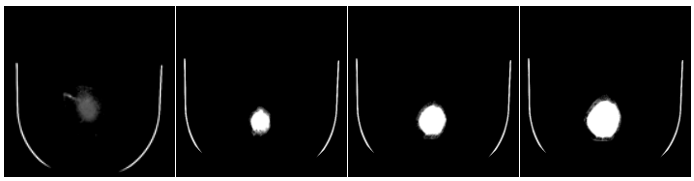

(a) *(b)* *(c)* *(d)*

Figure 3.5: Head images with no brain information

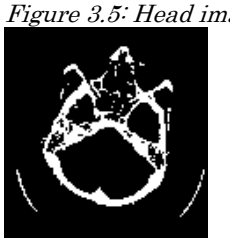

Figure 3.6: Skull after thresholding a nasal image

3.3.4. Arranging images

The sequence of images in the dataset under test is unknown. For an end to end sequential scan, information pattern in images, changes gradually from low to high and back to low. Prior knowledge of this pattern is very helpful for high accuracy segmentation. But, as already discussed in introduction section of chapter 2, many datasets includes one or more images which are rescanned after the end to end sequential scan to satisfy diagnosis requirement [63]. Sometimes one region of head is scanned first and then adjacent areas are scanned for more investigation. So the saved images may or may not be present in order of their changing information pattern. On the other hand, the method proposed in this thesis, offers the best result when the images in a dataset are in the expected scan sequence. To overcome this problem of unexpected scan sequence, all the images are rearranged automatically in the anatomical order using stereo matching. Stereo matching is popularly used to identify moving objects within an image

frame [140]. A sequentially arranged head CT dataset can be conceptualized as a collection of footprints of an image, some components of which have travelled a distance gradually. Hence, each image can be considered as a frame of the video formed by the entire dataset. Lowest disparity presents minimum transition i.e. nearest image. The test is performed on skull removed dataset and the image with lowest IPF from the dataset is selected as seed image. The image from the dataset having highest stereo match with seed image is then selected as the next image. Now the newly selected image is considered as seed image for the next search. This checking procedure runs for each image until all the images are arranged. The program flow is demonstrated in figure 3.7. Out of order dataset is processed using this method and the result is discussed with image in result section.

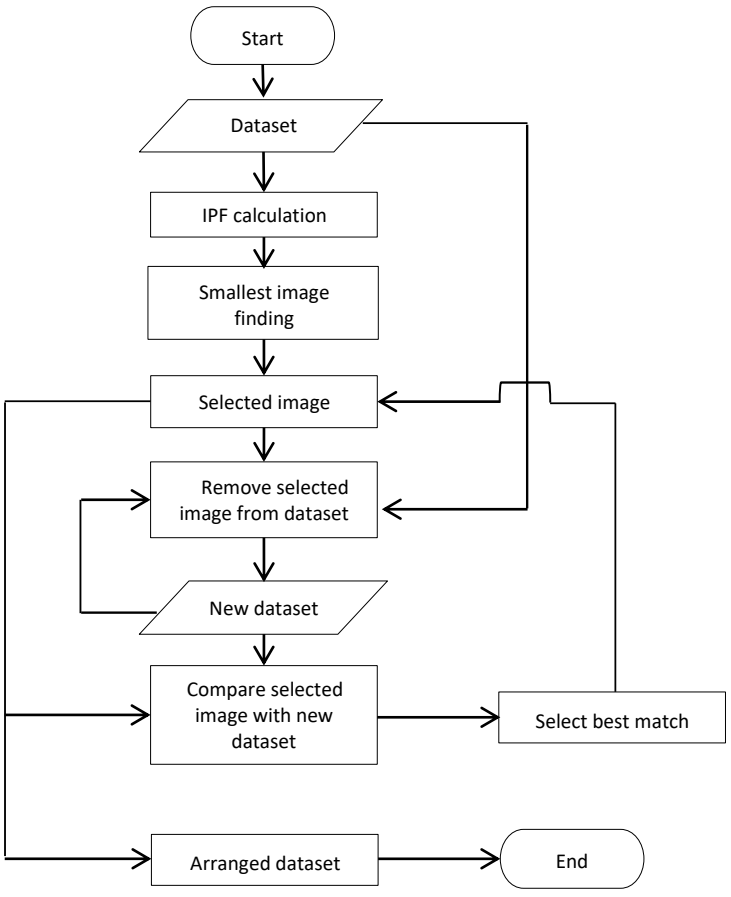

Figure 3.7: Arranging images in expected sequence

3.3.5. Automatic Seed point definition

The selected master image is taken as the reference to create the mask for brain segmentation. As it has the largest area encapsulated by skull, significantly

large portion of the non-zero pixels' area is occupied by brain matter in original image. For simplification of operation, a binary equivalent of master image is created from skull image. Two distinct levels of the resultant binary image are – below skull threshold and equal to or above the skull threshold. All pixels having intensity below the threshold were already suppressed to 0 during skull extraction. These pixels create level 0 of the binary image. Rest of the pixels are promoted to 255 to create level 1. Figure 3.8 is showing that brain is completely encircled by the white thick boundary represented by the skull of the original image. Region growing technique with a seed point anywhere within the skull boundary can accurately identify the area required to create the mask for brain segmentation.

To make the proposed system completely automatic, instead of interactive seed point selection, a computational seed point finding method is used. An algorithm is developed to locate the center of non-zero pixel distribution of the master image by identifying distribution midlines across rows (i) and columns (j). The crossing point of two midlines is considered as seed point when it has non-zero intensity level in original image. Otherwise, the closest non-zero pixel location is considered as the seed point.

Coordinates of Seed point S(i,j) are

$$[i,j] = \left[\frac{imin + imax}{2}, \frac{jmin + jmax}{2}\right], when\ S(i,j) > 0$$

$$= \min\left\{\left[\frac{imin + imax}{2} + \alpha, \frac{jmin + jmax}{2} + \beta\right]\right\}, otherwise$$

when α and ß can be any integer values starting from 0.

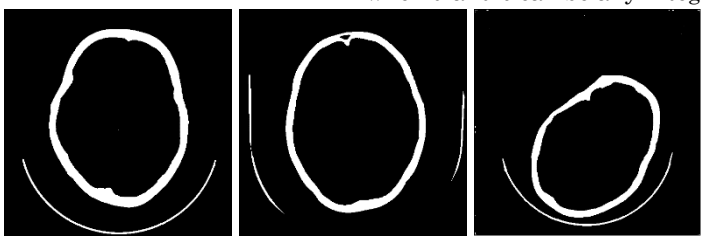

Figure 3.8: Binary images of different reference images

3.3.6. Mask Area Definition

Region growing technique is applied on binary equivalent image to define the mask. High pixel intensity i.e. 255 is taken as stop criterion. To define the mask, the complete image must be divided into two regions – brain and the rest. Two different algorithms are attempted to grow the region around seed point. In

one algorithm, all similar intensity neighbors of seed point are located and selected. Then for each selected point the search repeats. The algorithm offers 100% accuracy in segmentation at a cost of long execution time.

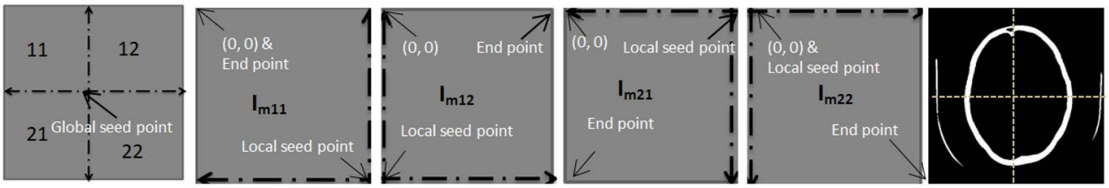

Figure 3.9: Splitting an image into 4 sub-images and seed point of each sub-image for region growing technique

In the second algorithm, a complete image is divided into four sub-images keeping seed point as the origin of splitting axes, as shown in figure 3.9. Region growing is done in each sub-image separately and the resultant images are merged back into one image. When the image is divided into four, each one is treated as an independent image by the software. To implement region growing technique, local seed points are required for each sub-images. A non-zero pixel which is nearest to the global seed point is selected through the algorithm to act as a local seed point. The seed point location details is given in appendix C. Search query starts from local seed point, moves towards the extreme end and terminates upon meeting stop criterion. In this algorithm, the query runs in only one direction at a time. It selects all *same intensity level pixels,* until stop criteria satisfied. After region growing, sub-images are merged and converted into the mask. This 'split and grow' algorithm works much faster than the above-discussed neighbor search algorithm. Created mask is considered as the inner mask (IM) because it defines the area inside the skull.

Though inner mask defines largest brain matter in the dataset, if it is used as the global mask for segmentation of entire dataset, in many images, unwanted information will be segmented as brain matter, as shown in figure 3.10 (a) and (b). Images having complex pattern due to the inclusion of nasal area, sinuses, eye, optical canal etc. offer poor segmentation result by including out of the skull low intensity areas. Figure 3.10(b) is a terminal CT image taken from top of the head. It has very low brain area with respect to inner mask. Direct application of inner mask thus included unwanted non-intracranial information in segmented image. From nasal level to ventricle level, brain shape and size changes fast in a non-uniform pattern. As discussed in previous section, brain in a CT scan image of

nasal area gets divided into lobes and then gradually becomes very small. From ventricle level to top of the head, not the brain shape but the size changes significantly. So, it has been observed that inner mask works accurately only on images having brain of almost same size and shape of the mask as shown in figure 3.10 (c) and (d).To get rid of this shape and size problem, the segmentation algorithm is enhanced and modified.

The arranged dataset is now divided into two parts keeping master image at the center. Two adjacent images of master image, one from preceding part and another from following part, are segmented using the inner mask definition. After segmentation, a search runs to find and include the additional connected area of the similar intensity level. The final segmented area of one image is considered as inner mask definition for next adjacent image of that segmented image. This mask propagation technique offers significant improvement in segmentation result.

Independent use of inner mask with propagation technique increases inaccuracy in the nasal images by including all connected non-intracranial sinus areas as shown in figure 3.10 (e).

To put some restrictions over such inclusion another mask is proposed. In this mask definition, the skull area of the master image is included. Skull around inner mask is considered to get larger mask which is referred as the outer mask (UM) in this thesis. Mathematically it is presented below,

Outer mask= inner mask + skull

This mask is defined used as global mask for all images of corresponding dataset. Final masking is proposed using two steps. Outer mask is applied on each skull removed image of the dataset to remove any information located outside the skull location of the master image. It reduces the area of the non-intracranial part of complex nasal images as shown in figure 3.10 (f). Resultant images are used for further segmentation by inner mask propagation.

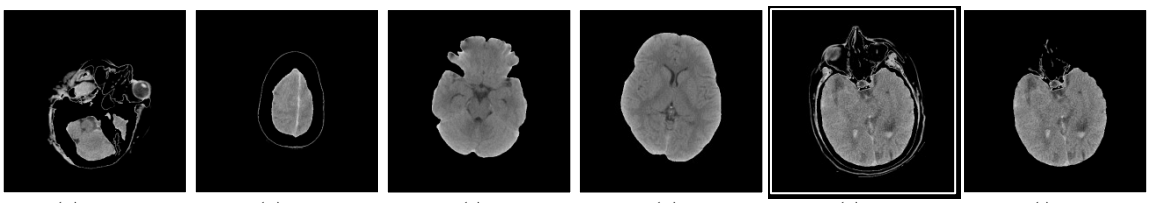

(a) *(b)* *(c)* *(d)* *(e)* *(f)*

Figure 3.10: Brain segmented by inner masking only

3.4. Result

Proposed algorithms are coded using LabVIEW (Laboratory Virtual Instrumentation Engineering Workbench) programming platform and tested on entire database of head CT scan. In this complete collection, 16 datasets are of normal subjects, 27 are having hemorrhage and one dataset has very low scan area. The results of proposed segmentation method are discussed here step by step following the sequence of the program as shown in the flowchart in figure 3.1. Results of complete analysis of all dataset and two dataset without cleaning are collated for presentation.

3.4.1 Skull thresholding and dataset cleaning

The threshold value is calculated separately for each image of a dataset by CAD to remove skull. Some thresholded images of different dataset are shown in figure 3.11. The result depicts that brain mostly remains unaffected by this thresholding. Only calcification is removed in figure 3.11 (b) and in some hemorrhage affected images, small sprinkled holes are introduced in hemorrhage part as shown in figure 3.11(c) and (d).

Following the skull thresholding, dataset is cleaned by removing images without skull and skull without pore. Images with no brain information are removed at this stage and cleaned dataset is processed for further analysis. Removed images of a dataset which is shown in figure 3.12 (a) are shown in figure 3.12 (b).

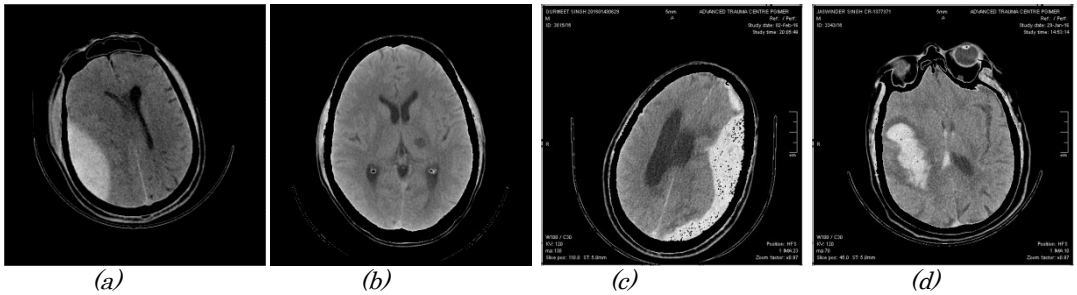

(a) (b) (c) (d)

Figure 3.11: CT scan after skull thresholding

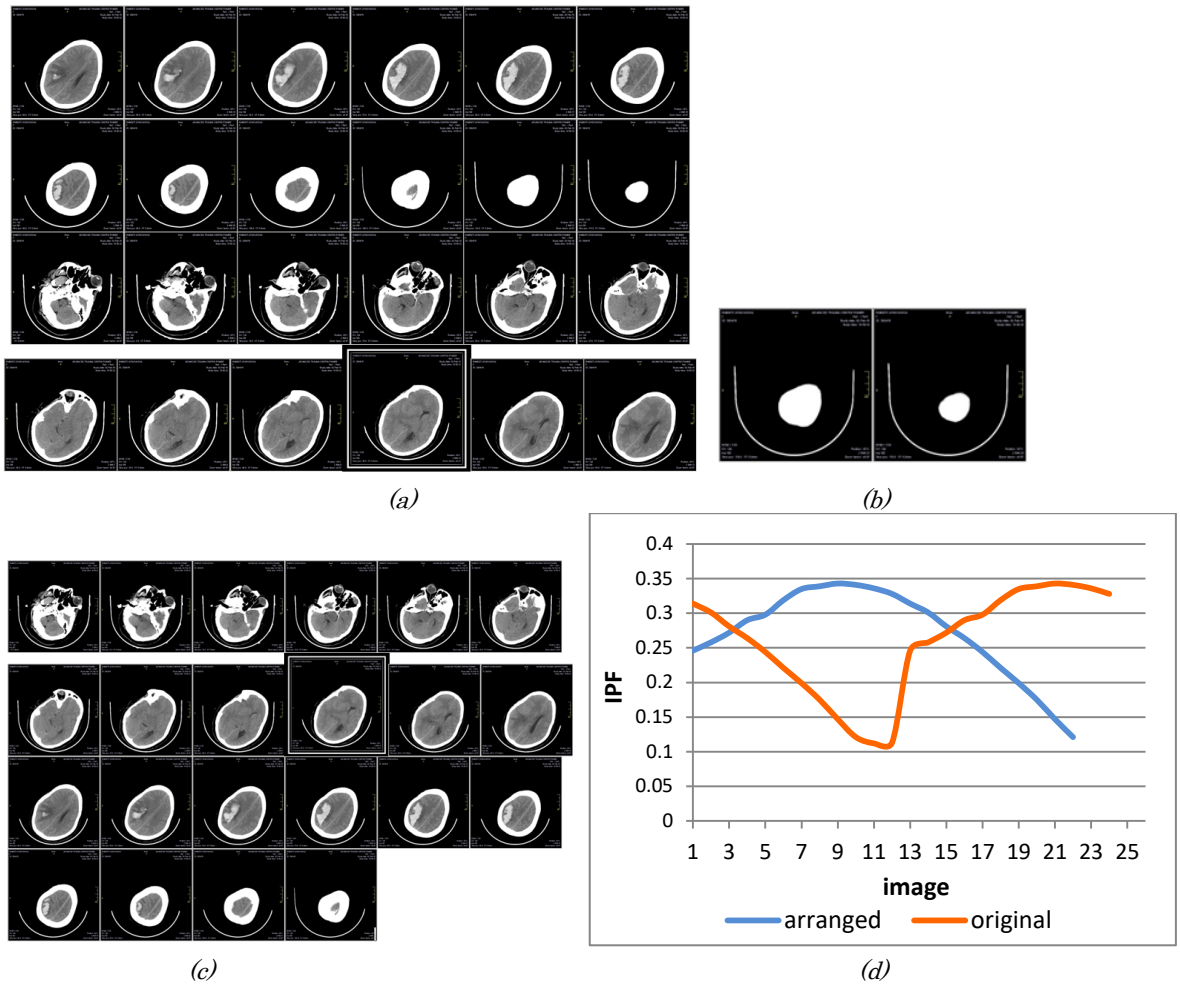

Figure 3.12: (a) Image dataset with master image, (b) Removed images during cleaning (c) Dataset after arranging the images with master image, (d) The graph of change in size before and after arranging the images

3.4.2 Master image selection

From the skull removed images, master image is selected by computing the highest rank of largest available pore area in the images of the dataset. Proposed CAD has successfully selected master image irrespective of its location and sequence in the dataset. One result is presented in figure 3.12 (a). Selected master image is highlighted by a boarder in the figure.

Though normally head CT scanning is done in sequence from one end to another end of the head, this dataset has images in abnormal sequence. The selection of middle image as the master image [141] is not wise here as the middle image i.e. 12^{th} image has no brain information. Proposed method offers an effective solution to this problem and also removes such unwanted images from dataset.

3.4.3 Arranging images

Images, shown in figure 3.12(a), are not in the expected order. The first image, as well as the last one, is presenting ventricle level images of a head scan dataset. The change in brain is gradual negative in 1st thirteen images and then gradual positive for the rest. But the change between 12th and 13th image has no similarity. The master image selected by CAD is the 3rd last in the series. If masking is done in this sequence, no brain will be extracted from first 11 images as the 12th image has no brain. Successive propagation will turn the inner mask area to zero at 12th image.

After arranging images, using proposed algorithm, images are placed in expected order as shown in figure 3.12(c). The change in size of images before and after arranging is compared in the graph shown in figure 3.12(d). The master image is also at expected location in the arranged dataset.

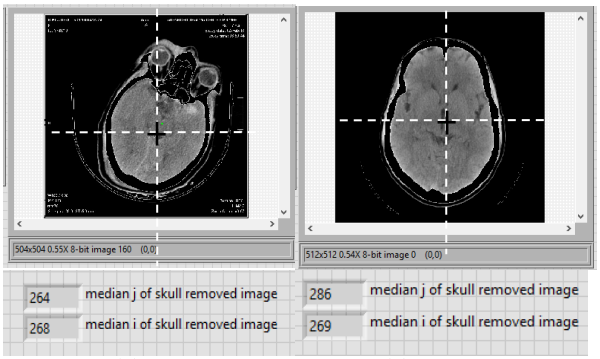

(a) (b)

Figure 3.13: Seed point location marked by '+'

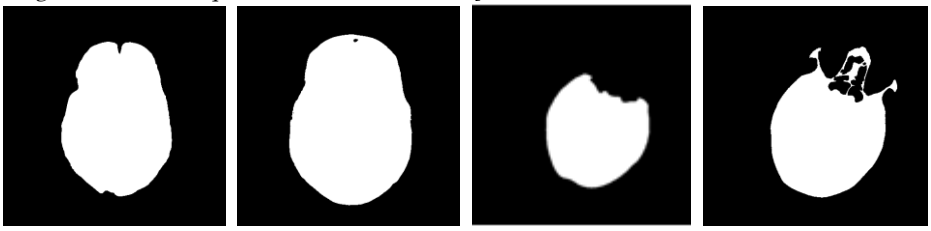

(a) (b) (c) (d)

Figure 3.14: (a)-(b) Inner mask and outer mask of figure 13(a), (c)-(d) Inner mask and outer mask of figure 13(b) respectively

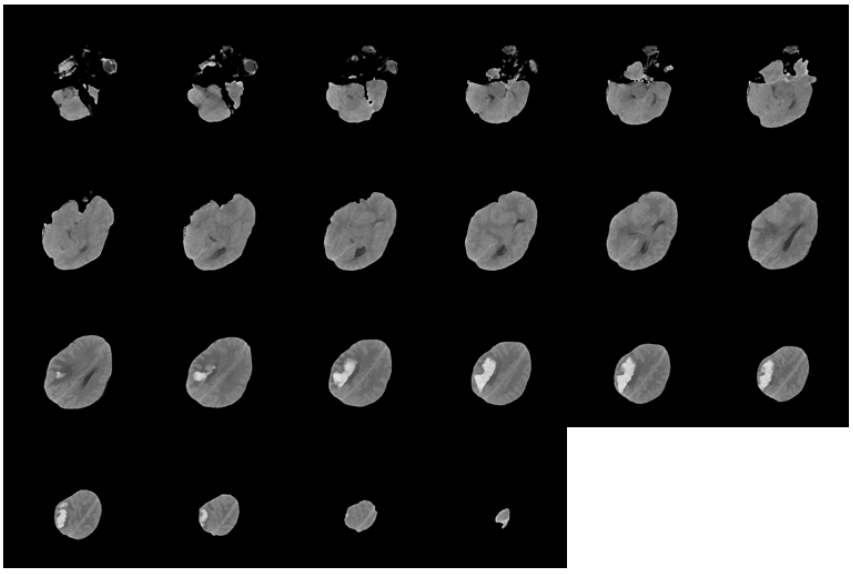

Figure 3.15: Segmented brain for figure 12(a) dataset

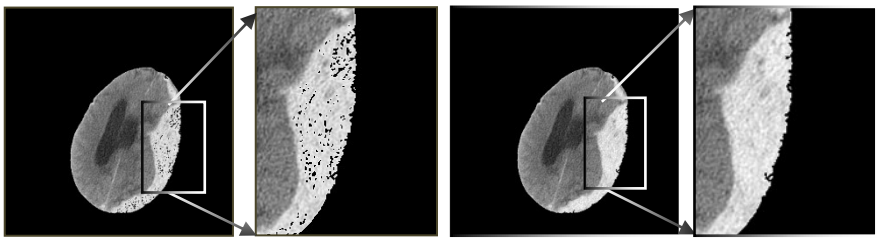

Figure 3.16: (a) Holes created during skull removal, (b) Restoration result

3.4.4 Seed point & Mask

Center of splitting axes i.e. the seed point is the median of row and column of the master image. In figure 3.13, seed points are marked as 'black cross marks' on reference images of two different datasets. In every case, it is successfully placed within the intracranial location. The success rate is 100% for all datasets under examination.

The binary image is formed from the reference image by converting any value below the threshold to zero and rest of the values to 255. Then the binary image is split into four sub-images by the perpendicular axes originated from seed point (Δn, Δm). First, the image is divided into two parts by x-axis at $x=\Delta n$ i.e. one part contains 0 to Δn rows, another from $(\Delta n+1)$ to n and then each part divided again by y-axis at Δm, splitting each from 0 to Δm and $(\Delta m+1)$ to m when the complete image size is nXm. Region growing technique by pixel matching works accurately to define intracranial area (IM) and skull included intracranial area (UM). Created inner mask and outer mask from master images which are shown in figure 3.13 (a)-(b) are presented respectively in figure 3.14 (a)-(d).

3.4.5 Segmentation

Figure 3.15 presents segmented brains, after two level masking and doing adjacent area search, of the dataset shown in figure 3.12(a). Complete segmented dataset presents the method's performance quality. All those images which have majorly brain parts, offer very clean segmentation. Images beyond any null brain image are also segmented accurately. Some nasal images are offering larger area than actual brain area as lower intensity areas around the skull and facial bones get included. The inclusion of such unwanted parts happens during an adjacent area search. These areas get included due to their connectivity with brain through paranasal sinus.

After segmentation, information restoration within brain can be done as shown in figure 3.16. The holes created within hemorrhage during segmentation process can be filled with original information automatically by CAD. Location information of the holes are extracted using the algorithm described in section C of Appendix B. A mask is created to retrieve the intensity information from the respective locations of the original image. Collected information is added to the segmented image. The drawback of restoration is the chance of inclusion of calcification, if any. So, for hemorrhage segmentation we have avoided this restoration process.

3.5. Result analysis

Each image in a dataset is segmented to remove most of the unwanted information from it. Performance analysis of the proposed method is done in terms of accuracy, sensitivity, specificity, error, PPV (positive predictive value), NPV (negative predictive value) using the values of true positive (TP), false positive (FP), false negative (FN), true negative (TN). TP and TN present correct segmentation (CS) as per clinical ground truth. When an image with brain information returns brain in segmentation and an image without brain returns null segmentation the segmentation results are considered as true positive and true negative respectively. TN in a dataset is the count of images which contains no intracranial information. Such images are effectively removed during cleaning operation. The inclusion of external tissue parts in the nasal area contributes in FP. Non-zero segmented values for original images having no intracranial

information is also addressed as FP. In first case, segmented images having nasal tissue area also contribute to TP count because of having segmented brain into it. Such images thus get membership of two classes, FP and TP and create confusion in result analysis. Hence, another term absolute FP (AbsFP) is introduced to identify segmented images having non-brain non-zero values only. No actual brain will be available in such images. The segmented images containing actual brain information will be classified as TP even when non-brain peripheral information is included. The conceptual presentation of TP, AbsFP, TN and FN is shown pictorially in table 3.1. The overall segmentation performance is calculated with respect to the volume of a dataset i.e. the total number of images.

	Image with brain	Image without brain
Segmentation have brain	TP	AbsFP
Segmentation without brain	FN	TN

Table 3.1: Pictorial presentation of TP, AbsFP, FN, TN

For a dataset of n number of images the analysis parameters of confusion matrix are extracted using the equations stated in chapter 1. The term FP is replaced by AbsFP as follows:

$$n = AbsFP + FN + CS$$

$$\%error = \frac{AbsFP + FN}{n} * 100\%$$

$$specificity = \frac{TN}{TN + AbsFP}$$

$$positive\ predictive\ value = \frac{TP}{TP + AbsFP}$$

The proposed method has offered an average accuracy of 98.17%. No false negative (FN) in segmentation turns the sensitivity into 1 for this method. For the dataset having no image without brain, TN turns into zero. The specificity and NPV are not calculated for such dataset. The analysis results of 27 hemorrhage dataset and one additional abnormally scanned dataset are presented in table 3.2 (a) and the same of 16 normal image dataset are presented in table 3.2 (b).

dataset serial no.	TP	FN	AbsFP	TN	N	CS	sensitivity	specificity	PPV	NPV	% error	% accuracy
	(number of images)											
1	22	0	0	2	24	24	1	1	1	1	0	100
2	28	0	1	5	34	33	1	0.833	0.966	1	2.941	97.059
3	28	0	0	0	28	28	1	--	1	--	0	100
4	21	0	1	6	28	27	1	0.857	0.955	1	3.571	96.429
5	32	0	0	0	32	32	1	--	1	--	0	100
6	25	0	0	0	25	25	1	--	1	--	0	100
7	23	0	0	3	26	26	1	1	1	1	0	100
8	21	0	1	4	26	25	1	0.8	0.955	1	3.846	96.154
9	19	0	1	6	26	25	1	0.857	0.95	1	3.846	96.154
10	24	0	0	2	26	26	1	1	1	1	0	100
11	23	0	1	2	26	25	1	0.667	0.958	1	3.846	96.154
12	21	0	1	3	25	24	1	0.75	0.955	1	4	96
13	25	0	0	0	25	25	1	--	1	--	0	100
14	24	0	1	1	26	25	1	0.5	0.96	1	3.846	96.154
15	24	0	1	1	26	25	1	0.5	0.96	1	3.846	96.154
16	23	0	1	2	26	25	1	0.667	0.958	1	3.846	96.154
17	19	0	1	3	23	22	1	0.75	0.95	1	4.348	95.652
18	24	0	0	0	24	24	1	--	1	--	0	100
19	23	0	0	3	26	26	1	1	1	1	0	100
20	26	0	0	0	26	26	1	--	1	--	0	100
21	26	0	0	0	26	26	1	--	1	--	0	100
22	26	0	0	0	26	26	1	--	1	--	0	100
23	23	0	0	0	23	23	1	--	1	--	0	100
24	26	0	0	0	26	26	1	--	1	--	0	100
25	26	0	0	0	26	26	1	--	1	--	0	100
26	26	0	0	0	26	26	1	--	1	--	0	100
27-a	2	0	3	7	12	9	1	0.7	0.4	1	25	***75***
27-b	2	0	0	10	12	12	1	1	1	1	0	100
28-a	24	0	2	0	26	24	1	--	0.923	--	7.692	92.308
28-b	24	0	0	2	26	26	1	1	1	1	0	100

Table 3.2 (a): Analysis of segmentation performance of proposed method on patients' dataset

The effect of cleaning is analysed by repeating segmentation of two dataset without performing cleaning operation. Serial no. 27-a is showing very poor performance due to presence of abnormal scan images in the dataset shown in figure 3.17(a). In 27-b, the segmentation of same dataset is presented with cleaning. The performance changes drastically.

dataset serial no.	TP	FN	AbsFP	TN	N	CS	sensitivity	specificity	PPV	NPV	% error	% accuracy
	(number of images)											
1	23	0	1	1	25	24	1	0.5	0.958	1	4	96
2	22	0	2	2	26	24	1	0.5	0.917	1	7.692	92.308
3	20	0	1	5	26	25	1	0.833	0.952	1	3.846	96.154
4	22	0	0	4	26	26	1	1	1	1	0	100
5	22	0	2	2	26	24	1	0.500	0.917	1	7.692	92.308
6	22	0	2	2	26	24	1	0.500	0.917	1	7.692	92.308
7	20	0	1	5	26	25	1	0.833	0.952	1	3.846	96.154
8	22	0	0	4	26	26	1	1	1	1	0	100
9	24	0	0	0	24	24	1	--	1	--	0	100
10	26	0	0	0	26	26	1	--	1	--	0	100
11	26	0	0	0	26	26	1	--	1	--	0	100
12	21	0	1	4	26	25	1	0.800	0.955	1	3.846	96.154
13	23	0	2	1	26	24	1	0.333	0.920	1	7.692	92.308
14	26	0	0	0	26	26	1	--	1	--	0	100
15	26	0	0	0	26	26	1	--	1	--	0	100
16	26	0	0	0	26	26	1	--	1	--	0	100

Table 3.2 (b): Analysis of segmentation performance of proposed method on normal dataset

Serial no.	Work of	Automation	Masking technique	Sensitivity
1	Hu, Q [79]	Full	Inner mask propagation	<1 [2.03% FN]
2	Chan, T [28]	Full	Largest area selection	Not Reported [test performed on our database; sensitivity <1; average sensitivity is approx. 0.94]
3	Shahangian, B [24]	Full		
4	Reported work	Full	Outer mask + inner mask propagation	1

Table 3.3: Comparison of segmentation sensitivity

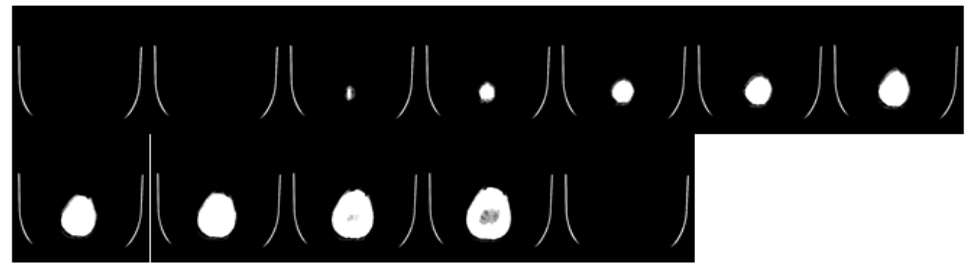

(a)

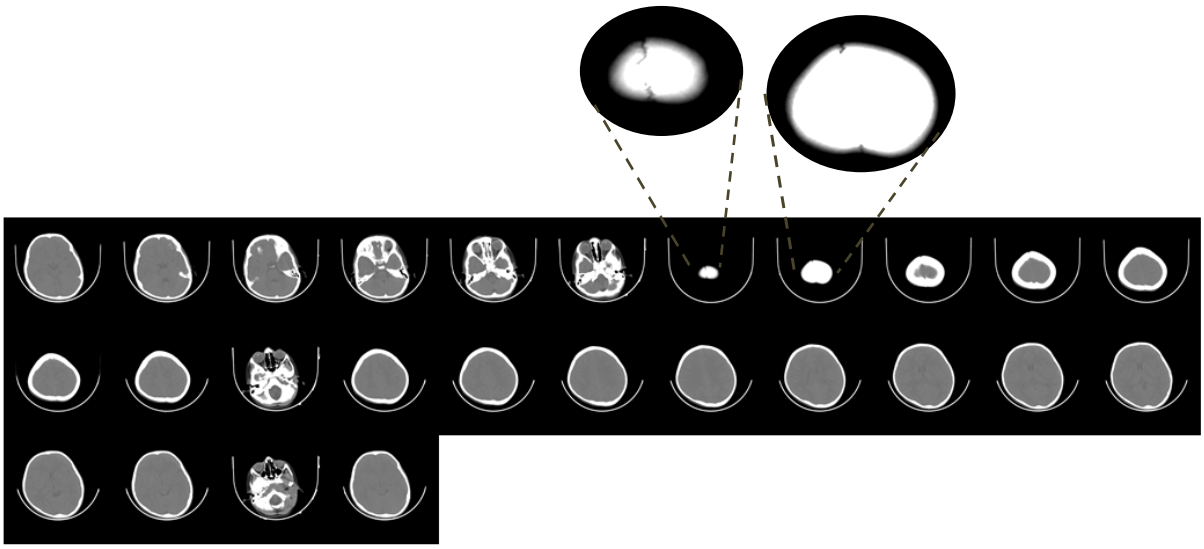

(b)

Figure 3.17: Dataset used to test potential of cleaning operation

Original image	Skulll removed	Methods			Ground truth
		Inner mask propagation	Largest area mask method	Proposed method	
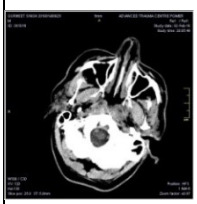	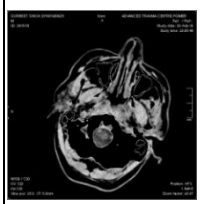	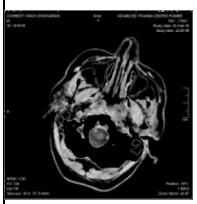	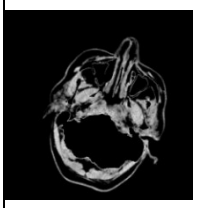	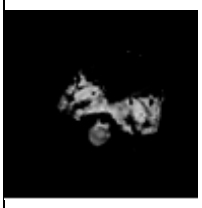	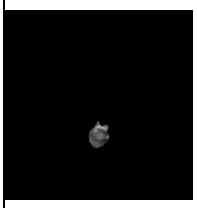
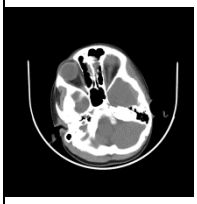	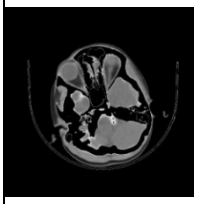	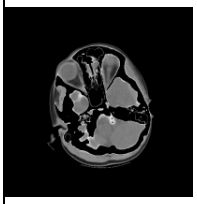	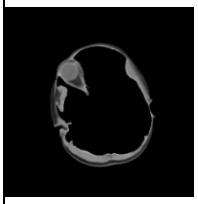	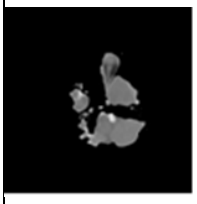	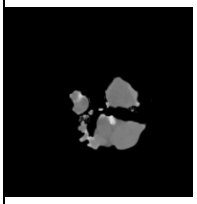

Figure 3.18: Segmented brain images from different method

Dataset 28, presented in figure 3.17(b), is showing comparatively lower accuracy due to higher AbsFP value contributed by soft tissues in no-intracranial

images. The result analysis is presented in 28-a of table 3.2 (a). When those images get removed from dataset by cleaning operation, the proposed method turns the accuracy into 100% as shown in 28-b in the table.

Segmentation results are investigated by practitioners for feedback. It has been confirmed that the segmentation results of proposed method are clinically acceptable because of its higher sensitivity. The sensitivity of this work is also compared with some previously reported potential works to understand its strength. The comparison is shown in table 3.3. For sl. no. 2 and 3, the sensitivity drops due to wrong area selection mainly in nasal area scan images as shown in figure 3.18.

3.6. Conclusion

The proposed method is fast, reliable and robust. It can segment any given dataset of CT images automatically with no false negative. In contrast to manual selection [31], an automatic seed point selection method is proposed. Fast and simple region growing technique is used for segmentation to keep the CAD fast. Largest pore area search methodology offers the creation of a most suitable mask in any dataset. Arranging the images in the expected order significantly increases the accuracy of CAD. Proposed continuous propagation and modification method of an inner mask, results into an adaptive masking of higher efficiency. The outer mask helps to eliminate headrest, embedded patient information and some peripheral parts from nasal images.

During speed test, a complete dataset of 34 images got segmented in less than 11 seconds in a computer having a 64-bit operating system, 8 GB RAM and processor of Intel® Core™ i7-3770 CPU @ 3.40GHz. Because of having guaranteed '0' FN, there is 0% chance of missing brain in any image. During segmentation enhancement, averaging and noise reduction operations which can modify pixel values of an image are avoided intentionally to keep the segmented output unaltered with respect to the original images, to offer no change or removal of diagnostic information.

Along with hemorrhage, other brain diseases which offer visible intensity change in head CT scan can be detected from these segmented brains as the complete intracranial matter is segmented successfully. The only issue is the

inclusion of non-intracranial information in few nasal images. This will have less effect during hemorrhage detection when the entire dataset will be considered. Once hemorrhage location will be identified in an image, a query based on disease location and other characteristic information will run through adjacent images. It will narrow down the search area and will not be much affected by the inclusion of small non-intracranial parts during brain segmentation. This hemorrhage segmentation technique is discussed in details in the next chapter.

Chapter 4

Hemorrhage Segmentation

Overview

This chapter proposes an intelligent knowledge driven method to segment hemorrhage from already segmented brain matter images, using the information of pixel intensity population and distribution. A mathematical model is designed to identify the unexpected variation in pixel intensity population in a brain CT image having hemorrhage. Complete batch of multi-slice CT scan images is taken as the input. Fusion of brain anatomy knowledge with the intensity distribution information of CT brain image, results in an unique solution for hemorrhage segmentation. To test the robustness, segmentation of different type of hemorrhage of different patients, is done using the proposed method. The results are accepted and validated by radiology experts. A fully automatic and fast CAD is designed, using the proposed method, to segment hemorrhage automatically in the absence of an expert, to assist the practioners for further inspection of hemorrhage. Competence of the CAD is tested against most used established clustering methods to demonstrate its potential.

4.1. Introduction

As per radiology, 'hemorrhage' in brain CT images, is an unexpected bright patch which is made of local collection of high intensity pixels within an average intensity brain matter region. Pathologically, inclusion of hemorrhage patch happens due to local blood collection in central nervous system or within meninges below the skull. In case of rupture in blood vessels, blood comes out of the vessel and accumulates in the local tissue area. With increase in the volume, leaked blood creates space in the neighborhood region and spreads gradually. Blood has higher x-ray absorption capacity than soft tissues. The accumulated blood, hence, absorbs higher amount of incident rays, than surrounding tissues when subjected under x-ray CT scan. As a result, in the CT image, a brighter spot is seen within the gray region as depicted in figure 4.1. This difference in pixel intensity is considered as principal feature to locate hemorrhage in a brain CT image.

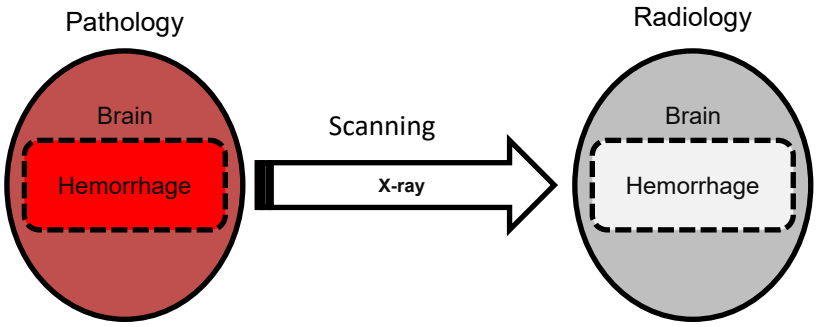

Figure 4.1: Brain hemorrhage from pathology to radiology

As already discussed in chapter 2, CT machine can capture large number of images during head scan. Manual identification of images which are affected by hemorrhage is hectic and time consuming for the practitioner.

Hemorrhage identification must be preceded by identification of dataset - as normal or hemorrhage, to minimise unnecessary time investment. Only the hemorrhage affected dataset will be considered for diagnosis and treatment. Researchers proposed different methods to classify the diseased images from the dataset automatically using computer's artificial intelligence and computational power. S. A. Kabara et al [142] extracted and compared three texture features, variance, correlation and sum average from the normalized

image slices. Using set of values of these three features, they classified most of the image as normal or abnormal, but few slices left with no clear decision. The use of tree classification has made this process simple, fast, robust and efficient. M. Chawla [16] approach starts with image enhancement, detection of mid-line and separation of symmetric halves of the brain through mid-line. Absolute feature values are not considered for classification in this work. Comparative status is used to take decision of classification. Histograms of both the halves are compared for primary stage classification. Further modification in classes is done by comparing corresponding energy values, after five levels wavelet decomposition of histogram of each half. This process has demonstrated a good accuracy. A simple but effective modification in normal and diseased slice classification is proposed by A. R. Fallahi [143]. Before doing classification using texture features, a morphological operation is applied on each slice. It offers a smoothing along with filling of small holes and removal of tiny unwanted isolated regions. M. M. Kyaw [144] proposed a method where detection accuracy is improved through elimination of non-diseased part of the image. After removing artifacts and skull, each image slice is divided into four parts. Mean and standard deviation of each part is calculated and compared for easy elimination of the normal parts. In a more recent paper, A. H. Ali et al [145] has demonstrated the power of first order texture features for identification of abnormal images. Each feature is compared and its relative value for abnormal images is discussed.

We have proposed a simple texture feature based classifier, for labeling data as normal or identify as a hemorrhage, before searching and finalizing the location of hemorrhage. Texture feature extraction is done from segmented brain images. The method is discussed in details in the respective section of this chapter.

There are few CAD systems already reported for hemorrhage segmentation as discussed in chapter 1. But room for more research is still open [73] due to lack of accuracy in the segmentation of reported systems, complex coding, difficulties in integration with real-time machines, less user-friendliness etc.

In this chapter, a simple, fast and robust CAD is proposed for hemorrhage segmentation from intracranial brain region. Outline of CAD process is presented in figure 4.2. The intensity and density of the hemorrhage pixels within brain CT

images are explored to locate and segment out hemorrhage for further diagnostic requirements.

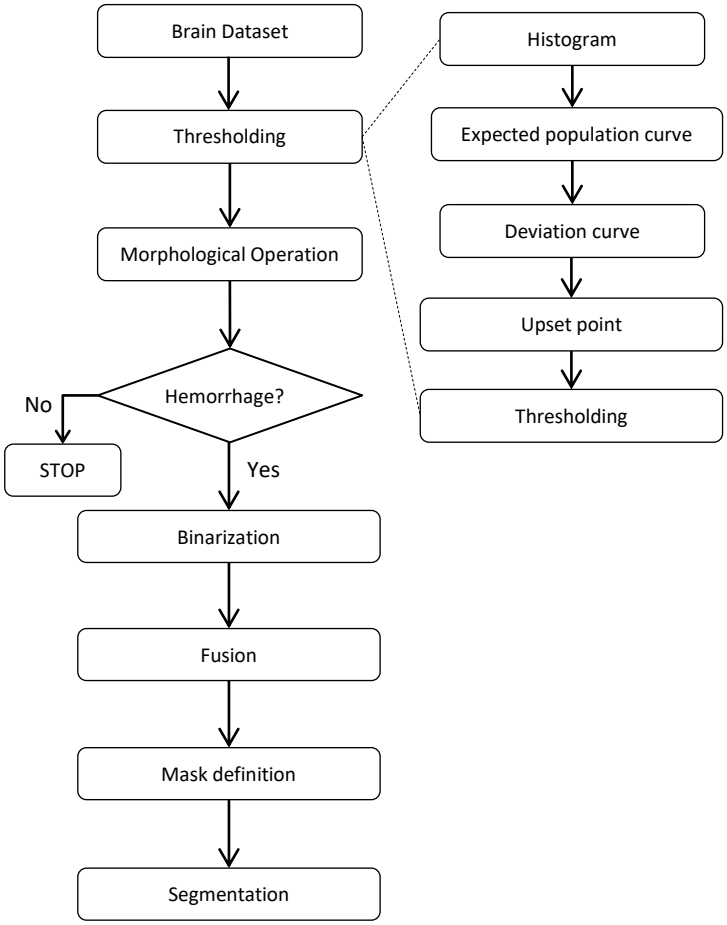

Figure 4.2: CAD process flow

4.2. Methodology

Already processed datasets of multi-slice brain CT images are taken for hemorrhage detection. This dataset has large number of pixels at background intensity level because of conversion of all non-intracranial information to background. The population curve of image shown in figure 4.3(b) is plotted in figure 4.3(a). 1st peak which is the largest one in this population curve represents the background. This peak is detected by CAD. In all clinical brain CT images, there is a sudden change in population after this peak. This change offers a very high slope. In between 1st highest peak and 2nd highest peak, the highest population deviation with respect to 1st peak is calculated and used to determine the background intensity threshold as shown in figure 4.3(c). The resultant image output is shown in figure 4.3(d). In short, the threshold value is the intensity at

which the intensity population deviation from the highest peak, created by background, is maximum. This value must lie between two highest population peaks of intensity histogram of a skull removed brain image. It has been considered that all intensity values other than the background carry clinical brain information. In the proposed work, hemorrhage is detected from these background removed pre-processed dataset by image analysis.

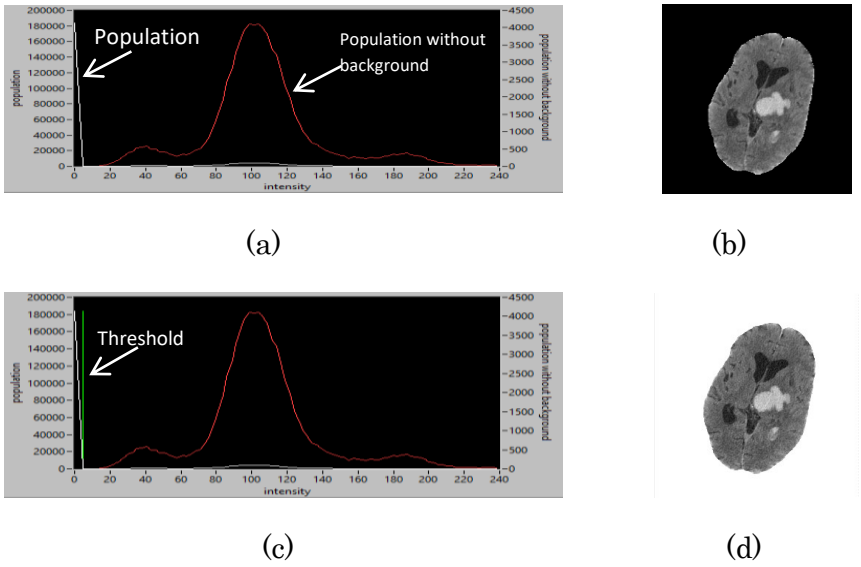

Figure 4.3(a): Population of intensity with and without background (b) Image under test (c) Background threshold (d) Background removed image

4.2.1. Segmentation of hemorrhage by population histogram

To segment hemorrhage from brain CT images, thresholding technique is used to find the target pixel cluster. We have considered two clusters – brain and hemorrhage. Cut-off between these two clusters i.e. threshold for hemorrhage is computed from image intensity population i.e. histogram analysis.

Pixel distribution of CT brain image is analyzed, based on count of pixels at different intensity level. Figure 4.4 is presenting histogram of three normal brain CT images after removing skull and background. These brain images are acquired from three different subjects. Depending upon the actual size of a CT image, amplitude and position of maximum population can vary; but the pattern of population distribution remains unaltered. The maximum population due to brain matter happens near the middle of the complete intensity range. At higher

intensity range the population reduces gradually and becomes very low near the end. Similar plots of patients' data are shown in figure 4.5. It has unchanged pattern for the initial part till the decreasing slope of highest peak, but a small bell shaped new peak is introduced due to hemorrhage which increases population in high intensity range. Threshold for hemorrhage lies near the end of downward slope of highest population peak and before the upward slope of newly introduced population peak. This work has proposed dynamic threshold finding to identify hemorrhage.

Expected population (eP) of an instance, is the statistically calculated population prediction from past population values. The value is calculated by taking moving average of available past, i.e. the lower intensity levels' frequency information for each instance as described in equation 4.1. Wide change in population pattern occurs twice, creating greater slopes around the highest population peak. These changes differ significantly from the expected population change, depicted from the history of population of previous intensities.

Expected population

$$eP_{i+1} = \frac{\sum_0^i P}{n} \tag{4.1}$$

where value for $(i+1)^{th}$ intensity level is calculated from all n past intensity level [0 to i] values.

The actual population and the expected population are compared in figure 4.6 (a) for CT image shown in figure 4.5(2). Actual population reaches the highest peak due to large no of pixels of brain matter. The expected curve does not follow the actual curve towards that peak. It increases its value slowly and reaches highest value at an intensity which is higher than the intensity at which actual population reaches highest value. After that intensity value, expected population decreases constantly but with very poor slope. It then meets the actual population value and offers zero deviation. The value of expected population remains higher than actual population beyond the zero deviation point, due to very high peak value of actual population.

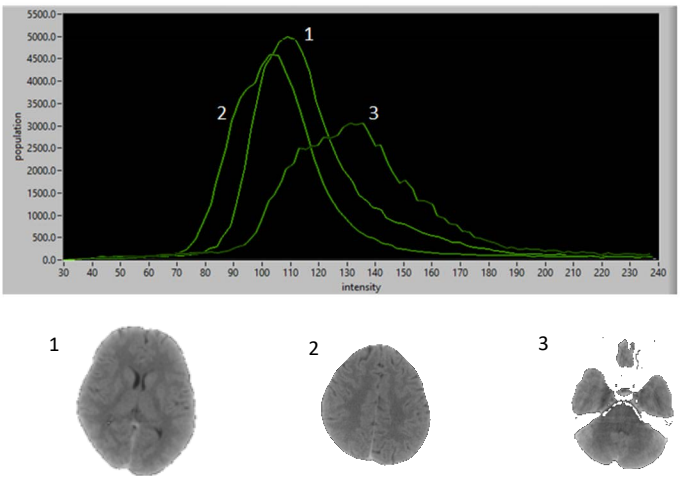

Figure 4.4: Intensity population distribution of image 1, 2, 3

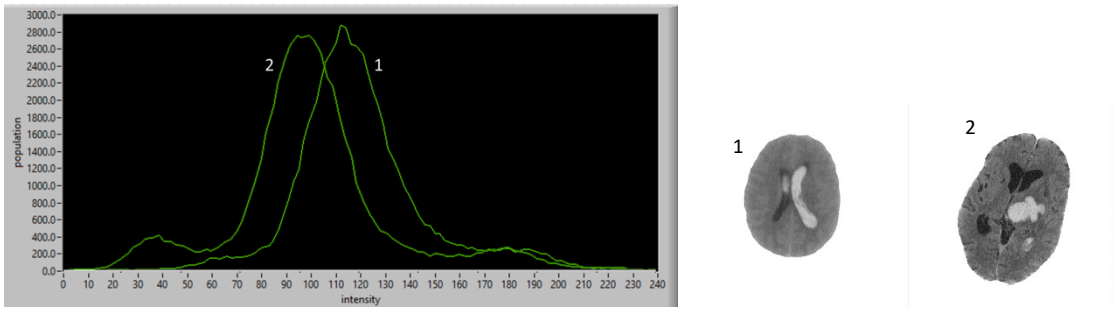

Figure 4.5: Intensity population for images with hemorrhage

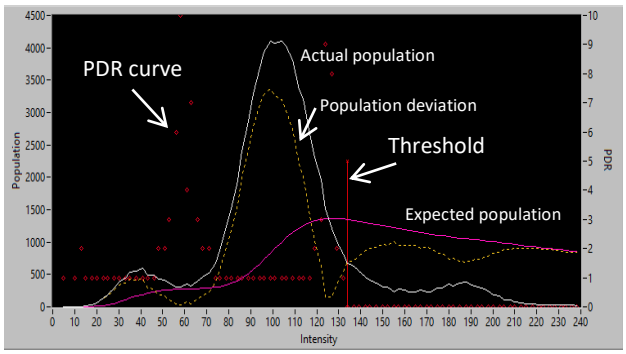

(a)

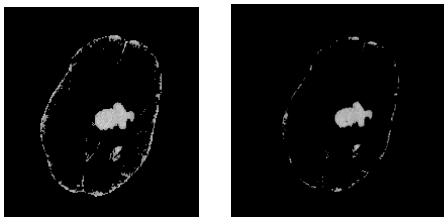

(b) *(c)*

Figure 4.6: (a) PDR and threshold (b) Segmented image (c) After morphological operation

A deviation curve, calculated using equation 4.2, is plotted to present the difference between actual and expected population. It is shown as a dotted line in figure 4.6 (a). Deviation reduces to minimum value as actual value approaches to

expected population. Beyond that intensity, deviation increases due to continuous fall of actual population and very low change in expected population.

$$\text{Deviation } D_i = |P_i - eP_i| \tag{4.2}$$

This calculated deviation curve presents the overflow or vacancy in pixel availability in actual population with respect to the predicted or expected population. Higher actual population symbolizes overflow, due to higher pixel availability than expected population, and the reverse represents vacancy due to deficiency in pixel population. The intensity value at which actual population meets expected population is the saturation point. Here the pixel availability of actual population is satisfied with the expected value. The situation becomes critical where deviation becomes higher than actual population. This happens due to very low strength of actual population with respect to expected population. That switching point on population graph is mentioned as upset point in this work. This upset point intensity is considered as threshold for hemorrhage in a brain CT scan.

Mathematically that threshold intensity value is calculated by taking Population to Deviation Ratio (PDR) stated in equation 4.3. Actual population, P, is divided by deviation, D, which is the difference between actual population value and its respective expected population value. At the upset point, PDR becomes less than 1, as the available frequency is lower than the calculated deviation.

Population to deviation ratio,

$$\text{PDR} = \frac{P}{D} \tag{4.3}$$

Where P presents the population or histogram data and D presents the deviation curve. Deviation curve D can be calculated as follows –

$$D = |P - eP|$$

$$\because \text{PDR} = P/|P - eP|$$

$$= 1/|1 - eP/P|$$

The nature of PDR is dominated by the factor μ, wher $\mu = 1 - eP/P$. $\mu > 0$ for $eP < P$, $\mu = 0$ for $eP = P$, $\mu < 0$ for $eP > P$. As absolute of denominator is taken, PDR will remain positive non-zero for any other conditions than eP=P.

At upset point, PDR will switch from PDR ≥1 to PDR<1 as D > P at that point. For PDR<1 the equation can be written as

$$\frac{1}{\left|1-\frac{eP}{P}\right|} < 1$$

$$\text{or, } \left|1-\frac{eP}{P}\right| > 1$$

so it can be rewritten as $\frac{eP}{P} - 1 > 1$

$$\text{or, } \quad eP > 2P$$

So the threshold for hemorrhage in a brain CT image is that intensity at which expected population becomes higher than twice of its actual population.

As per anatomy, hemorrhage intensity is always higher than brain matter intensity. So, to reduce computational load and to avoid any unexpected error, the threshold search is limited in the intensity region higher than the highest - peak in the background and skull removed histogram. After highest peak in the population curve, the 1st upset point intensity is taken as threshold for hemorrhage. PDR, along with the actual population, expected population and deviation curves are shown in figure 4.6 (a) for figure 4.5 (2). The upset point or threshold intensity for hemorrhage is shown here by a straight line. The segmented image with hemorrhage keeps all values above threshold and rest are converted to background as shown in figure 4.6 (b).

(a) (b)

Figure 4.7: Thresholding result of normal brain image

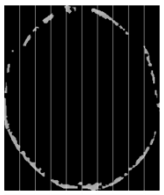

Figure 4.8: Vertically divided image

4.2.2. Removal of normal dataset

This thresholding method introduces noise due to the presence of the residual skull part in an image irrespective of its disease status. The segmented image shown in figure 4.6 (b) contains hemorrhage as well as some non-hemorrhage skull adjacent parts. To improve segmentation result, segmented image goes through single iteration erosion. This morphological operation shows high impact on deleting skull left out parts as shown in figure 4.6 (c). A normal

image without any hemorrhage also returns some non-hemorrhage parts as shown in figure 4.7 (a). Single iteration erosion of a normal image is shown in figure 4.7 (b). Such images can introduce error in further analysis and reduce performance accuracy of the system.

To identify an image as normal or diseased, classification is done using artificial neural network. Each image is first divided into 10 sub-images vertically as shown in figure 4.8. For each sub-image the value of IPF, along with the texture features, is extracted. For a single image, each feature results into an one dimensional array of 10 elements. A single value is derived from such array to represent the respective feature as the classifier input. This value is evaluated by clustering using mean shift algorithm [146].

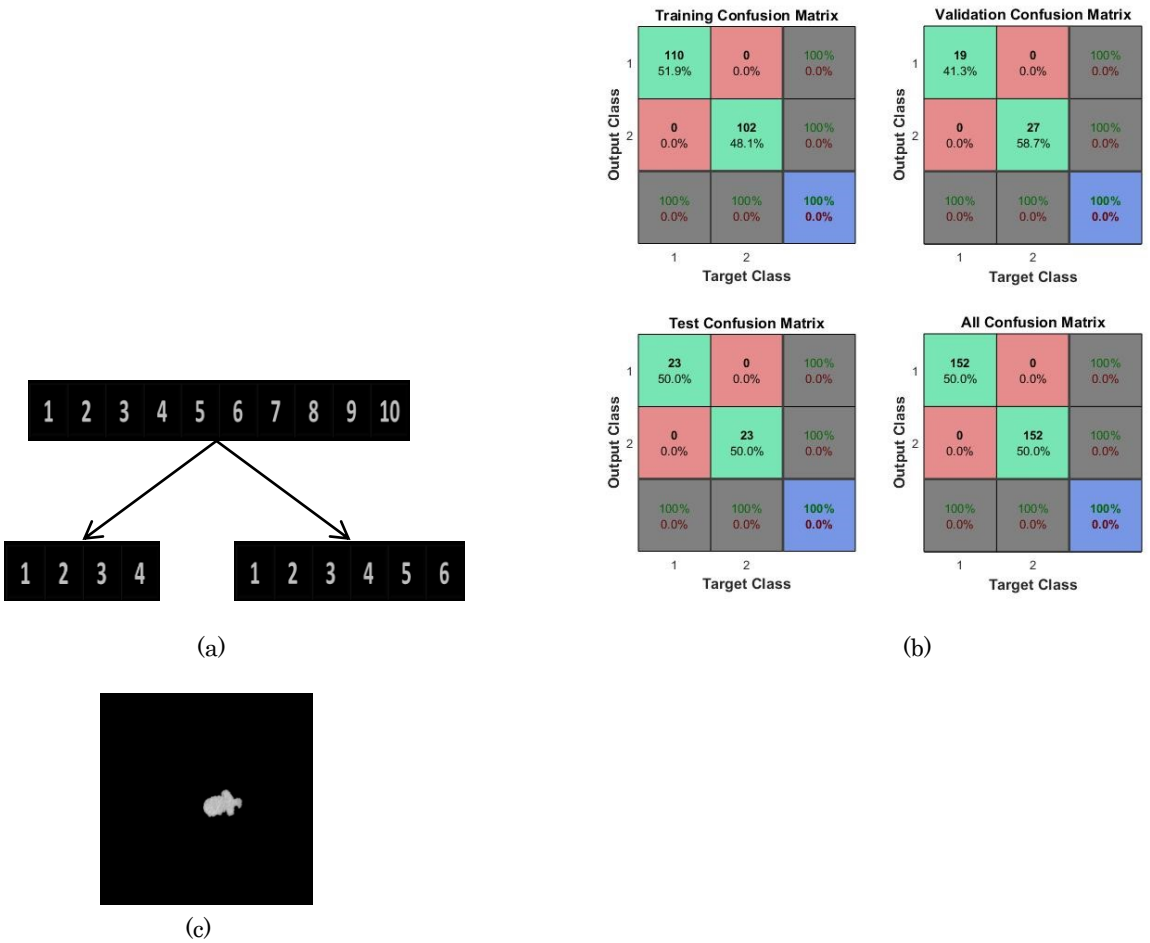

Figure 4.9: (a) Feature array to subsets, (b) Confusion matrix, (c) Selected hemorrhage

The elements of the one dimensional array, are divided into two subsets depending on their Euclidian distance from initial seed points [147]. The highest and lowest values of the array are selected as initial seed points of two sets, say S1

and S2. Rest of the elements are assigned to a set whose seed point has lower distance from that element. Mean of each set is evaluated and assigned as seed point of corresponding set. All the values are rearranged as per their distance from new seed points. These two steps, calculating new seed points and rearranging data, are repeated until no change is noticed. This mean shift process results into two final sets as shown in figure 4.9 (a). Euclidian distance between the two seed points of final sets is taken as representative of the corresponding feature.

IPF and three GLCM features, entropy, homogeneity and variance, are considered for classification. IPF predicts the number of foreground pixels, in this case the high intensity pixels, available in the thresholded images. Entropy varies with the increase in intensity span i.e. unevenness of image texture. The variance signifies higher intensity co-occurrence values. Homogeneity represents repetitiveness of the image texture. For hemorrhage affected images, difference between seed points are different than normal images. In case of normal images, only skull residues which are adhered to the boundary are present. The amount is significantly low. Final feature value remains low for normal images.

Classification is done using neural network. To train and validate the neural network, 152 normal and 152 hemorrhage images have been used. These images are not part of the dataset under test. The neural network returns 100% accuracy as presented in confusion matrix of figure 4.9 (b). Using the trained network, the entire database of 27 hemorrhage dataset and 16 normal dataset is classified. When no image in a dataset is labeled as diseased, the patient is considered as normal. No further inspection is required for such dataset. Rests of the dataset are further evaluated to locate the hemorrhage. The trained classifier has misclassified 2 normal datasets as diseased. Hence the accuracy drops to 95.35%, but sensitivity of classifier remains 100% because of no false negative selection.

If the dataset is labeled as diseased, hemorrhage location search is initiated. Largest connected part of an image, obtained from morphological operation, is identified as a hemorrhage. Any available non-zero information attached to that area in the pre-erosion image is reconsidered for reconstruction of

the hemorrhage. The segmentation result after reconstruction is shown in figure 4.9 (c).

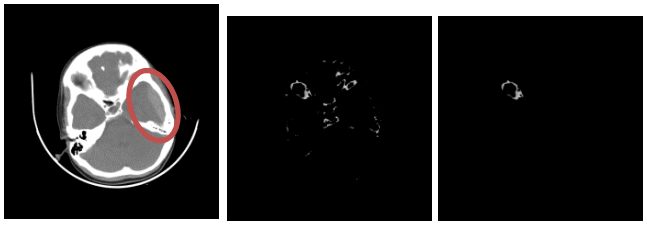

(a) (b) (c)

Figure 4.10: (a) Original image (hemorrhage is marked by circle) (b) Segmented image (c) Output after morphological operation.

4.2.3. Fusion and Mask definition

Sometimes in some images, due to other compact larger area of matching intensity, the actual hemorrhage does not get detected by the CAD as shown in figure 4.10. In figure 4.10 (a) hemorrhage is marked by a circle. In figure 4.10 (b), we can see only a few scattered pixels segmented form hemorrhage area. The largest connected area shown in figure 4.10 (c) is not a part of actual hemorrhage. To solve the problem, binarization of all segmented images of a dataset is done. Then the images are stacked up one after another and fused linearly. Correctly segmented images offer overlapping areas, whereas wrongly segmented images result into different scattered areas. After the linear fusion, the highest strength area is selected as hemorrhage zone. This hypothesis is elaborated by a 6X6 matrix here.

Say, dataset D has total 5 images, each of which is a 6X6 matrix. I_1 to I_5 are the images after segmentation and morphological operations, where 0 represents deleted brain, non-brain and background part. f represents high intensity brain part, h is the hemorrhage.

$$I_1 = \begin{bmatrix} 0 & 0 & 0 & 0 & 0 & 0 \\ 0 & 0 & 0 & 0 & 0 & 0 \\ 0 & h & 0 & 0 & 0 & 0 \\ 0 & h & 0 & 0 & \mathbf{f} & 0 \\ 0 & 0 & 0 & \mathbf{f} & \mathbf{f} & 0 \\ 0 & 0 & 0 & 0 & 0 & 0 \end{bmatrix} \quad I_2 = \begin{bmatrix} 0 & 0 & 0 & 0 & 0 & 0 \\ 0 & 0 & 0 & 0 & 0 & 0 \\ 0 & \mathbf{h} & 0 & 0 & f & 0 \\ 0 & \mathbf{h} & 0 & 0 & f & 0 \\ 0 & \mathbf{h} & 0 & 0 & 0 & 0 \\ 0 & 0 & 0 & 0 & 0 & 0 \end{bmatrix} \quad I_3 = \begin{bmatrix} 0 & 0 & 0 & 0 & 0 & 0 \\ 0 & 0 & 0 & 0 & f & 0 \\ 0 & \mathbf{h} & \mathbf{h} & 0 & 0 & 0 \\ 0 & \mathbf{h} & 0 & 0 & f & 0 \\ 0 & 0 & 0 & 0 & 0 & 0 \\ 0 & 0 & 0 & 0 & 0 & 0 \end{bmatrix}$$

$$I_4 = \begin{bmatrix} 0 & 0 & 0 & 0 & 0 & 0 \\ 0 & \mathbf{h} & 0 & 0 & 0 & 0 \\ 0 & \mathbf{h} & \mathbf{h} & 0 & 0 & 0 \\ 0 & 0 & 0 & 0 & 0 & 0 \\ 0 & 0 & 0 & 0 & 0 & 0 \\ 0 & 0 & 0 & 0 & 0 & 0 \end{bmatrix} \quad I_5 = \begin{bmatrix} 0 & 0 & 0 & 0 & 0 & 0 \\ 0 & 0 & 0 & 0 & 0 & 0 \\ 0 & \mathbf{h} & 0 & 0 & 0 & 0 \\ 0 & \mathbf{h} & 0 & 0 & 0 & 0 \\ 0 & 0 & 0 & 0 & 0 & 0 \\ 0 & 0 & 0 & 0 & 0 & 0 \end{bmatrix}$$

The largest part of each image is highlighted using bold font. Now, all the pixels in the largest part are converted to value 1 and rest to 0.These binary images are then added linearly and resultant image I becomes –

$$I = \sum_{1}^{5} I_{g_i} = \left\{ \left\| \begin{bmatrix} 0 & 0 & 0 & 0 & 0 & 0 \\ 0 & 1 & 0 & 0 & 0 & 0 \\ 0 & 4 & 2 & 0 & 0 & 0 \\ 0 & 3 & 0 & 0 & 1 & 0 \\ 0 & 1 & 0 & 1 & 1 & 0 \\ 0 & 0 & 0 & 0 & 0 & 0 \end{bmatrix} \right\| \; f = 1 \text{ for } I_1, h = 1 \text{ for other than } I_1 \right\}$$

Where I_g presents segmented binary images. The strength of two areas is evaluated as S_h and S_f.

$$S_h = \sum\{I|\, f = 0\} = \sum \begin{bmatrix} 0 & 0 & 0 & 0 & 0 & 0 \\ 0 & 1 & 0 & 0 & 0 & 0 \\ 0 & 4 & 2 & 0 & 0 & 0 \\ 0 & 3 & 0 & 0 & 0 & 0 \\ 0 & 1 & 0 & 0 & 0 & 0 \\ 0 & 0 & 0 & 0 & 0 & 0 \end{bmatrix} = 11$$

and similarly $S_f = 3$.

For final hemorrhage segmentation, pixel locations of highest strength area are saved to create a mask. Each segmented slice is then tested against that mask to see if any information in that area or in adjacent area, is available. All positive response locations are selected as hemorrhage candidate for the respective image. The success of this backpropagation information collection is presented in figure 4.11 for the image shown in figure 4.10 (a). It shows that the largest area selected in figure 4.10 (c) is cancelled and the actual area marked in figure 4.10 (a) is selected as hemorrhage by mask.

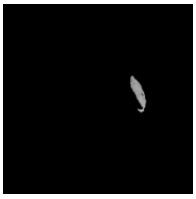

Figure 4.11: Segmented hemorrhage

4.3. Result

The proposed CAD is unsupervised, fully automatic system. Efficiency of this proposed segmentation technique is tested against popular segmentation methods to establish its potential. In case of data sets segmentation, Liu et al., 2009 [148] and Y.G.Jung et al., 2014 [149] have demonstrated the power of K-means clustering method over Otsu and Expectation Minimization methods respectively. As discussed in chapter 1, Dundar et al., 2015 [71] has shown that unsupervised K-means technique outperforms several deep learning techniques when implemented on a small dataset. Fuzzy C-means method is an advancement of K-means method [150]. So, we have compared the performance of proposed method with K-means and fuzzy C-means segmentation. In figure 4.12 the segmentation results are shown with ground truth annotation.

In result 2, hemorrhage segmentation annotation (blue line) is overlapped with ground truth and thus not visible. Non-hemorrhagic segmented areas are not marked but visible in the segmentation result. Two class segmentation offers poor distinguishability for both the techniques. With the increase in number of classes, the segmentation method increases its sensitivity. But even after segmenting for six classes the proposed method outcome remains ahead in the competition.

As per the expert's opinion, hemorrhage patch detection using proposed CAD satisfies the ground truth for all the cases under test. It also has successfully collected hemorrhage information from dataset having low volume hemorrhage. Though initially in few images of some datasets, wrong areas are labeled as hemorrhage, after fusion and final selection those are nullified and the ground truth is satisfied.

For further analysis, quantitative evaluation in term of sensitivity, accuracy and dice coefficient of proposed segmentation method is carried out. The basic concept of dice coefficient is discussed in Appendix C. Results of 27 datasets of CT brain hemorrhage are presented. The dice coefficient shows that each dataset is segmented with enough similarity with ground truth marked by experts. Calculated average dice coefficient value is 0.9205. Evaluated results are collated in table 4.1. For proposed method sensitivity lies in between 70%-100%, with an average of 93.47%. Average error is 6.81% and average accuracy is 93.19%.

Accuracy, sensitivity and dice coefficient of proposed method are compared with that of K-means and fuzzy C-means methods for k=6. To do segmentation using K-means and fuzzy C-means, the program flow described in figure 4.2 is kept unaltered; only 'hreshold finding' and 'binary segmentation' steps are replaced by respective method. Average accuracy and sensitivity for K-means is 80.74% and 67.29%, for fuzzy C-means is 90.17% and 76.96% respectively. Comparison graphs shown in figure 4.13 to figure 4.16 demonstrate the power of proposed method over the other conventional two.

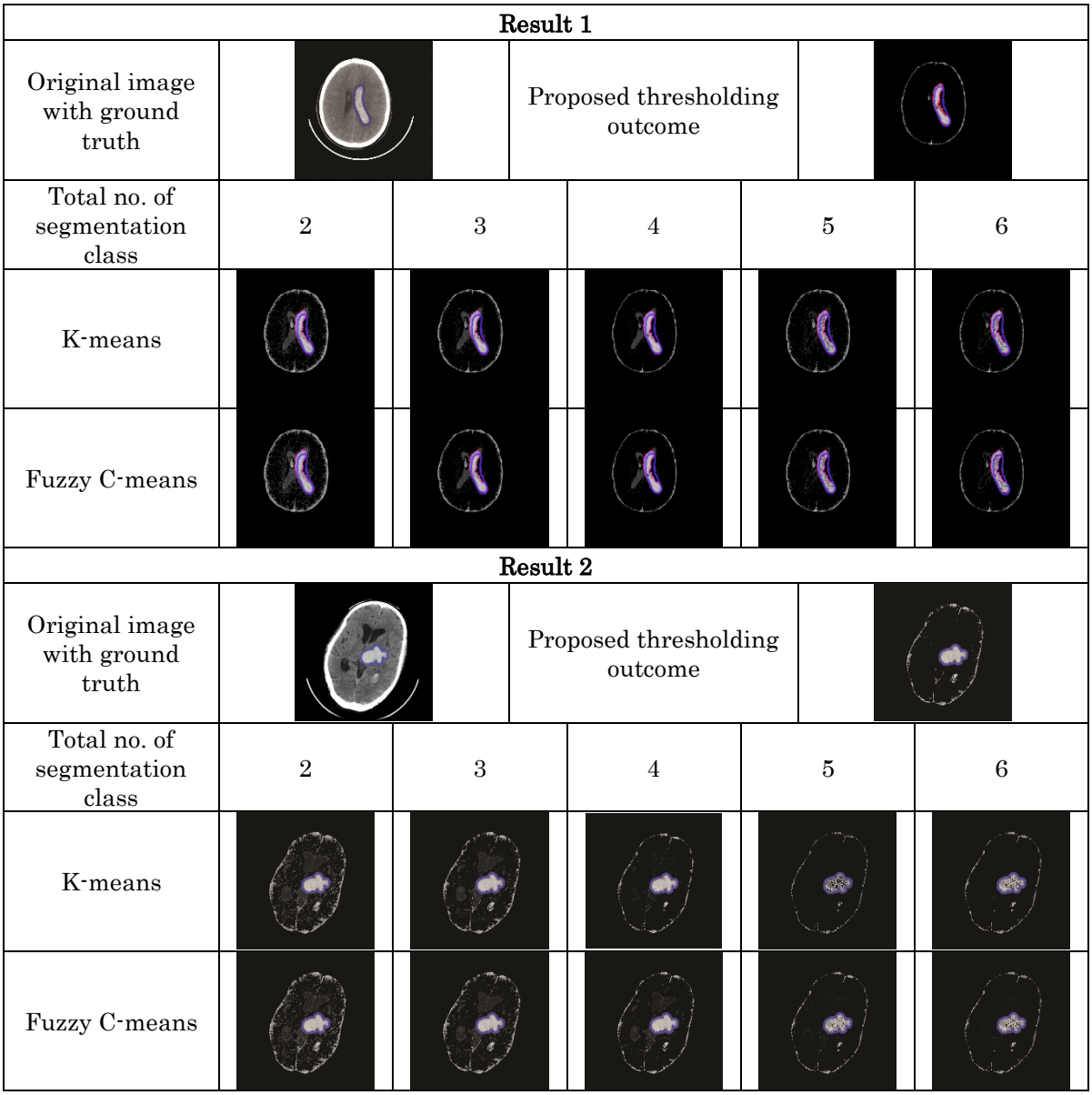

Figure 4.12: Thresholded images are compared. The blue line is used to show the ground truth and pink line to show segmented area of hemorrhage.

Regardless of this, no hemorrhage dataset is treated by CAD as normal dataset i.e. no false negative diagnosis by this CAD. This turns the CAD

sensitivity (true positive by CAD/true positive as per ground truth) to 100%. As per practitioners, higher sensitivity is most important requirement for any clinical support system to avoid risk of treatment delay or life loss due to wrong diagnosis.

The proposed thresholding technique takes 4.79 seconds to segment a 36 slices dataset when run in a computer having 4 GB RAM, Intel® Core(TM) i3 processor running at 2 GHz speed and 64 bit Windows 10 OS platform. In the same system, segmentation of the same dataset by K-means and Fuzzy C-means take 4.9 seconds and 5.2 seconds respectively when each slice is segmented in two clusters. Required time increases with increase in number of clusters. Segmentation times are compared in figure 4.17. Time required for K-means and fuzzy c-means clustering for both k=2 and k=6 are compared with time required for proposed thresholding method. As per the result, proposed method has outperformed the other two methods.

Dataset	%Sensitivity	%Accuracy	%Dice coefficient
1	90	96.43	91.81
2	77.78	93.33	96.72
3	100	92.86	95.37
4	83.33	92.86	98.78
5	100	95.65	89.35
6	100	100.00	90.87
7	100	88.00	91.06
8	100	84.62	94.4
9	90.91	92.31	92.44
10	81.25	88.00	92.17
11	100	76.92	93.78
12	100	100.00	92.5
13	80	80.77	92.83
14	100	100	95.78
15	92.31	97.06	95.58
16	100	96.43	91.81
17	87.5	96.43	96.62
18	89.47	93.75	95.87
19	100	100.00	98.58
20	100	100.00	84.56
21	94.44	96.43	92.72
22	100	72.00	68.13
23	92.86	96.43	93.12
24	88.89	96.43	91.01
25	100.00	100.00	92.13
26	75.00	89.47	87.47
27	100.00	100.00	89.97
Average	**93.47**	**93.19**	**92.05**

Table 4.1: Sensitivity, accuracy and dice coefficient analysis of proposed method

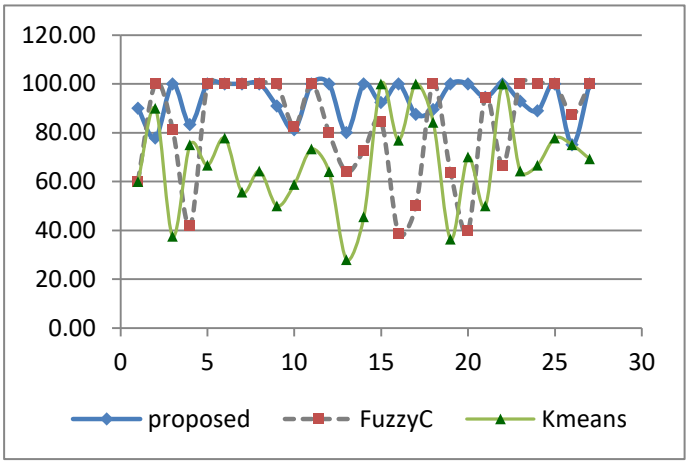

Figure 4.13: Comparison of %sensitivity of three methods

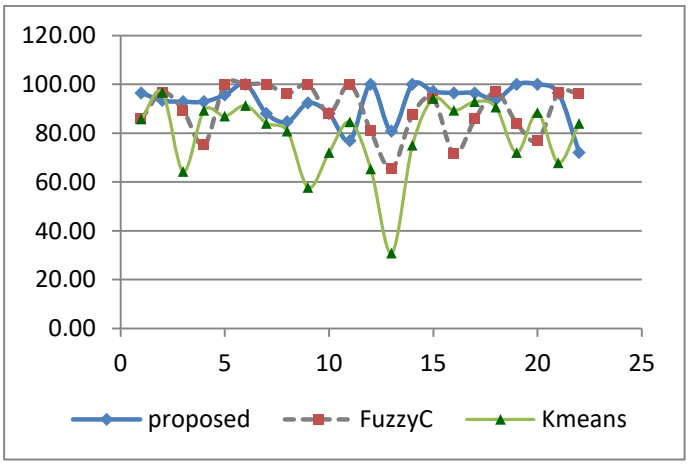

Figure 4.14: Comparison of %accuracy of three methods

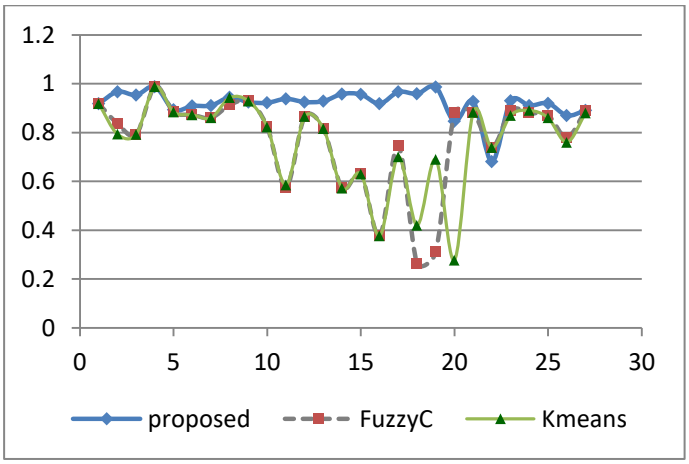

Figure 4.15: Comparison of dice coefficient of three methods

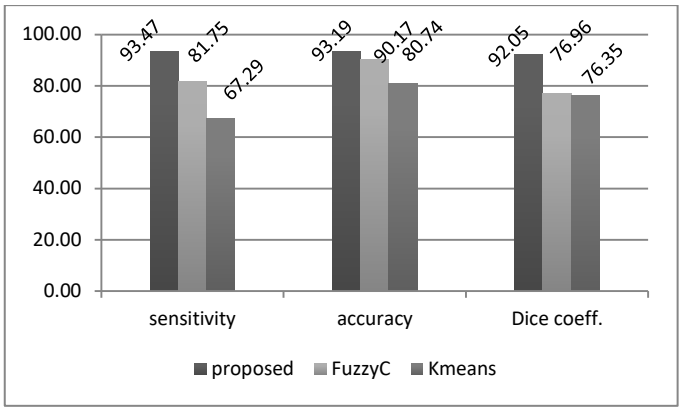

Figure 4.16: Comparison of average of %sensitivity, %accuracy and %Dice coefficient

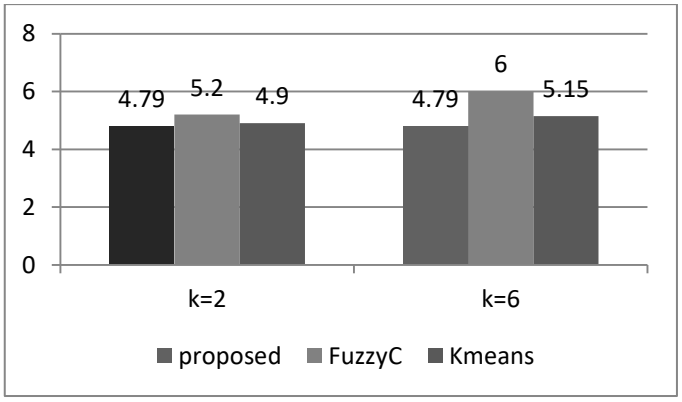

Figure 4.17: Comparison of segmentation time (in seconds) of three methods (k value varies for traditional methods, for proposed method it is 2 for both the cases.)

There are different works already presented by researchers for hemorrhage segmentation as discussed in state of the art section. Two [78, 151] of such works have significant resemblance with the proposed work. Quantitative analysis of these two works is compared with our proposed work.

Shahangian et al. have presented automatic hemorrhage segmentation from brain CT images with good accuracy. But three major deficiencies are noticed in this research - selection of initial thresholds, brain matter segmentation, and threshold value selection for hemorrhage segmentation.

In the article, background and skull are removed by absolute threshold values 100 and 225 respectively. In many cases, parts of brain, as well as parts of hemorrhage, are removed by those fixed threshold values. No restoration method is proposed to recover such parts. An example of such case is shown in figure 4.18. Adaptive threshold selection process of the proposed method has proven advantages over method proposed by Shahangian et al. In the next step, they

proposed selection of brain by selecting the largest connected area. Disadvantages of this method are already discussed in the previous chapter with examples.

Finally, there is no clue given in the article about threshold selection for hemorrhage. Rather it has been stated as "we define an appropriate threshold", though the process is claimed to be automatic. This is the most important part, on which automatic hemorrhage segmentation and accuracy of the system is highly dependent. Hence the quantitative analysis presented in their paper remains questionable.

An integrated process is proposed by Bhadauria et al. It offers better result than Chen and Vese method, region growing technique and fuzzy C means method. They have used active contour method, along with FCM to improve the performance of the process. The performance parameters of this method and Shahangian's method are assembled and compared with our proposed method in table 4.2.

It has been observed that the potential of the proposed method is much higher in terms of sensitivity, dice similarity and specificity. Only Shahangian's method is claiming higher accuracy, justification of which is not found in their article and the reported dice coefficient is very poor. Another important advantage of the proposed method is its image handling capacity. It can segment hemorrhage from all affected images of a dataset in a single run of the program, whereas, other two methods can segment one image at a time.

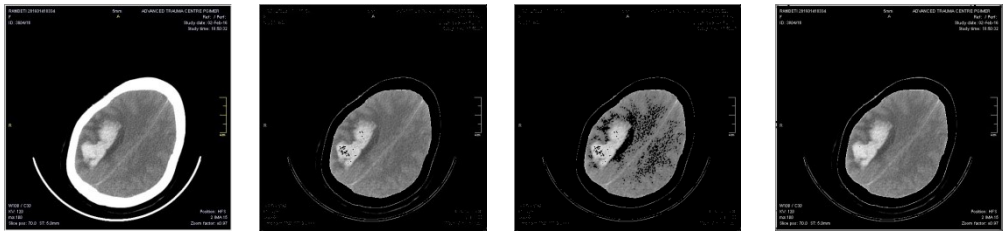

(a) *(b)* *(c)* *(d)*

Figure 4.18: (a) Original image (b) Skull removed by threshold 225 (c) Background removed by threshold 100 (d) Adaptive thresholding for skull and background

	Sensitivity	**Specificity**	**Dice coefficient**	**Accuracy**	**Image handling capacity**
Shahangian [151]	85.27	96.05	83.69	**93.80**	Single image
Bhadauria [78]	80.67	99.58	87.58	86.24	Single image
Proposed method	**93.95**	**100**	**92.35**	92.45	**Multislice scanned data**
Advantage observed in	Proposed method	Proposed method	Proposed method	Shahangian	Proposed method

Table 4.2: Comparison chart of Shahangian, Bhadauria and proposed methods' results

4.4. Discussion & Conclusion

The objective of this chapter is to design a fast, efficient, easy to use and reliable methodology for hemorrhage segmentation from already segmented ROI images. The proposed system's potential lies in zero false negative in final decision. The segmentation results are reviewed and approved by doctors of radiology department, from PGIMER, Chandigarh, India. Proposed CAD is a threshold based technique. To find threshold automatically from intensity population, prior knowledge of brain anatomy and CT image intensity distribution for brain and hemorrhage have been used.

The proposed unsupervised technique based CAD is expected to be helpful for critical situation like remote diagnosis support, absence of expert practitioner and bulk patient management due to an accidental emergency. This method requires no human interaction for segmentation; whereas K-means and fuzzy C-means need human interpretation to find right cluster among multiple output clusters. For example, an expert is required to select a particular cluster containing hemorrhage for 'n' times when the complete dataset contains 'n' slices. So these methods are unable to fulfill our requirement of using the CAD in absence of a practitioner for hemorrhage segmentation. In the next chapter the segmented hemorrhage are further analyzed for classification.

Chapter 5

EDH & SDH Classification

Overview

Segmented hemorrhages are classified in this chapter. Relative location information of each hemorrhage with respect to the brain boundary is evaluated. This information potentially classifies the target candidates with 100% accuracy. This class is further classified into EDH and SDH. Shape features play a great role in this classification. Several shape features are extracted from hemorrhage shape and size. From the primary features, more relevant secondary information are computed. IPF and compactness are also evaluated. The entire set of features, is optimized to reduce the dimension of the classifier input. Features having higher degree of separability are selected for designing purpose. Neural network classifier is trained using optimized features to conduct final stage of classification. Proposed classifier offers highly accurate classification result.

5.1. Introduction

Significance of classification of a disease lies in its importance in medical systems. It facilitates practitioners by providing fast and reliable information to take decision and initiate treatments. Same disease may have different impact on patients' morbidity and mortality depending on its class. Classification of disease can be based on its topography, anatomy, physiology, pathology, etiology, epidemiology, statistics and juristic conditions. Each category has a specific angle to look at a disease, as discussed in table 5.1. A single disease can fall under one or more categories.

Category	Base concept
Topographic	The area affected by disease
Anatomic	The organ or tissue affected by the disease
Physiological	The effect of disease on physiological functions
Pathological	The nature of disease process
Etiologic	The general cause of the disease
Epidemiological	By the stage of the disease
Juristic condition	By speed of advent of death
Statistical	The statistical information of disease

Table 5.1: disease category

Brain hemorrhage is classified into several types depending on its location (topography) of occurrence. The major two classes are intra-axial and extra-axial hemorrhage. When blood is collected in the periphery of brain within the tissue layers just below skull, the type of hemorrhage is identified as extra-axial hemorrhage. Other blood accumulations which happen within the brain matter or ventricular area are known as intra-axial hemorrhage. These two classes are further divided into different subclasses as shown in the classification tree in figure 5.1 (a) [152]. As discussed in introduction section of chapter 4, blood gets accumulated around the leakage initially. With increase in volume, leaked blood puts pressure on surrounding tissues to create more space in neighbourhood region and starts spreading gradually. Hemorrhage blood spreading can be - uniform, one directional, bi-directional or irregular. In different areas of brain, bonding of tissues with its adjoining layers is different. This property of tissue

layers, controls the spreading direction of blood and the final shape of the hemorrhage patch.

Like different categories, nomenclature of brain hemorrhage is also based on topographic information of leakage area. This has made the name auto-descriptive as discussed below.

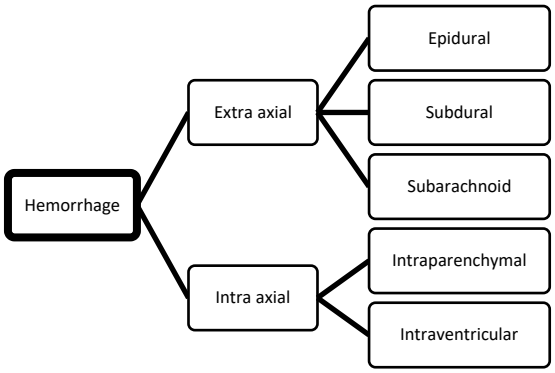

(a)

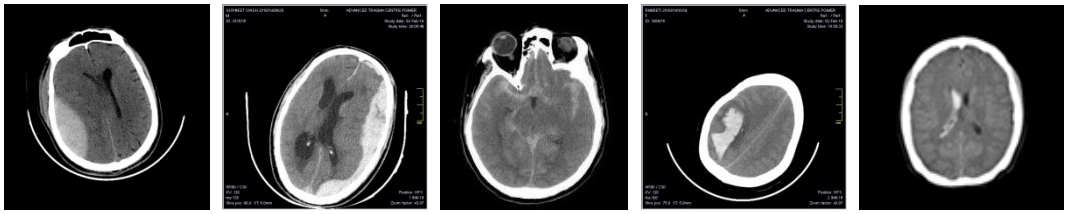

(b) *(c)* *(d)* *(e)* *(f)*

Figure 5.1: (a) Hemorrhage classes (b) EDH (c) SDH (d) SAH (e) IPH and (f) IVH

Epidural hemorrhage (EDH):

When due to rupture in the blood vessels, blood accumulates between the skull and the dura matter of brain, then the type of hemorrhage is identified as Epidural hemorrhage in short EDH.

Subdural hemorrhage (SDH):

When the leaked blood accumulates between the dura matter and arachnoid matter, then the type of hemorrhage is identified as subdural hemorrhage in short SDH.

Subarachnoid hemorrhage (SAH):

Pia matter is the innermost member surrounding the central nervous system. When leaked blood accumates between the arachnoid and pia natter of the brain, then the type of hemorrhage is identified as subarachnoid hemorrhage in short SAH.

Intraparenchymal hemorrhage (IPH):

Any blood accumulation within the brain parenchyma is referred to as intraparenchymal hemorrhage in short IPH.

Intraventricular Hemorrhage (IVH):

Cavities within the parenchyma, where cerebrospinal fluid is produced are known as ventricles. Any blood accumulation within this ventricular space is identified as Intraventricular hemorrhage in short IVH.

Among all types of hemorrhages, Epidural hemorrhage (EDH), subdural hemorrhage (SDH) and intraparenchymal hemorrhage (IPH) are the most common cases received in hospitals [80]. After discussion with radiologists, Subdural and Epidural hemorrhage (SDH & EDH) classes have been considered as major research targets, and rest of the cases are labelled as 'others' which include SAH and intra-axial hemorrhage. All these types of hemorrhage listed in figure 5.1 are shown in figure 5.1 (b)-(f).

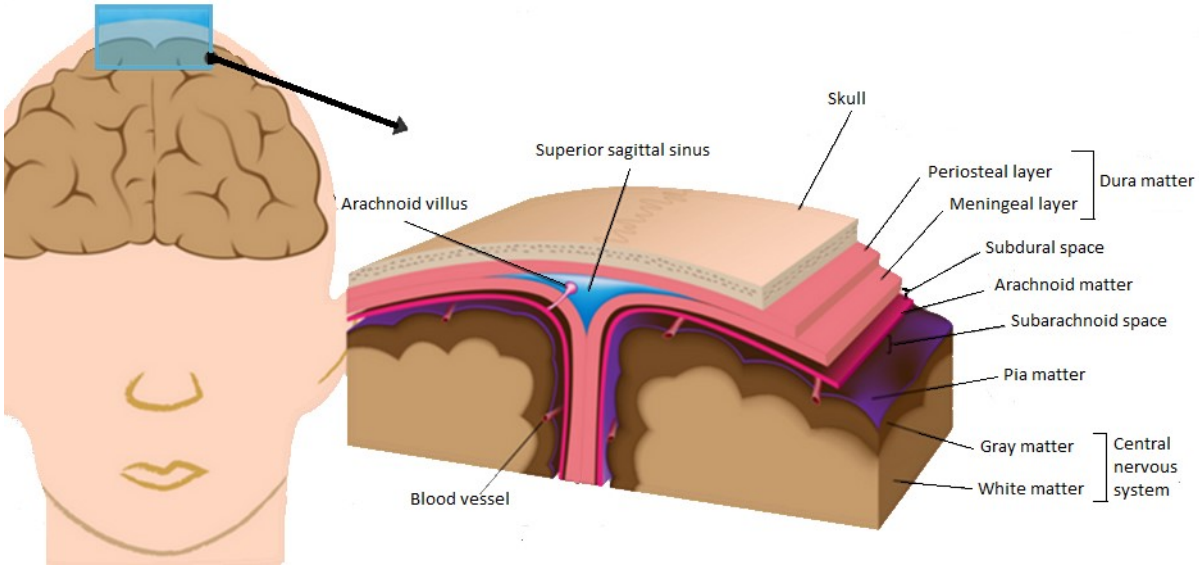

Figure 5.2: Cranial meninges

5.2. Image Features

For easy presentation and data compression, images are presented as set of features [153]. Conceptual sketch of cranial meninges surrounding brain's central nervous system is shown in figure 5.2. The location of different types of hemorrhage can be visualized easily as the name of each type of hemorrhage is

self-descriptive. If we start moving from the skull and trace the path towards the center of the brain, we gradually pass the layers associated with different types of hemorrhage, starting with EDH followed by SDH, SAH, ICH and IVH. Classification is a technique using which we can divide a large collection of subjects into smaller groups. Each group contains subjects which are similar with respect to some specific characteristic parameters. The parameters are selected as per the interest of end users. With the change in the parameters, the entitlement of an object to a subgroup can be changed depending on the correlation between the previous parameters and the newly selected parameters. If the new set is completely different from old set of parameters then the subjects will create completely different groups. With increasing similarity between the new and old parameter sets, the change in assigned class decreases. Characteristics parameter can be of three types for an image – color, texture and shape [154]. Set of features can be extracted from each of these three types of parameters. Some commonly used features are listed in the tree shown in figure 5.3. They can be used separately or in a combination, to increase accuracy in classification. Features extracted from local region of an image are considered as local features, whereas features extracted considering entire image as region of interest (ROI) are known as global features. Both types of features have its own significance in classification. Practically a large number of features can be extracted from available color, texture and shape information of an image [154]. For different target ROI same set of features can offer different values and show different potential in classification.

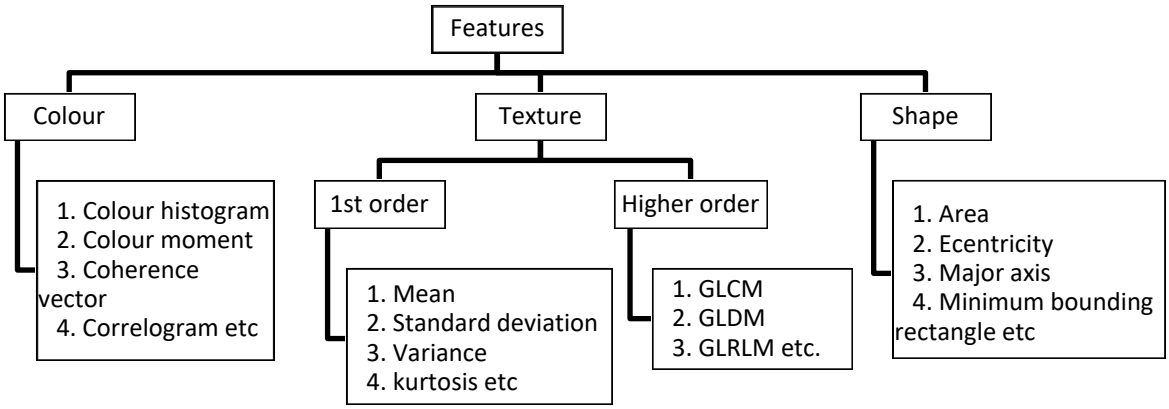

Figure 5.3: Image features

Color features are the most prominent visual features of an image. Color value and color distribution both can offer distinguishable and potential information for image classification. Mean variance and standard deviation etc. are calculated from color histogram. Spatial coherence of color is presented by features like coherence vector, correlogram, etc.

Texture features mathematically describe the visual pattern of image surface. A 3-dimentinal real world vision is presented in a 2-dimentional image by converting the surface information, like the pattern of roughness/smoothness and change in color/gray intensity etc., into proportional pixel intensity. Several statistical methods are used to extract information from the image. Information like mean, standard deviation, variance, kurtosis, skewness etc. which are extracted directly from pixel values, are called first order texture features. These features are mostly calculated from intensity histogram of the image. When relative pixel intensity information with respect to the neighborhood pixel intensity is evaluated, then the extracted features are called higher order texture features. If the immediate neighbors are considered for feature extraction, then the features are called 2nd order features. With the increase in distance between the target pixel and the neighbor, the order will increase. Different analyses methods like gray level co-occurrence matrix (GLCM) [19], gray level run length matrix (GLRLM) [20], gray level difference matrix (GLDM) [155] etc., are already proposed for higher order texture information extraction.

Shape features describe the shape of the ROI. It is normally extracted from the part of image to understand the local area information. Total area, perimeter, longest axis, eccentricity, circularity, rectangularity, convexity and much more information are extracted from the shape of ROI.

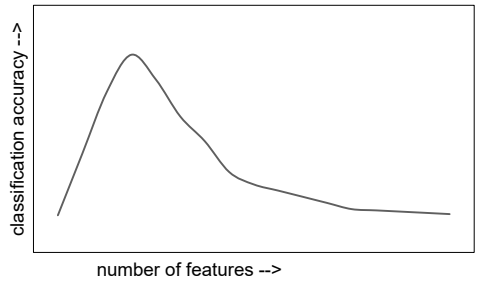

Figure 5.4: Performance of classifier

Each feature contains some information about the subject. So though it seems that more number of features means more information, but in practice the fact is something different. All features are not always useful, nor contributory. Few features offer no prominent discrimination for target classes. Such features are called irrelevant features. Irrelevant features are unnecessary computational load on classifier and sometimes create noise in output. Few features are redundant. Such features do not contribute anything significant. It has been observed that with increase in the number of features, the classifier performance improves initially but then starts falling as shown in figure 5.4. This happens due to inclusion of irrelevant and redundant features which confuse the classifier. So to optimize the performance of a classifier noise reduction is must. Irrelevant Feature elimination can be done by feature selection.

Elimination of less contributing features using search algorithms like optimum methods, heuristic methods or randomize methods - is called feature selection. These search algorithms use filtering or wrapping mechanism. The entire list of features is truncated to a lower dimension selecting top ranked or more contributing features. When a given set of features are projected to another plane of less dimensionality, the size of the newly extracted feature set gets reduced. The new features are then used as input of the classifier.

5.3. Hemorrhage features

As already discussed, classification solely depends on the unique features of the subject under test. Irrespective of their types, each and every hemorrhage is pathologically a liquid body formed by accumulation of blood. The x-ray absorption capacity of any hemorrhage is same. CT numbers offered by different hemorrhage are thus almost equal. Hence, in a CT image, type of hemorrhage cannot be classified depending on its HU. In non-contrast CT, no color information is available. The texture is almost homogeneous having no significant textural differences between classes. On the contrary, the anatomical information and shape of each type of hemorrhage vary from each other significantly. Several works demonstrated satisfactory accuracy in hemorrhage classification using shape features [13,24,151,156]. In our research work, we have considered a combination of different types of features to design a highly accurate classifier. A set of second order shape features, along with information packing factor, compactness and skull vicinity of the target ROI, are used as input parameters of the classifier.

5.3.1. Shape features

A shape is described mathematically by several parameters which have qualitative values in different aspects. Shapes of different hemorrhage are shown in figure 5.1 (b)-(f). EDH and SDH both are prominent blood collection near the skull with different bounding shapes. EDH has bi-convex boundary whereas SDH has crescent shape. The adjacent layers to the skull, are convex for both types of hemorrhages. Other side is convex for EDH but concave for SDH. SDH can be more extensive than EDH because it can cross cranial sutures and spread over the hemispheres.

SAH is another extra-axial hemorrhage. It is not as attached to the skull as EDH or SDH. A smaller part of subarachnoid hemorrhage body remains adjacent to the skull; rest gets spread in the subarachnoid space forming an irregular shape. Intaparenchymal and ventricular hemorrhage are formed by blood collections which are anatomically non-adjacent to the skull. The shape of IPH can be semi-circular or irregular with uneven boundary. IVH is formed within

the ventricle near the skull mid-line. Its shape changes with the increase in size in the shape of ventricle. A large IVH forms rounded edge crescent shape within the ventricle. Some commonly used primary shape features of the brain hemorrhage are collated in table 5.2 and pictorially described in figure 5.5.

	Shape feature [157]	Description
1	Area (A)	Count of total number of pixels in the hemorrhage patch is the measure of hemorrhage area.
2	Perimeter (P)	Total length of boundary of the hemorrhage body is the perimeter of that hemorrhage.
3	Major axis (M)	The longest available span in the hemorrhage body is considered as major axis of that hemorrhage.
4	Minor axis (m)	Longest available span in the perpendicular direction of major axis is the minor axis of that hemorrhage.
5	Equivalent circle (Ec)	The circle, area of which is equal to the area of hemorrhage, is denoted as equivalent circle.
6	Best fit circle (C)	The smallest circle which can envelope all pixels of the hemorrhage.
7	Best fit rectangle (R)	The smallest rectangle which can wrap the entire hemorrhage body.
8	Best fit ellipse (E)	The smallest ellipse which can wrap the entire hemorrhage body.
9	Inscribed circle	The best possible circle which can fit within the hemorrhage body.
10	Convex hull	Count of total number of pixels of the best fit polygon of the hemorrhage.

Table 5.2: Shape features

5.3.2. Additional features

Two primary features are modified to extract information about the continuity hemorrhage body along axes. As shown in the figure 5.5, major and minor axes are affected by rotation of the brain image. Inspection for these axes hence involves rotation correction or complex mathematics. To avoid this burden, in our research we have considered two alternative features, height (H) and width (W) of the hemorrhage. Maximum available length across x-axis and y-axis in the hemorrhage body are denoted as width and height, respectively. The concept is shown in figure 5.5 (a)-(b).

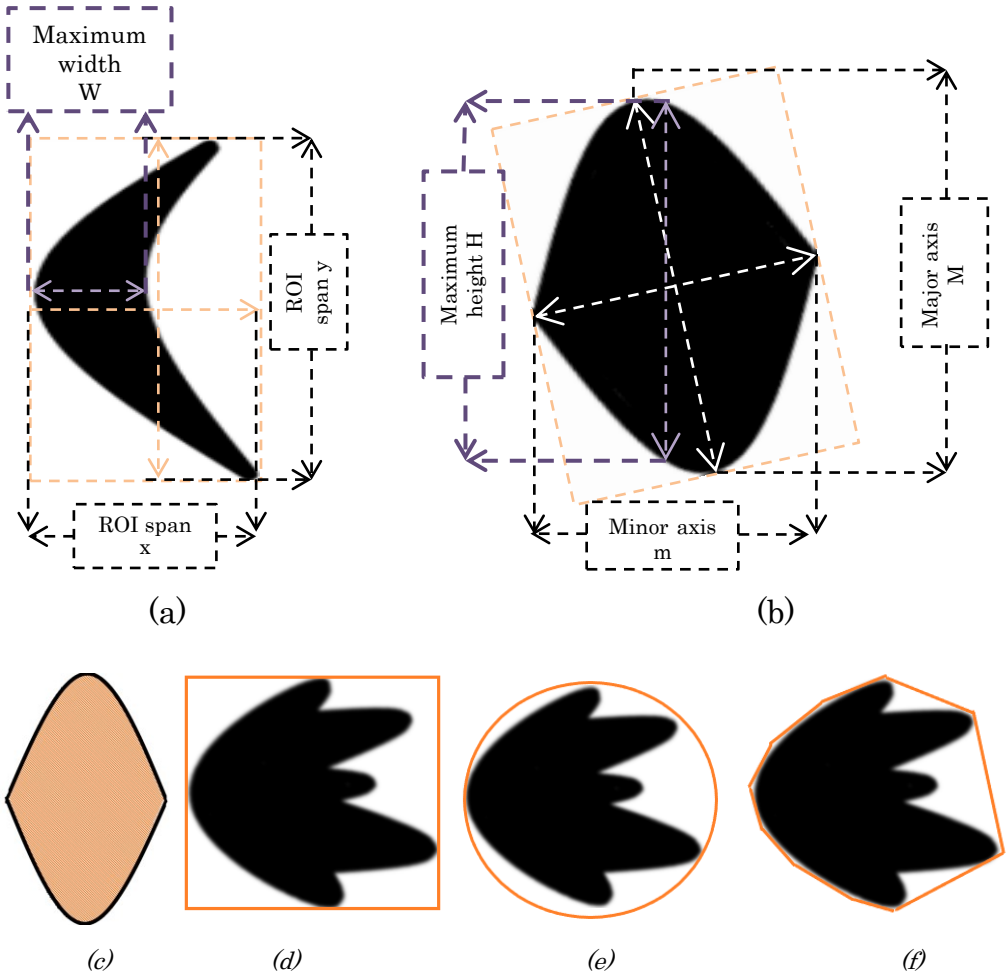

Figure 5.5: Different hemorrhage shape features (a)-(b) Hemorrhage and ROI spans (c) Hemorrhage area (d) Best fit rectangle (e) Best fit circle (f) Convex hull

Skull vicinity (V) is a measure of distance between the boundary elements of hemorrhage and the corresponding segmented brain image. Hemorrhage boundary candidates within five pixel distance from the brain boundary, are recorded as positive candidates [72]. Mathematical calculation is formulated as follows,

$$V \quad [\sum \Delta d\,\{(1,0): |B_i - H_i| \leq 5, 0\} / \sum H_i] * 100$$

where, B_i and H_i represent i^{th} element of brain and the hemorrhage boundary candidate. For less than and equal to five pixels distance Δd picks up value 1, for rest of the cases it remains as 0. Summation of all positive occurrences presents how tightly or loosely the hemorrhage is connected to the skull. The concept is described in figure 5.6.

In a dataset, hemorrhage can be detected in one or more images. Each of the hemorrhage affected image is processed to extract different shape features,

IPF, compactness and skull vicinity values. From the extracted primary features, higher order correlative features are derived.

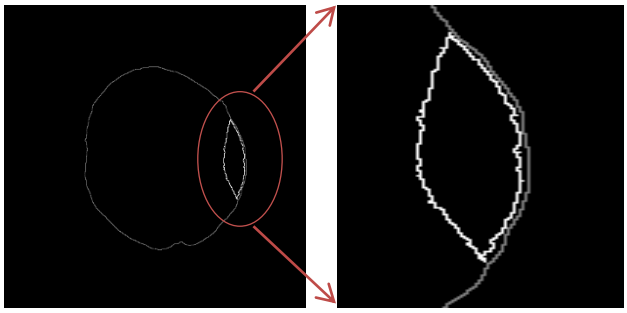

Figure 5.6: Skull vicinity

5.3.3. Derived shape features

Correlative features which are calculated from above discussed primary features can be addressed as derived shape features. These derived features are more useful for classification. Primary features are static information which can be same for different shapes. When a derived feature is calculated from primary features, the relative impact of a particular shape is evaluated. This relation varies for varying shape, by enhancing difference between categories. Some potential derived shape features are discussed below.

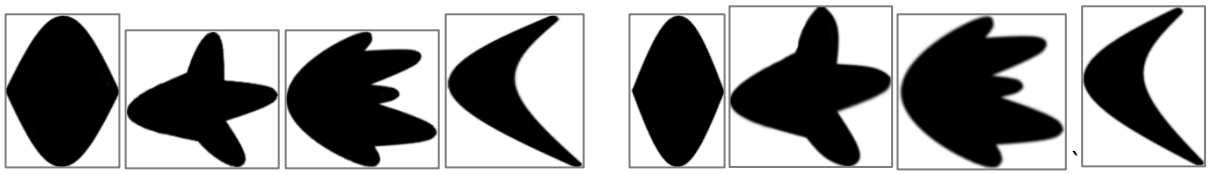

(a) (b)

Figure 5.7: (a) Different hemorrhage area with same ROI size, (b) Same hemorrhage area with different ROI size

Image identifier	*Image type*	*Hemorrhage area A*	*ROI size R*	*IPF of ROI*
Figure 5.7(a)	*Same ROI size*	30539	**49715**	0.6143
		19536	**49776**	0.3925
		26339	**49646**	0.5305
		15345	**49830**	0.3079
Figure 5.7(b)	*Same hemorrhage size*	**24862**	42606	0.5835
		24890	63754	0.3904
		24825	53040	0.4680
		24825	84328	0.2944

Table 5.3: IPF of ROI calculation for figure 5.7 images

1. Local Information packing factor (local_IPF):

It is the ratio of the area of the hemorrhage to the area of the best fit rectangle. Mathematically it can be expressed as

$$local\_IPF = A/R.$$

The fact is described with the help of eight vector diagrams shown in figure 5.7. In figure 5.7(a), four hemorrhage patches of different shape and size are shown. Area of bounding rectangle of these hemorrhage are almost the same; but the ratio between hemorrhage area and best fit rectangle area are significantly different from each other depending on the size of the hemorrhage. Where the hemorrhage size is high, local_IPF is also high, as the area of best fit rectangle is constant in all the cases. In figure 5.7(b) all the hemorrhage patches have almost the same area; but area of the best fit rectangle differs from each other. Thus with lower area of rectangle, the IPF increases as hemorrhage area is fixed in this case. Hence, local_IPF contributes significantly in classification even when either the hemorrhage area or ROI area of different hemorrhage patches are almost equal. The tabulation and comparison for shown vector diagrams, are presented in table 5.3 and figure 5.8 (a) and (b).

The results are demonstrating the potential of derived shape features. When the primary feature value, here the area of a hemorrhage, cannot specify the class, then the ratio of hemorrhage area to the best fit rectangle, mimics the shape information of the target object.

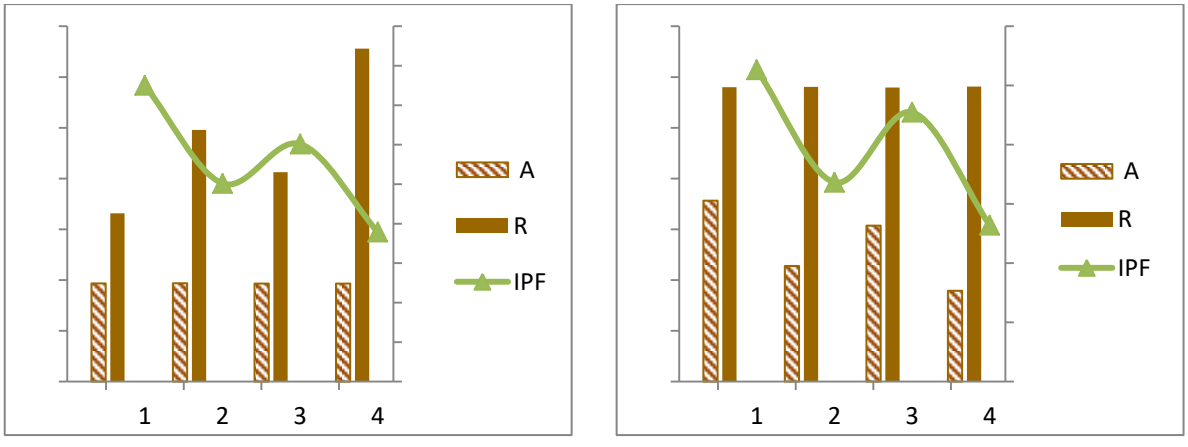

(a) *(b)*

Figure 5.8: IPF varies with (a) constant ROI area (b) constant hemorrhage area

2. Span ratio (Sr):

It is the ratio of the maximum available spans of hemorrhage along x-axis and y-axis and is used to understand the nature of the spread. If the x-axis span i.e. width is W and y-axis span i.e. height is H then span ratio is calculated as follows –

$$S \begin{cases} = W/H; & \text{when } W < H \\ = H/W; & \text{when } H < W \end{cases}$$

Where,

W= maximum x-coordinate value available in hemorrhage – minimum x-coordinate value available in hemorrhage

H= maximum y-coordinate value available in hemorrhage – minimum y-coordinate value available in hemorrhage

The ratio varies with the change in shape. EDH, because of its convex-convex shape, has high y-axis span and low x-axis span. SDH mimics this pattern with larger x-axis span. In SAH sometimes x-axis becomes larger than y-axis.

3. Area to perimeter ratio (Ap):

It is the ratio between hemorrhage area A and perimeter of hemorrhage P. For same area if the shape of hemorrhage is circular the ratio value will be maximum. Ap decreases with increase in non-circularity in shape. EDH offers maximum Ap due to its elliptical nature.

$Ap = A/P$, when A is the hemorrhage area and P is its perimeter.

4. Circular area ratio (Cr):

It is the ratio between hemorrhage area and best fit circle area. With the change in span the radius of circle varies. So for the same area with higher span, needs a circle having larger radius reducing the circular ratio value.

$Cr = A/C = A/(\pi * r^2)$, when r is the radius of the best fit circle C.

For constant A, $Cr \propto 1/r$ i.e. with increase in radius the ratio decreases.

5. Elliptical area ratio (Er):

It is the ratio between the hemorrhage area and the best fit ellipse area. A convex shape is better fitted inside an ellipse increasing the value of Er. Generally EDH offers higher Er than other hemorrhage patches.

6. Diameter ratio (∂):

It is the ratio of diameters of equivalent circle to best fit the circle. This is the circularity measurement of an image. When a shape changes from polygonal to circular its diameter ratio increases gradually.

If the diameter of equivalent circle is d_1 and diameter of best fit circle is d_2 then ∂ can be calculated as

$$\partial = {}^{d_1}/_{d_2}$$

It can be rewritten as,

$$\partial = {}^{d_1}/_{d_2} = {}^{r_1}/_{r_2} = \sqrt{r_1^2/r_2^2} = \sqrt{\pi r_1^2/\pi r_2^2} = \sqrt{A/C} = \sqrt{C_r}$$

Hence, $\partial \propto C_r$

So, in practice this feature is redundant with circular area ratio and hence need not to be considered if the previous one is already considered in input.

7. Maximum distribution ratios ($\mathcal{L}x$, $\mathcal{L}y$):

It is the ratio between maximum available hemorrhage span and ROI span in corresponding axis. If the maximum available spans of hemorrhage are W and H, and the same of ROI are x and y respectively, then the maximum distribution ratio across x axis is

$\mathcal{L}x$ = W/x

Similarly for y-axis, it is $\mathcal{L}y$ = H/y.

5.4. Feature optimization and classification

Segmented hemorrhages are processed to extract features for classification. Other than patients' dataset, 50 EDH, 50 SDH, 31 SAH and 31 intra-axial hemorrhage data are used for training and testing purpose. The respective brain ROI images of each hemorrhage, generated during brain segmentation (described in chapter 3), are considered to find the boundary of the brain. Total information size i.e. hemorrhage area, compactness and perimeter of segmented hemorrhage, span across x and y axis, equivalent circle, best fit circle, best fit rectangle and best fit ellipse are found from each hemorrhage. The vicinity

of the hemorrhage to the skull, which is important information for classification, is also calculated.

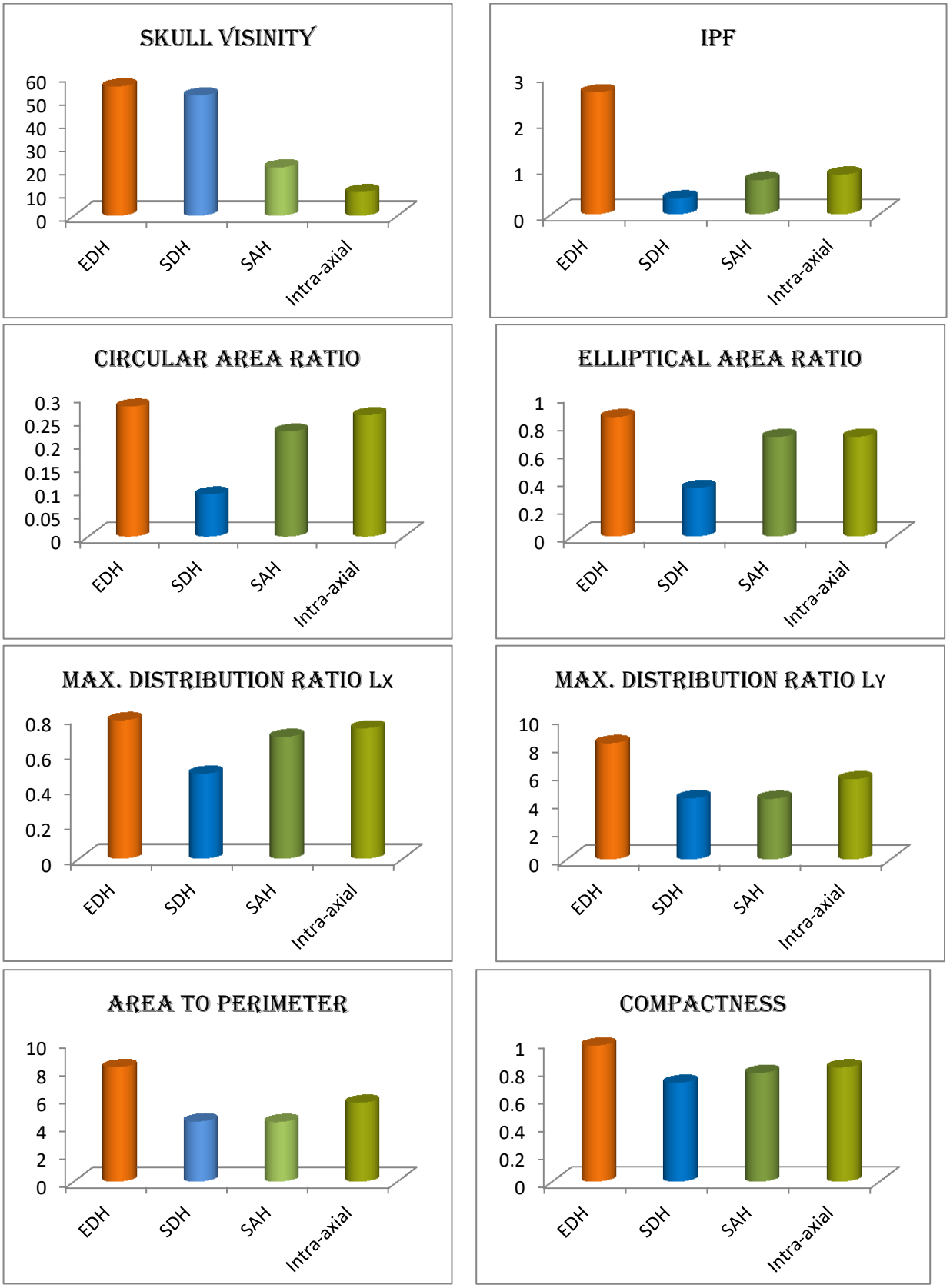

Figure 5.9: Features are compared for different types of hemorrhage

From primary shape features, derived features are extracted mathematically. These derived feature values are more relevant to the hemorrhage shape and hence perform better as classification input parameter. Value of skull vicinity, local_IPF, circular area ratio, elliptical area ratio, maximum distribution ratios $\mathcal{L}x$ & $\mathcal{L}y$, area to perimeter ratio and compactness features are plotted in the graph shown in figure 5.9. SAH is not included here in 'other' group, in order to inspect its potential in creating noise in classification. Results show that for $\mathcal{L}y$, area to perimeter and compactness, SDH and SAH is not much distinguishable.

Initial dimension reduction by new feature extraction is done by projecting primary features into the low dimension secondary feature plane. In this work, without considering the derived feature set merely, combined set is used to achieve the best performance of the classifier. Form the entire list of primary and derived features, dimension reduction is done by finding the most prospective features for classification. The potential of a feature in classification method depends on its separability power between the classes. Separability is measured by comparing the the spread of a feature around local mean i.e. within class mean and global mean.

Within the class, spread is determined by computing local variance -

$$\sigma_l^2 = \sum_i \frac{\sum_n (x_n - \mu_i)^2}{n}$$

Here, μ_i presents the mean of a feature set x of i^{th} class and n is the number of candidate images of the class. Similarly, the across class spread is found by computing global variance -

$$\sigma_o^2 = \sum_i \frac{\sum_n (x_n - \mu_o)^2}{n}$$

where, μ_0 presents the overall mean. The separability S is calculated as -

$$S = \frac{\sigma_o^2}{\sigma_l^2}$$

To gain a better insight of classification potential, the separability measure of different features are reported in Table 5.4 and graphically depicted in Figure 5.10. The potential is examined into two steps. In the first step, features having great potential to separate the target classes from other are examined. In second

step, features with higher potential to classify the target class objects into their corresponding classes are selected.

Primary features	Separability		Derived Features	Separability	
	Target versus Other	EDH versus SDH		Target versus Other	EDH versus SDH
perimeter	1.10	2.01	*skull vicinity V*	**3.19**	0.99
Area	1.07	1.00	*span ratio Sr*	**1.28**	1.03
W	1.01	1.04	*local_IPF*	1.01	**6.09**
H	**1.46**	1.03	*circular area ratio Cr*	**1.45**	1.39
best fit circle	1.15	1.06	*elliptical area ratio Er*	1.06	**4.79**
best fit ellipse	1.08	1.05	*maximum distribution ratio £x*	1.03	**4.61**
best fit rectangle	1.08	1.05	*maximum distribution ratio £y*	1.02	2.07
radius of equivalent circle	1.12	1.02	*area to perimeter ratio Ap*	1.04	1.22
compactness	1.03	**3.40**			

Table 5.4: Separability of different features

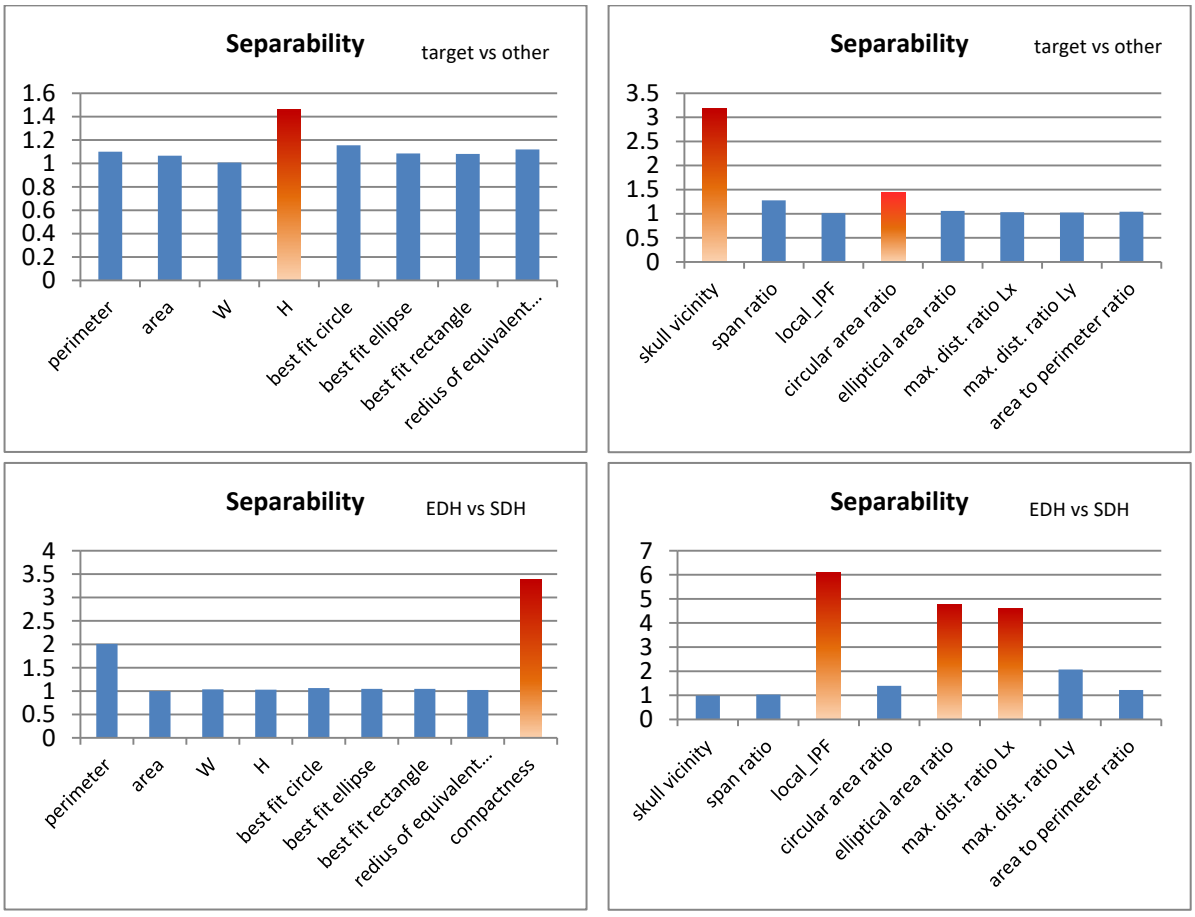

Figure 5.10: Separability

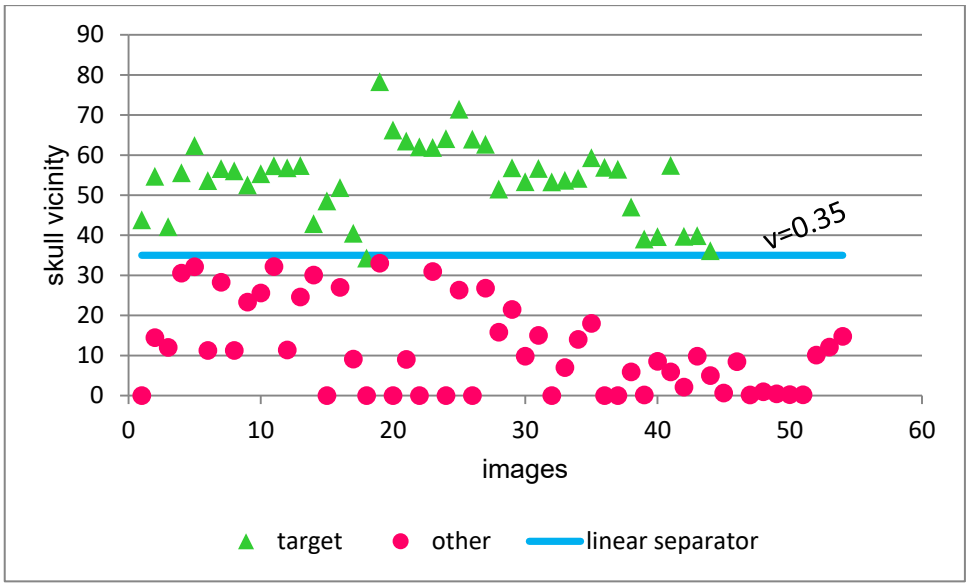

Figure 5.11: Skull vicinity distribution

Height from the primary feature set and the skull vicinity from derived feature set, standout with the highest potential to discriminate target class from others. Circular area ratio also demonstrates good potential for first step classification. In practical test, skull vicinity demonstrates the utmost strength and nullifies the requirement of any other features' association. The potential of skull vicinity is depicted graphically in figure 5.11. If minimum 35% of the perimeter returns positive value i.e. remains within five pixels distance from the brain boundary then the hemorrhage is considered as skull adhered. A 2D linear classifier is designed to separate target class from the entire dataset. The equation below imposes the predictor line in the input space,

$$V \quad 0.35 = 0$$

Value 1 is assigned to rank 'r' for any positive data and 0 for rest.

$$r \leftarrow V \quad 0.35$$

To evaluate a dataset of multislice CT scan, % value of V of all hemorrhage affected images are considered to set rank for respective dataset. The measure of average skull vicinity and assigned rank value of entire database, is collated in table 5.5. For V more than or equal to 50%, the rank is considered as 1. The result presents 100% accuracy in classification.

Serial no.	Ground truth	%V	Rank 'r'	Classification status
1	EDH	61.43	1	Satisfied
2	EDH	58.10	1	Satisfied
3	IPH	9.72	0	Satisfied
4	EDH	65.57	1	Satisfied
5	SDH	77.53	1	Satisfied
6	ICH	0.00	0	Satisfied
7	SDH	83.85	1	Satisfied
8	SAH	1.86	0	Satisfied
9	SDH	74.84	1	Satisfied
10	ICH	8.07	0	Satisfied
11	IPH	9.73	0	Satisfied
12	EDH	51.60	1	Satisfied
13	IPH	8.72	0	Satisfied
14	SDH	58.03	1	Satisfied
15	SDH	50.00	1	Satisfied
16	SAH	0.00	0	Satisfied
17	EDH	64.97	1	Satisfied
18	EDH	52.57	1	Satisfied
19	IVH	0.00	0	Satisfied
20	SDH	76.53	1	Satisfied
21	ICH	5.74	0	Satisfied
22	IVH	0.00	0	Satisfied
23	SDH	70.09	1	Satisfied
24	SAH	4.70	0	Satisfied
25	EDH	51.44	1	Satisfied
26	IPH	6.56	0	Satisfied
27	SDH	68.37	1	Satisfied

Table 5.5: Skull vicinity value of different dataset

Target class is further divided into two classes – EDH and SDH. Both EDH and SDH hemorrhage are very close to skull than any other classes. Compactness from primary feature set, local_IPF, elliptical ratio and maximum distance ratio $\mathcal{L}x$ from derived feature set, have projected good potential for EDH and SDH classification. Their potential is presented for visual interpretation in figure 5.12. Artificial neural network tool of Matlab is used to classify EDH and SDH. Input feature array is created using above mentioned potential features to train and validate the network.

For training of the artificial neural network, features are extracted from 50 EDH and 50 SDH hemorrhage images which are not part of the dataset under test. 70% data from the data (33 EDH, 37 SDH) are used for training, 15% (9 EDH, 6 SDH) are for validation and rest are used for testing of classifier. Best

performance achieved by training and testing is reported as confusion matrix in figure 5.13. It has achieved 100% accuracy in its performance. This trained classifier is then used to classify patients' dataset. For each dataset, there are multiple images having hemorrhage. The classifier predicts class for each image. The class having highest strength in a dataset is selected as the class of hemorrhage of that dataset. Using this method, entire database is classified with 100% accuracy by this classifier.

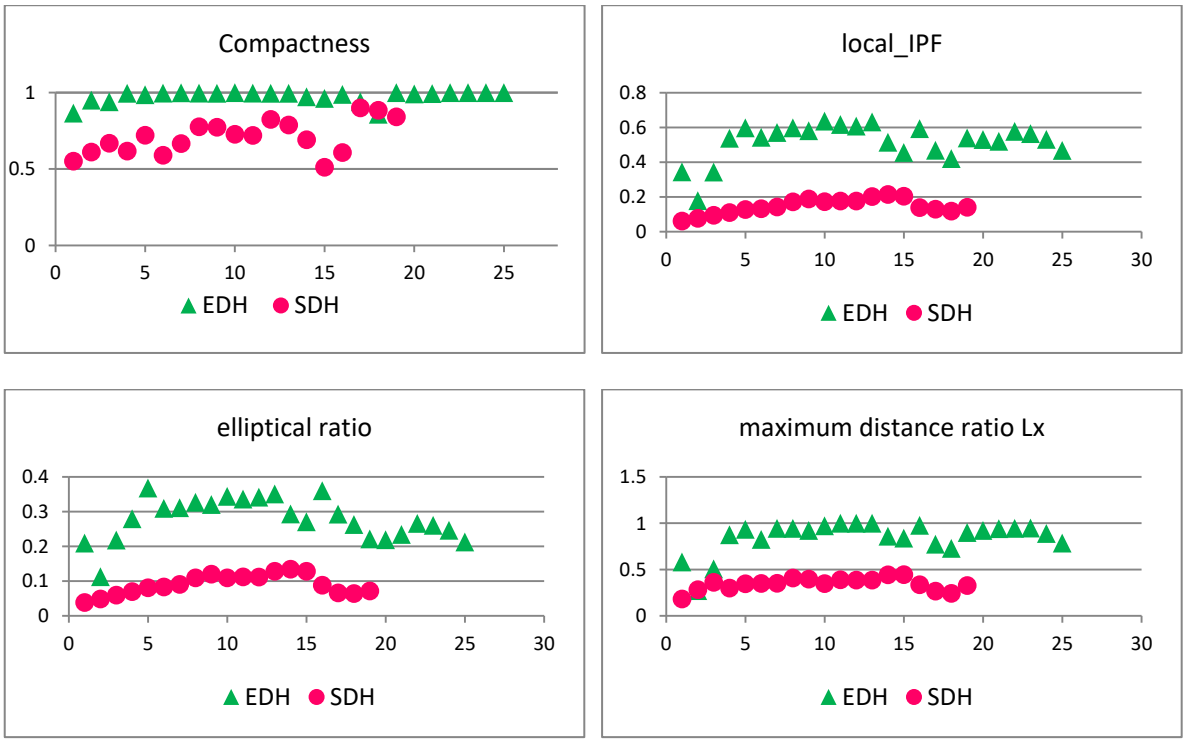

Figure 5.12: Distribution of potential features for EDH and SDH

5.5. Conclusion

Proposed classifier has segmented target group of hemorrhage successfully from database and sub-divided it into EDH and SDH accurately. Tree classifier is used to perform classification in two steps. It separates the non-target classes before final classification. A simple linear classifier performs the separation job with higher accuracy. Then the target group is classified into its respective classes. The initial elimination process increases classification accuracy significantly.

An attempt was taken to classify the entire database directly into three classes in a single go. Skull vicinity, compactness, local_IPF, elliptical ratio and maximum distance ratio Lx were taken as classifier input features. A reduction in

the accuracy of classifier was experienced. The best possible performance, we were able to achieve is shown in figure 5.14. Though the classifier was trained with 0% error, accuracy of the classifier dropped to 95.8% during test. Skull vicinity which is a useful feature for classification of the target and non-target class has very low power in separating EDH from SDH as shown in figure 5.10. Similarly local_IPF, elliptical ratio and $\mathcal{L}\chi$ are not potential features for classification of target class and non-target class. These input features are thus introducing noise in the classifier performance affecting the accuracy of classification result.

The success of the proposed method will be a great support for medical system if implemented in practice. High accuracy and specificity are obtained in classification of EDH and SDH. With no false negative, the risk of delay in brain hemorrhage treatment due to machines' misguidance in automatic detection, is lowered to zero. This is one of the most important requirements in disease diagnosis and is a critical parameter for any CAD system.

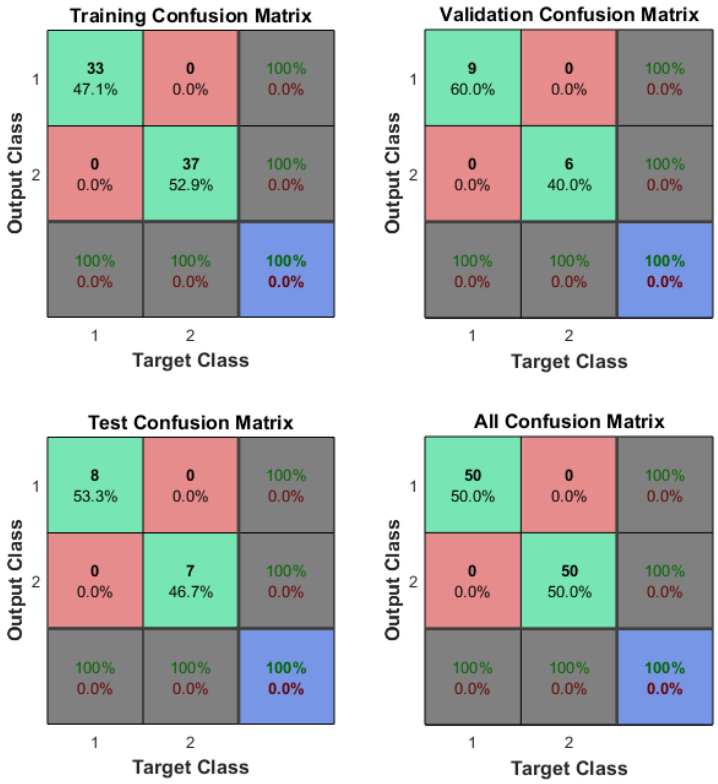

Figure 5.13: Confusion matrix of EDH-SDH classifier

Figure 5.14: Confusion matrix of three class classifier

Chapter 6

Conclusion

Overview

Proposed methods for hemorrhage segmentation and EDH, SDH classification are summarized in this chapter. The insights of different steps have been analyzed to understand the contribution of this work to the research world. Proposed binary features have shown significant impact in accuracy enhancement in different steps of the entire research. Method of arranging CT images in anatomical order is a useful technique for other brain researches too. Prospects and deficiencies of the entire work are discussed to propose further research for advanced version of the designed CAD with more facilities. A modification to make system more compatible with clinical process is proposed by using DICOM images directly as the input of the system.

6.1. Introduction

In this thesis - an automatic, fast and easy to implement methodology is proposed. This method has successfully segmented hemorrhage from CT images and has done classification of segmented hemorrhage in three classes – epidural hemorrhage, subdural hemorrhage and others. Both segmentation and classification have shown sufficient accuracy and sensitivity. This method was an attempt to support medical practitioners in their decision making process. The implementation of this automatic detection can save lives by accelerating diagnosis during emergency.

Commercialization of proposed CAD will lower subjectivity in treatment with no tiredness. Use of this system in hospitals having CT machines but no field expert or radiologist will offer a quick initial diagnosis to initiate treatment. Different hospitals, using the same CAD, will have homogeneous exchangeable reports.

6.2. Research potential

The entire research is divided into three major parts, and one additional part is added to introduce some binary features. This additional part is presented in chapter 2. Rest of the works was discussed sequentially in the consecutive chapters based on the process flow of the proposed CAD. Performance analysis at each step was done before moving to the next stage of the research.

6.2.1. Proposed features

Three easy to compute features are proposed in chapter 2. These features are used in different stages of the research work to improve the performance of the proposed CAD. At preprocessing stage, data cleaning is done with the help of porousness and IPF information. Skull images, without any brain information within it, are identified by null or negligible pore count of respective images. These images need no attention in our process. The images, without skull, are also not of our concern for hemorrhage segmentation. Such no-skull images are identified by the IPF value. Elimination of these unwanted images, reduces the computational

cost as well as increases the performance accuracy of the proposed CAD - as demonstrated in chapter 3. Pore Information also helps to find the master image which works as the center image for bi-directionally propagated brain segmentation process. IPF value identifies the seed image in the dataset to initiate re-organization of CT images in anatomical order.

In the classification of hemorrhage, IPF and compactness have a significant contribution. Both of these features return good separability value for classification of EDH and SDH. The overall classification accuracy drops to 98% if any of the two features, local_IPF and compactness, is removed. The confusion matrices of best performing neural networks, selected from 20 tests, are shown in figure 6.1.

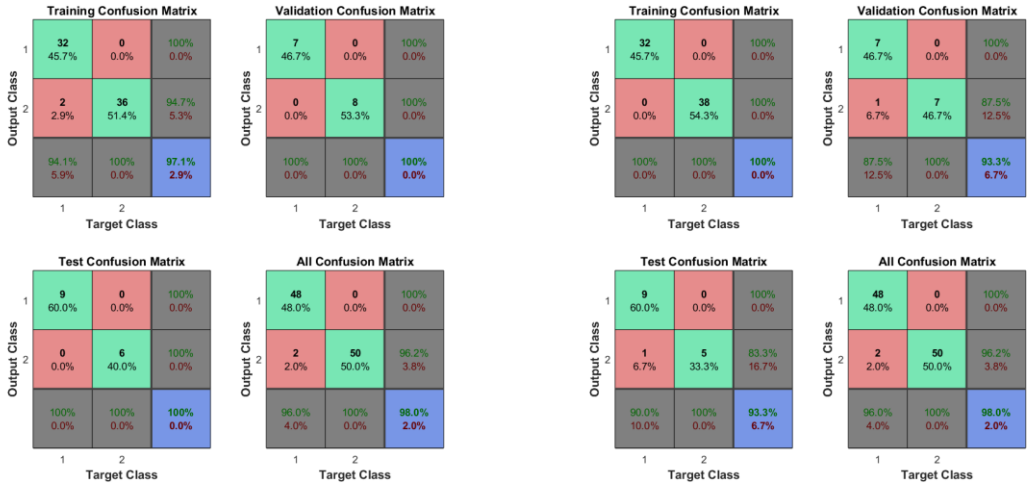

Figure 6.1: Classifier performance (a) Without local_IPF feature, (b) Without compactness feature

6.2.2. Image pre-processing

Pre-processing of dataset before actual analysis of images is done to reduce noise. For hemorrhage segmentation, brain intracranial part is the ROI. The key achievements of this chapter are, arranging dataset in anatomical sequence, automatic seed point finding for mask definition, implementation of outer masks to increase segmentation accuracy in nasal area images, successive propagation of inner mask. This anatomical arrangement keeps the images of a dataset in the expected order. It is a useful technique for all kinds of brain CT inspection. The

concept of using double mask to restrict the segmentation search area, is introduced for the first time in brain CT image segmentation, as per our knowledge. The effectiveness is discussed in the result section of chapter 3. The successive propagation of inner mask had effectively included the brain areas, which are not included in the initial mask definition. It breaks the barrier of hard definition of a mask and makes it dynamic and adaptive.

6.2.3. Hemorrhage segmentation

In chapter 4, hemorrhage segmentation is done using simple histogram thresholding technique to keep the CAD simple and fast. The threshold is defined by newly introduced 'upset point'. Clinical knowledge of the pattern of information intensity distribution and its alteration due to inclusion of hemorrhage is taken as domain knowledge to design this system. The speed and accuracy of proposed method has outperformed other established methods. This 'upset point' can be further explored for possible implementation in identification of other brain diseases. The concept of adding all thresholded images to find final location of hemorrhage returns good result. Other advantages of this method are the simplicity, ease and speed.

6.2.4. Classification

For classification, selection of optimum feature set is important to get rid of curse of dimensionality. Projecting the available set of features to a lower dimension feature plane is a common and effective technique used for dimension reduction. In this thesis, initially the primary features are projected to a low dimension secondary plane. Then, before final selection, all the features are combined. Filtering is done depending on the separability potential of the feature of that combined set. This process empowers us not to miss any potential feature irrespective of its type. Compactness, from primary feature set, is thus selected for

classification of EDH and SDH. The impact of this feature in classification is already discussed in the section 6.2.1.

6.3. Limitations

This work cannot detect multiple hemorrhages in a dataset. In case of Simultaneous Multiple Intracerebral Hemorrhages (SMICH), only the largest hemorrhage can be identified by this method. Though it is sufficient to trigger medical attention and the requirement of expert's opinion, the report compiles incomplete information in diagnosis perspective. Proposed classifier also suffers from limited class classification issue. Hemorrhages other than EDH and SDH are grouped as 'other', not classified.

In absence of sufficient volume of versatile data, it is difficult to overcome these above mentioned shortage. A standard benchmark database of brain CT hemorrhage needs to be created for better research in this field.

6.4. Future works

Further research can be done to propose modified algorithms which will identify all hemorrhages in an image. Other than selecting largest patch, an adaptive algorithm can be proposed to find all potential hemorrhage candidates in the segmented image. Research can be conducted to add more functions in the classifier, so that it can classify all the hemorrhages in their respective classes.

To improve compatibility of the proposed method with medical support system, it can be modified to consider DICOM images as input to avoid image compression in pre-processing. From DICOM information file, HU scale and rescale factor can be accessed and used for intensity computation [158]. The hemorrhage patch size can be calculated using pixel spacing information to understand the severity of the disease.

Use of powerful CAD will improve patient support and service by reducing death, rate of disability and other associated hazards. Cost is the most important factor which needs to be scaled to reach larger segment of population. The proposed CAD is designed using LabVIEW and Matlab, both of which are costly

platform. A low cost system can be designed by transforming the codes in low cost or free coding platform like Python.

6.5. Closing note

Brain image segmentation result presented in chapter 3 is useful for all kinds of brain artifacts detection, if restoration is implemented at end. Because of overlapping intensity range with skull, calcification information if any and some high intensity scattered pixels within brain are removed during thresholding of skull. Such areas introduce small holes in the extracted BM. For accurate lossless segmentation, such holes can be filled by actual intensity information. To avoid any nasal cavity inclusion, only holes have an area less than 0.1% of segmented image should be considered. These segmented images can be used for any brain disease diagnosis or further image analysis - as this restoration offers a lossless segmentation of brain images.

Publication

Journal

"Intensity population based unsupervised hemorrhage segmentation from brain CT images" in Expert Systems with Applications, Volume 97, 1 May 2018, Pages 325–335

ELSEVIER

https://doi.org/10.1016/j.eswa.2017.12.032

Conference

1. "Derived Shape Features for Brain Hemorrhage Classification", 8th International Conference Soft Computing for Problem Solving (SocProS 2018)
   [Conference Proceedings will be published online in the SCOPUS indexed AISC series of Springer]

2. "Identification of Abnormal Brain Images from CT Image Dataset", 2nd International Conference on Advanced Computational and Communication Paradigms (ICACCP 2019). Awarded as best paper in computer vision and machine learning track.
   [Conference Proceedings will be published online in IEEE Proceedings, SCOPUS indexed]

Pre-print [Archive]:

Binary Image Features Proposed to Empower Computer Vision
https://arxiv.org/abs/1808.08275

An Automatic Method for Complete Brain Matter Segmentation from Multislice CT scan
https://arxiv.org/abs/1809.06215

Appendix A

[definition, formula, range]

To understand practical ranges, the definitions and details formulae to evaluate IPF, C, S, P are discussed.

1. Information Packing Factor [IPF]

Fraction of area of an image that is occupied by information which are useful for further analysis to extract data is proposed as Information Packing Factor [IPF] of the image.

Consider an image I of size A which has u number of useful information and z number of non-useful or background information. IPF for that image can be calculated as

$$IPF = u/A = u/(u+z) = 1/(1+z/u)$$

Now the values of IPF vary depending on u and z.

$$IPF \begin{cases} = 1 & If\ z = 0\ and\ u > 0;\ no\ background\ pixel\ in\ the\ image \\ < 1 & If\ z > 0\ and\ u > 0 \\ = 0 & If\ u = 0 \end{cases}$$

So, the range of possible values of IPF can be written as $0 \leq IPF \leq 1$

In practice, u=0 is not possible. So, practically the range can be written as $0 < IPF \leq 1$

2. Compactness [C]

Fraction of usable information spread area of an image that is actually occupied by foreground pixels is described as compactness [C] of the image.

Compactness offers the idea that how closely the usable information is packed in the image. The measurement is local as only the spread area is counted not the area of whole image.

Say, in the above mentioned image I, there are total y number of background pixels available within the usable information spread. Then

$$C = u/(u+y) = 1/(1+y/u)$$

Now the values of C vary depending on u and y.

$$C \begin{cases} = 1 & If\ y = 0\ and\ u > 0;\ no\ space\ between\ foreground\ pixels \\ < 1 & If\ y > 0\ and\ u > 0 \\ = 0 & If\ u = 0 \end{cases}$$

So, the range of possible values of C can be written as $0 \leq C \leq 1$

In practice, $u=0$ is not possible. So, practically the range can be written as $0 < C \leq 1$

3. Scatterness [S]

Fraction of usable information spread area of an image that is occupied by non-usable of background pixels is described as scatterness [S] of the image.

Scatterness offers the idea that how loosely the usable information is placed in the image. This measurement is also local as only the spread area is counted not the area of whole image.

So, compactness and scatterness are complement of each other. And the sum of both must be unity. We can calculate S if C is known by the following equation:

$$S = 1 - C = y/(u + y) = 1/(1 + u/y)$$

Now the values of S vary depending on u and y.

$$S \begin{cases} = 1 & If\ y > 0\ and\ u = 0 \\ < 1 & If\ y > 0\ and\ u > 0 \\ = 0 & If\ y = 0; \quad no\ space\ between\ foreground\ pixels. \end{cases}$$

So, the range of possible values of S can be written as $0 \leq S \leq 1$

In practice, as $u=0$ is not possible practically the range can be written as $0 \leq S < 1$

The maximum value of y can be the value of z. So the range of y can be defined as $0 \leq y \leq z$.

4. Porousness [P]

Fraction of usable information spread area of an image that is occupied by non-usable information which has no link to background pixels as neighbor is described as porousness [P] of the image.

Each such individual area creates a 'pore' in the image.

Say, in image I, total area occupied by pores is w. Then

$$P = w/(u + w) = 1/(1 + u/w)$$

Now the values of P vary depending on u and w.

$$P \begin{cases} = 1 & If\ u = 0\ and\ w > 0 \\ < 1 & If\ w > 0\ and\ u > 0 \\ = 0 & If\ w = 0; \quad no\ pore\ in\ the\ image. \end{cases}$$

So, the range of possible values of P can be written as $0 \leq P \leq 1$

In practice, as $u=0$ is not possible practically the range can be written as $0 \leq P < 1$.

The maximum value of w can be y and maximum value of y can be z. So the range for w can be written as $0 \leq w \leq y \leq z$.

There can be one or multiple pores in an image. Now if the no of pores in image i is n_p and the area of the pores are $p_1, p_2, \ldots p_n$, then porousness contributed by any pore p_i is

$$Pi \quad p_i/u + \sum p_i \quad where\ i \quad 1\ to\ n$$

$$p_i/u + w$$

And so, $P \quad \sum p_i$. Thus the range of P_i is same as P.

Appendix B

[algorithm]

Algorithms are described in details to generate code of IPF, C, S, P.

The image contains foreground part (F), background (B), porousness parts (D) and scattered gaps (G). This can be presented by Venn diagram as shown in figure B.1.

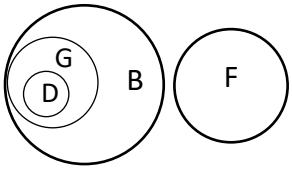

Figure B.1: conceptual presentation of image pixel intensity distribution

Information and background are disjoint sets, whereas porousness is a subset of scattered gap and gap is a subset of background.

Logically it can be presented as

$B \cap F = \emptyset$ $B \cap G = G$

$G \cap D = D$ $D \subset G \; and \; G \supset D$

$G \subset B \; and \; B \supset G$ $D \subset B \; and \; B \supset D$

The algorithms for extraction of the proposed features are described below. Let say, the image is I. The size of image is nXm, when image array has 'n' number of rows and 'm' number of columns.

Total span of intensity in the image is i_0 to i_x.

Foreground intensity range is i_k to i_l.

The binary image $I_b = \begin{cases} 1 \;\; for \;\; i_k \leq i \leq \; i_l \\ 0 \; for \; any \; other \; i \end{cases}$

1. IPF measurement

Mathematically IPF is evaluated using the formula as follows,

$$IPF = \sum I_b / (nXm) = \sum I_b / A$$

where A=nXm=total area of the image

To compute it automatically the code should be created following the algorithm given here.

```
Ib <-- image

th = threshold
u=0
for i=0 to (n-1)
    for j= 0 to (m-1)
        if Ib[i,j] ≥ th
            Ib[i,j] = 1
        else
            Ib[i,j] = 0
u=∑Ib
IPF=u/(n*m)
```

2. Compactness measure

For compactness, total foreground pixel and all the gaps between foreground pixels need to be counted. The algorithm used is given below. Scatterness can be calculated easily by taking complement of compactness.

```
ib ← image
sp=0            //**total span of foreground
f=0             //**foreground count
for i=0 to (n-1)
    k1=-1
    k2=-1
    n=0
    for j= 0 to (m-1)
        if ib[i,j]=1
            If n=0
                k1=j
                n= 1
            f=f+1
    for j= (m-1) to 0
        if ib[i,j]=1
            k2=j
            break
    if k1 > -1
        sp= sp+k2-k1+1
C= f/sp                         **//compactness
S=1-C                           **//scatterness
b=sp-f          **//background within foreground : secondary information
```

Scatterness (S) is calculated directly as $S = \bar{C} = (1 - C)$

It also cab ne calculated directly using formula $S = {}^{b}/_{S_p}$

3. Porousness measurement

To count porousness (P), all gap pixels having any link to background pixel as neighbour should be removed from s_p.

A border frame is appended to the image before operation. In case of no background around the foreground of the image which is under test, this added background will act as image background. The border frame is nothing but two extra rows and columns which are added at both ends of rows and columns of the image respectively as shown in figure B.2. Elements of these rows and column must be equal to background intensity value. Here it is considered as 0. To locate pixels contributing in porousness, non-porous pixels from scatter pixel cloud will be removed.

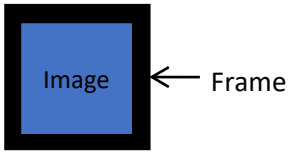

FigureB.2: image with append frame

```
//**porousness should not have overlapping boundary with foreground
//**to confirm it, an extra layer is padded at each of the four sides of the image
//**this is required for images having no background surrounding foreground

Ib <-- image
I <-- Null image of {(n+2)*(m+2)}
for i=0 to n
    for j= 0 to m
        I[i+1,j+1]=Ib[i,j]
//**replace background outside foreground by 2
//** step 1: (0,0) position pixel is considered as seed for flood
I[0,0]=2
//** step 2: flood fill search
repeat for k>0
    k=0
    for i=0 to n
        for j= 0 to m
```

```
                    if I[i,j]=2
                        for p=i-1 to i+1
                            for q= j-1 to j+1
                                if I[p,q]=0
                                    I[p,q]=2
                                    k=k+1
//** convert to negative binary image
for i=0 to n
    for j= 0 to m
            if I[i,j]>0
                I[i,j]=0
            if I[i,j]=0
                I[i,j]=1
```

$P_{area} = \sum I$

$P = P_{area}/(u+P_{area})$

Appendix C

[Ellaboration and illustration]

Discussion on some necessary information

1. Chapter 3: Seed point

Local seed points and query end points of four sub-images are listed in table C.1. The search directions of query starting from seed point to end point is illustrated below pictorially in figure C.1.

Sub-image	Size	Seed point	Query end point
I_{m11}	n_1Xm_1	n_1-1,m_1-1	0,0
I_{m12}	n_2Xm_2	n_1-1,m_1	0,m
I_{m21}	n_3Xm_3	n_1,m_1-1	n,0
I_{m22}	n_4Xm_4	n_1,m_1	n,m

Table C.1: seed point of sub-images

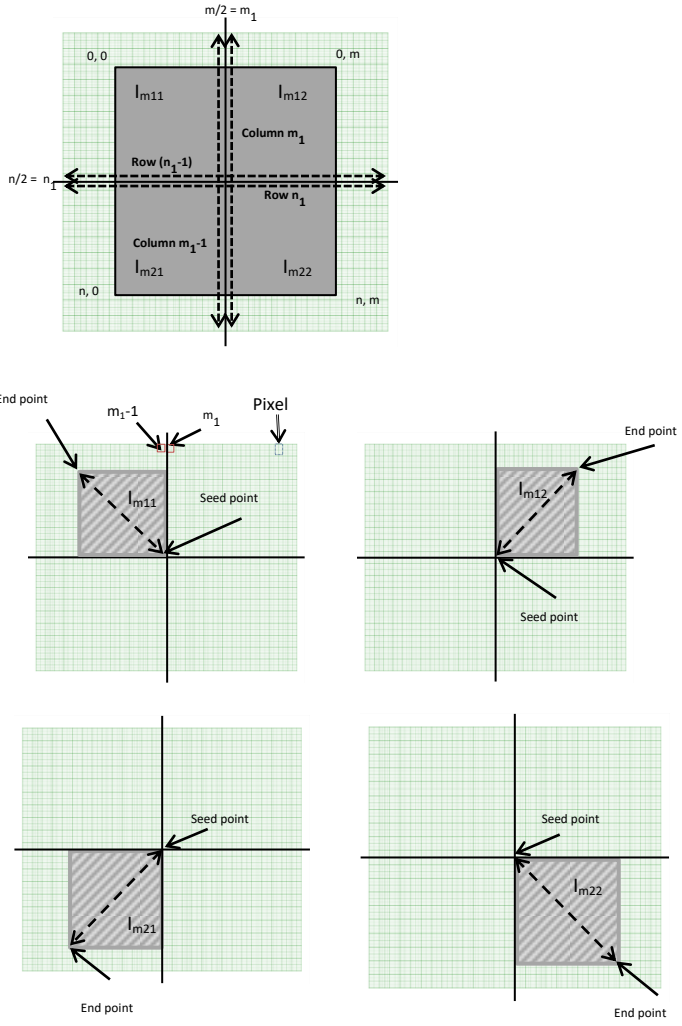

Figure C.1: Sub-images with seed point and extreme point

2. Chapter 4: Dice Coefficient

Dice coefficient is the measure of accuracy in segmentation result by comparing segmented area with the ground truth. It is the measure of overlap index.

$$\text{Dice coefficient DC} = \frac{2(I_g \cap I_s)}{|I_g| + |I_s|} \times 100$$

Where, I_g and I_s are ground truth image and segmented image respectively. The value of DC varies from 0 to 100%. With increase in overlapping pixels between these two images, the value of DC increases.

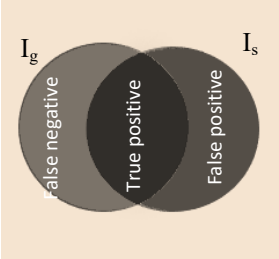

Figure C.2: Illustration of dice coefficient

The equation can be rewritten as follows to make it easy derivable from the confusion matrix,

$$\text{Dice coefficient DC} = \frac{2 \times (true\ positive)}{2 \times (true\ positive) + (false\ negative) + (false\ positive)} \times 100$$

References

[1] K. Than. (2012). World's Oldest Cave Art Found-Made by Neanderthals? Available: https://news.nationalgeographic.com/news/2012/06/120614-neanderthal-cave-paintings-spain-science-pike/
[2] B. Newhall, "The History of Photography, the Museum of Modern Art," New York, 1982.
[3] S. Mahajan, A. Das, and H. K. Sardana, "Image acquisition techniques for assessment of legume quality," Trends in Food Science & Technology, vol. 42, pp. 116-133, 2015.
[4] T. Voigt, U. Katscher, and O. Doessel, "Quantitative conductivity and permittivity imaging of the human brain using electric properties tomography," Magnetic Resonance in Medicine, vol. 66, pp. 456-466, 2011.
[5] M. Fuchs, M. Wagner, H.-A. Wischmann, K. Ottenberg, and O. Dössel, "Possibilities of functional brain imaging using a combination of MEG and MRT," in Oscillatory event-related brain dynamics, NATO ASI Series (Series A: Life Sciences), vol 271, pp. 435-457, 1994.
[6] R. Quain, A Dictionary of Medicine: Including General Pathology, General Therapeutics: D. Appleton and Company, 1883.
[7] B. Wedro. (2015). Head Injury (Brain Injury). Available: http://www.medicinenet.com/head_injury/article.htm
[8] A. Nehra and S. Bajpai, "Effectiveness of Cognitive Retraining After Brain Trauma—Case Studies," Activitas Nervosa Superior, vol. 54, pp. 139-145, 2012.
[9] K. Anand, "A clinical analysis of outcome in management of head injury in patients with highway road accidents," International journal of research in medical sciences, vol. 4, pp. 2079-2083, 2017.
[10] L. Li, X. Arakaki, T. Tran, M. Harrington, N. Padhye, and G. Zouridakis, "Brain activation profiles in mTBI: evidence from ERP activity of working memory response," in Engineering in Medicine and Biology Society, IEEE 38th Annual International Conference, 2016, pp. 1862-1865.
[11] Admin. (2014). Traumatic brain injury. Available: http://indianheadinjuryfoundation.org/traumatic-brain-injury/
[12] K. Rehana, S. A. Tabish, T. Gojwari, R. Ahmad, and H. Abdul, "Unit cost of CT scan and MRI at a large tertiary care teaching hospital in North India," Health, vol. 5, pp. 2059-2063, 2013.
[13] M. Al-Ayyoub, D. Alawad, K. Al-Darabsah, and I. Aljarrah, "Automatic detection and classification of brain hemorrhages," WSEAS Transactions on Computers, vol. 12, pp. 395-405, 2013.
[14] C. S. Anand and J. Sahambi, "MRI denoising using bilateral filter in redundant wavelet domain," in TENCON 2008. IEEE Region 10 Conference, 2008, pp. 1-6.
[15] H. P. Adams, G. Del Zoppo, M. J. Alberts, D. L. Bhatt, L. Brass, A. Furlan, et al., "Guidelines for the Early Management of Adults With Ischemic Stroke A Guideline From the American Heart Association/American Stroke Association Stroke Council, Clinical Cardiology Council, Cardiovascular Radiology and Intervention Council, and the Atherosclerotic Peripheral Vascular Disease and Quality of Care Outcomes in Research Interdisciplinary Working Groups: The American Academy of Neurology affirms the value of this guideline as an educational tool for neurologists," Circulation, vol. 115, pp. e478-e534, 2007.
[16] M. Chawla, S. Sharma, J. Sivaswamy, and L. Kishore, "A method for automatic detection and classification of stroke from brain CT images," in Engineering in Medicine and Biology Society, Annual International Conference of the IEEE, 2009, pp. 3581-3584.
[17] U. Balasooriya and M. S. Perera, "Intelligent brain hemorrhage diagnosis using artificial neural networks," in Business Engineering and Industrial Applications Colloquium, IEEE, 2012, pp. 128-133.
[18] Y. Li, Q. Hu, J. Wu, and Z. Chen, "A hybrid approach to detection of brain hemorrhage candidates from clinical head ct scans," in Fuzzy Systems and Knowledge Discovery, Sixth International Conference, 2009, pp. 361-365.
[19] R. M. Haralick, K. Shanmugam, and I. H. Dinstein, "Textural features for image classification," IEEE Transactions on systems, man, and cybernetics, vol. 3, pp. 610-621, 1973.

[20] M. M. Galloway, "Texture analysis using gray level run lengths," Computer graphics and image processing, vol. 4, pp. 172-179, 1975.
[21] J. Canny, "A computational approach to edge detection," IEEE Transactions on pattern analysis and machine intelligence, vol. 6, pp. 679-698, 1986.
[22] R. Deriche, "Optimal edge detection using recursive filtering," International Journal of Computer Vision, vol. 2, pp. 167-187, 1987.
[23] D. Marr and E. Hildreth, "Theory of edge detection," Proceedings of the Royal Society (B): Biological Sciences, vol. 207, pp. 187-217, 1980.
[24] B. Shahangian and H. Pourghassem, "Automatic brain hemorrhage segmentation and classification algorithm based on weighted grayscale histogram feature in a hierarchical classification structure," Biocybernetics and Biomedical Engineering, vol. 36, pp. 217-232, 2016.
[25] R. Ganesan and S. Radhakrishnan, "Segmentation of computed tomography brain images using genetic algorithm," International Journal of Soft Computing, vol. 4, pp. 157-161, 2009.
[26] A. Anand and H. Kaur, "Survey on Segmentation of Brain Tumor: A Review of Literature," International Journal of Advanced Research in Computer and Communication Engineering, vol. 5, pp. 79-82, 2016.
[27] Y. Huang and L. C. Parra, "Fully automated whole-head segmentation with improved smoothness and continuity, with theory reviewed," PloS one, vol. 10, p. e0125477, 2015.
[28] T. Chan, "Computer aided detection of small acute intracranial hemorrhage on computer tomography of brain," Computerized Medical Imaging and Graphics, vol. 31, pp. 285-298, 2007.
[29] F.-h. Tang, D. K. Ng, and D. H. Chow, "An image feature approach for computer-aided detection of ischemic stroke," Computers in biology and medicine, vol. 41, pp. 529-536, 2011.
[30] S. Shirgaonkar, D. H. Jeong, T. Huynh, and S.-Y. Ji, "Designing a robust bleeding detection method for brain CT image analysis," in Bioinformatics and Biomedicine Workshops, IEEE International Conference, 2012, pp. 260-264.
[31] A. Bardera, I. Boada, M. Feixas, S. Remollo, G. Blasco, Y. Silva, et al., "Semi-automated method for brain hematoma and edema quantification using computed tomography," Computerized Medical Imaging and Graphics, vol. 33, pp. 304-311, 2009.
[32] D. Cosic and S. Loucaric, "Computer system for quantitative: analysis of ICH from CT head images," in Engineering in Medicine and Biology Society, 19th Annual International Conference of the IEEE, 1997, pp. 553-556.
[33] W. Chen, R. Smith, S.-Y. Ji, K. R. Ward, and K. Najarian, "Automated ventricular systems segmentation in brain CT images by combining low-level segmentation and high-level template matching," BMC medical informatics and decision making, vol. 9, p. 1, 2009.
[34] Z. Wei, C. Zhang, X. Yang, and X. Zhang, "Segmentation of Brain Tumors in CT Images Using Level Sets," in International Symposium on Visual Computing, Springer, 2012, pp. 22-31.
[35] A. Neumann and C. Lorenz, "Statistical shape model based segmentation of medical images," Computerized Medical Imaging and Graphics, vol. 22, pp. 133-143, 1998.
[36] P. K. Sahoo, S. Soltani, and A. K. Wong, "A survey of thresholding techniques," Computer vision, graphics, and image processing, vol. 41, pp. 233-260, 1988.
[37] R. Pohle and K. D. Toennies, "Segmentation of medical images using adaptive region growing," in SPIE Medical Imaging, 2001, pp. 1337-1346.
[38] M. Del Fresno, M. Vénere, and A. Clausse, "A combined region growing and deformable model method for extraction of closed surfaces in 3D CT and MRI scans," Computerized Medical Imaging and Graphics, vol. 33, pp. 369-376, 2009.
[39] H. r. Wang, J. l. Yang, H. j. Sun, D. Chen, and X. l. Liu, "An improved region growing method for medical image selection and evaluation based on Canny edge detection," in Management and Service Science, International Conference, 2011, pp. 1-4.

[40] T. Gong, R. Liu, C. L. Tan, N. Farzad, C. K. Lee, B. C. Pang, et al., "Classification of CT brain images of head trauma," in Pattern Recognition in Bioinformatics, IAPR International Workshop, 2007, pp. 401-408.

[41] B. Liu, Q. Yuan, Z. Liu, X. Li, and X. Yin, "Automatic segmentation of intracranial hematoma and volume measurement," in Engineering in Medicine and Biology Society, 30th Annual International Conference of IEEE, 2008, pp. 1214-1217.

[42] N. Pérez, J. A. Valdés, M. A. Guevara, L. A. Rodríguez, and J. Molina, "Set of methods for spontaneous ICH segmentation and tracking from CT head images," in Iberoamerican Congress on Pattern Recognition, 2007, pp. 212-220.

[43] S. Loncaric, A. P. Dhawan, D. Cosic, D. Kovacevic, J. Broderick, and T. Brott, "Quantitative intracerebral brain hemorrhage analysis," in SPIE Medical Imaging, 1999, pp. 886-894.

[44] M. E. Brummer, "Hough transform detection of the longitudinal fissure in tomographic head images," IEEE Transactions on Medical Imaging, vol. 10, pp. 74-81, 1991.

[45] R. Guillemaud, P. Marais, A. Zisserman, B. McDonald, T. Crow, and M. Brady, "A three dimensional mid sagittal plane for brain asymmetry measurement," Schizophrenia Research, vol. 18, pp. 183-184, 1996.

[46] R. J. Davidson, "13 Cerebral Asymmetry, Emotion, and Affective Style," Brain asymmetry, p. 361, 1996.

[47] B. A. Ardekani, J. Kershaw, M. Braun, and I. Kanuo, "Automatic detection of the mid-sagittal plane in 3-D brain images," IEEE Transactions on Medical Imaging, vol. 16, pp. 947-952, 1997.

[48] Q. Hu and W. L. Nowinski, "A rapid algorithm for robust and automatic extraction of the midsagittal plane of the human cerebrum from neuroimages based on local symmetry and outlier removal," NeuroImage, vol. 20, pp. 2153-2165, 2003.

[49] A. Datta, A. Datta, and B. Biswas, "A fuzzy multilayer perceptron network based detection and classification of lobar intra-cerebral hemorrhage from computed tomography images of brain," in Recent Trends in Information Systems, International Conference, 2011, pp. 257-262.

[50] T. Hara, N. Matoba, X. Zhou, S. Yokoi, H. Aizawa, H. Fujita, et al., "Automated detection of extradural and subdural hematoma for contrast-enhanced CT images in emergency medical care," in SPIE Medical Imaging, 2007, pp. 651432(1)-651432(4).

[51] Y. Liu, N. A. Lazar, W. Rothfus, F. Dellaert, A. Moore, J. Schneider, et al. (2004). Semantic-based biomedical image indexing and retrieval. Available: https://www.researchgate.net/profile/Yanxi_Liu/publication/2916809_Semantic-based_Biomedical_Image_Indexing_and_Retrieval/links/00b4952588e192e1f9000000.pdf

[52] Y. Liu, W. E. Rothfus, and T. Kanade, "Content-based 3d neuroradiologic image retrieval: Preliminary results," in Content-Based Access of Image and Video Database, IEEE International Workshop, 1998, pp. 91-100.

[53] E. L. Yuh, A. D. Gean, G. T. Manley, A. L. Callen, and M. Wintermark, "Computer-aided assessment of head computed tomography (CT) studies in patients with suspected traumatic brain injury," Journal of neurotrauma, vol. 25, pp. 1163-1172, 2008.

[54] L. P. Clarke, R. P. Velthuizen, L. O. Hall, J. C. Bezdek, A. M. Bensaid, and M. L. Silbiger, "Comparison of supervised pattern recognition techniques and unsupervised methods for MRI segmentation," in SPIE Medical Imaging VI: Image Processing, 1992, pp. 668-677.

[55] H. Greenspan, B. van Ginneken, and R. M. Summers, "Guest editorial deep learning in medical imaging: Overview and future promise of an exciting new technique," IEEE Transactions on Medical Imaging, vol. 35, pp. 1153-1159, 2016.

[56] S. T. Kamble and M. Rathod, "Brain Tumor Segmentation using K-Means Clustering Algorithm," International Journal of Current Engineering and Technology, vol. 5, pp. 1521-1524, 2015.

[57] T. H. Lee, M. F. A. Fauzi, and R. Komiya, "Segmentation of CT brain images using K-means and EM clustering," in Computer Graphics, Imaging and Visualisation, Fifth International Conference, 2008, pp. 339-344.

[58] J. Bezdek, L. Hall, and L. Clarke, "Review of MR image segmentation techniques using pattern recognition," Medical Physics, vol. 20, pp. 1033-1048, 1993.

[59] D. C. Cheng and K. S. Cheng, "A PC-based medical image analysis system for brain CT hemorrhage area extraction," in Computer-Based Medical Systems, Proceedings of 11th IEEE Symposium, 1998, pp. 240-245.
[60] J. S. Lin, K. S. Cheng, and C. W. Mao, "A fuzzy Hopfield neural network for medical image segmentation," IEEE Transactions on Nuclear Science, vol. 43, pp. 2389-2398, 1996.
[61] K. S. Cheng, J. S. Lin, and C. W. Mao, "The application of competitive Hopfield neural network to medical image segmentation," IEEE Transactions on Medical Imaging, vol. 15, pp. 560-567, 1996.
[62] A. P. Dhawan, S. Loncaric, K. Hitt, J. Broderick, and T. Brott, "Image analysis and 3-d visualization of intracerebral brain hemorrhage," in Computer-Based Medical Systems, Proceedings of Sixth Annual IEEE Symposium, 1993, pp. 140-145.
[63] R. Liu, C. L. Tan, T.-Y. Leong, C. K. Lee, B. C. Pang, C. T. Lim, et al., "Hemorrhage slices detection in brain CT images," in International Conference on Pattern Recognition, 2008, pp. 1-4.
[64] S. Loncaric, D. Cosic, and A. Dhawan, "Hierarchical segmentation of CT images," in Medicine and Biology Society, 18th Annual International Conference of IEEE, 1996, pp. 736-737.
[65] S. Lončarić, D. Ćosić, and A. P. Dhawan, " Hierarchical Segmentation of CT Head Images," Engineering in Medicine and Biology Society, 18th Annual International Conference of the IEEE, 1996, pp. 736-737.
[66] T. Brosch, L. Y. Tang, Y. Yoo, D. K. Li, A. Traboulsee, and R. Tam, "Deep 3D convolutional encoder networks with shortcuts for multiscale feature integration applied to multiple sclerosis lesion segmentation," IEEE transactions on medical imaging, vol. 35, pp. 1229-1239, 2016.
[67] S. Pereira, A. Pinto, V. Alves, and C. A. Silva, "Brain tumor segmentation using convolutional neural networks in MRI images," IEEE transactions on medical imaging, vol. 35, pp. 1240-1251, 2016.
[68] F. C. Ghesu, E. Krubasik, B. Georgescu, V. Singh, Y. Zheng, J. Hornegger, et al., "Marginal space deep learning: efficient architecture for volumetric image parsing," IEEE transactions on medical imaging, vol. 35, pp. 1217-1228, 2016.
[69] A. Kalinovskya, V. Liauchuka, and A. Tarasaub, "Lesion Detection in CT Images Using Deep Learning Semantic Segmentation Technique," ISPRS-International Archives of the Photogrammetry, Remote Sensing and Spatial Information Sciences, pp. 13-17, 2017.
[70] D. Ravì, C. Wong, F. Deligianni, M. Berthelot, J. Andreu-Perez, B. Lo, et al., "Deep learning for health informatics," IEEE journal of biomedical and health informatics, vol. 21, pp. 4-21, 2017.
[71] M. Dundar, Q. Kou, B. Zhang, Y. He, and B. Rajwa, "Simplicity of kmeans versus deepness of deep learning: A case of unsupervised feature learning with limited data," in Machine Learning and Applications, IEEE 14th International Conference, 2015, pp. 883-888.
[72] C. C. Liao, F. Xiao, J. M. Wong, and I. J. Chiang, "A knowledge discovery approach to diagnosing intracranial hematomas on brain CT: recognition, measurement and classification," in International conference on medical biometrics, 2008, pp. 73-82.
[73] P. Maduskar and M. Acharyya, "Automatic identification of intracranial hemorrhage in non-contrast CT with large slice thickness for trauma cases," in SPIE Medical Imaging, 2009, pp. 726011(1)-726011(8).
[74] C. W. Hsu and C. J. Lin, "A comparison of methods for multiclass support vector machines," IEEE transactions on Neural Networks, vol. 13, pp. 415-425, 2002.
[75] D. K. Srivastava, B. Sharma, and A. Singh, "Classification of Hematomas in Brain CT Images Using Support Vector Machine," in Information and Communication Technology for Sustainable Development, Springer, 2018, pp. 375-385.
[76] D. R. Chowdhury, M. Chatterjee, and R. Samanta, "An artificial neural network model for neonatal disease diagnosis," International Journal of Artificial Intelligence and Expert Systems (IJAE), vol. 2, pp. 96-106, 2011.

[77] R. Ramteke and Y. K. Monali, "Automatic medical image classification and abnormality detection using K-Nearest Neighbour," International Journal of Advanced Computer Research, vol. 2, pp. 190-196, 2012.
[78] H. Bhadauria, A. Singh, and M. Dewal, "An integrated method for hemorrhage segmentation from brain CT imaging," Computers & Electrical Engineering, vol. 39, pp. 1527-1536, 2013.
[79] Q. Hu, G. Qian, A. Aziz, and W. L. Nowinski, "Segmentation of brain from computed tomography head images," in Engineering in Medicine and Biology, 27th IEEE Annual Conference, 2006, pp. 3375-3378.
[80] C. C. Liao, F. Xiao, J. M. Wong, and I. J. Chiang, "Computer-aided diagnosis of intracranial hematoma with brain deformation on computed tomography," Computerized medical imaging and graphics, vol. 34, pp. 563-571, 2010.
[81] J. Mather, "2762-dicom-example-files," in MATLAB Digest article about DICOM, MRI, Ed., ed. internet: The MathWorks, Inc., November 2002
[82] E. Bullitt, "MRA," MRI, Insight-journal: MIDAS.
[83] C. D, "PCIR DICOM Images," CT, Internet Archive, 20-Mar-2015.
[84] D. R. Varma, "Managing DICOM images: Tips and tricks for the radiologist," The Indian journal of radiology & imaging, vol. 22, pp. 4-13, 2012.
[85] R. Liu, S. Li, C. L. Tan, B. C. Pang, C. T. Lim, C. K. Lee, et al., "Fast traumatic brain injury CT slice indexing via anatomical feature classification," in International Conference on Image Processing, 17th IEEE International Conference, 2010, pp. 4377-4380.
[86] P. Aggarwal, H. Sardana, and G. Jindal, "Content based medical image retrieval: Theory, gaps and future directions," Graphics, Vision and Image Processing Journal, vol. 9, pp. 27-37, 2009.
[87] R. Acharya, Y. E. Ng, and J. S. Suri, Image modeling of the human eye: Artech House, 2008.
[88] A. Oliva, "Gist of the scene," Neurobiology of attention, vol. 696, pp. 251-258, 2005.
[89] P. G. Schyns and A. Oliva, "From blobs to boundary edges: Evidence for time-and spatial-scale-dependent scene recognition," Psychological science, vol. 5, pp. 195-200, 1994.
[90] J. K. Wu, M. S. Kankanhalli, J.-H. Lim, and D. Hong, "Color Feature Extraction," Perspectives on Content-Based Multimedia Systems, pp. 49-67, 2000.
[91] M. J. Swain and D. H. Ballard, "Color indexing," International journal of computer vision, vol. 7, pp. 11-32, 1991.
[92] S. E. Umbaugh, Computer imaging: digital image analysis and processing: CRC press, 2005.
[93] M. Tkalcic and J. F. Tasic, “Colour spaces: perceptual, historical and applicational background”, Computer as a Tool, The IEEE Region 8, 2003, pp.304- 308.
[94] T. K. Shih, J.-Y. Huang, C.-S. Wang, J. C. Hung, and C.-H. Kao, "An intelligent content-based image retrieval system based on color, shape and spatial relations," Proceedings of National Science Council Republic Of China Part A Physical Science And Engineering, vol. 25, pp. 232-243, 2001.
[95] X. Y. Wang, Y. J. Yu, and H. Y. Yang, "An effective image retrieval scheme using color, texture and shape features," Computer Standards & Interfaces, vol. 33, pp. 59-68, 2011.
[96] K. Arora and A. K. Aggarwal, "Approaches for Image Database Retrieval Based on Color, Texture, and Shape Features," in Handbook of Research on Advanced Concepts in Real-Time Image and Video Processing, IGI Global, 2017, pp. 28-50.
[97] J. Pujari and P. Hiremath, "Content based image retrieval based on color texture and shape features using image and its complement," International Journal of Computer Science and Security, vol. 1, pp. 25-35, 2007.
[98] R. S. Choras, "Image feature extraction techniques and their applications for CBIR and biometrics systems," International journal of biology and biomedical engineering, vol. 1, pp. 6-16, 2007.
[99] A. Oliva and A. Torralba, "Modeling the shape of the scene: A holistic representation of the spatial envelope," International journal of computer vision, vol. 42, pp. 145-175, 2001.
[100] A. Oliva and A. Torralba, "Building the gist of a scene: The role of global image features in recognition," Progress in brain research, vol. 155, pp. 23-36, 2006.

[101] D. G. Lowe, "Distinctive image features from scale-invariant keypoints," International journal of computer vision, vol. 60, pp. 91-110, 2004.
[102] H. Bay, A. Ess, T. Tuytelaars, and L. Van Gool, "Speeded-up robust features (SURF)," Computer vision and image understanding, vol. 110, pp. 346-359, 2008.
[103] M. Heikkilä, M. Pietikäinen, and C. Schmid, "Description of interest regions with local binary patterns," Pattern recognition, vol. 42, pp. 425-436, 2009.
[104] Z. Guo, L. Zhang, and D. Zhang, "A completed modeling of local binary pattern operator for texture classification," IEEE Transactions on Image Processing, vol. 19, pp. 1657-1663, 2010.
[105] S. Leutenegger, M. Chli, and R. Y. Siegwart, "BRISK: Binary robust invariant scalable keypoints," in Computer Vision, IEEE International Conference, 2011, pp. 2548-2555.
[106] J. Matas, O. Chum, M. Urban, and T. Pajdla, "Robust wide-baseline stereo from maximally stable extremal regions," Image and vision computing, vol. 22, pp. 761-767, 2004.
[107] A. Alahi, R. Ortiz, and P. Vandergheynst, "Freak: Fast retina keypoint," in Computer vision and pattern recognition, IEEE conference, 2012, pp. 510-517.
[108] B. Zhang, Y. Gao, S. Zhao, and J. Liu, "Local derivative pattern versus local binary pattern: face recognition with high-order local pattern descriptor," IEEE transactions on image processing, vol. 19, pp. 533-544, 2010.
[109] S. Murala, R. Maheshwari, and R. Balasubramanian, "Local tetra patterns: a new feature descriptor for content-based image retrieval," IEEE Transactions on Image Processing, vol. 21, pp. 2874-2886, 2012.
[110] L. Weisi, D. Tao, J. Kacprzyk, Z. Li, E. Izquierdo, and H. Wang, Multimedia analysis, processing and communications, vol. 346, Springer Science & Business Media, 2011.
[111] A. K. Jain and A. Vailaya, "Image retrieval using color and shape," Pattern recognition, vol. 29, pp. 1233-1244, 1996.
[112] K. Pearson, "X. Contributions to the mathematical theory of evolution.—II. Skew variation in homogeneous material," Phil. Trans. R. Soc. Lond. A, vol. 186, pp. 343-414, 1895.
[113] M. Flickner, H. Sawhney, W. Niblack, J. Ashley, Q. Huang, B. Dom, et al., "Query by image and video content: The QBIC system," computer, vol. 28, pp. 23-32, 1995.
[114] P. C. Chen and T. Pavlidis, "Segmentation by texture using a co-occurrence matrix and a split-and-merge algorithm," Computer graphics and image processing, vol. 10, pp. 172-182, 1979.
[115] A. S. Solberg and A. K. Jain, "Texture fusion and feature selection applied to SAR imagery," IEEE Transactions on Geoscience and Remote Sensing, vol. 35, pp. 475-479, 1997.
[116] G. Pass and R. Zabih, "Histogram refinement for content-based image retrieval," in Applications of Computer Vision, 3rd IEEE Workshop, 1996, pp. 96-102.
[117] J. Huang, S. R. Kumar, M. Mitra, W.-J. Zhu, and R. Zabih, "Image indexing using color correlograms," in Computer Vision and Pattern Recognition, IEEE Computer Society Conference, 1997, pp. 762-768.
[118] M. Subrahmanyam, Q. J. Wu, R. Maheshwari, and R. Balasubramanian, "Modified color motif co-occurrence matrix for image indexing and retrieval," Computers & Electrical Engineering, vol. 39, pp. 762-774, 2013.
[119] D. Tegolo, "Shape Analysis for Image Retrieval," in Storage and Retrieval for Image and Video Databases, 1994, pp. 59-69.
[120] D. Zhang and G. Lu, "Review of shape representation and description techniques," Pattern recognition, vol. 37, pp. 1-19, 2004.
[121] T. Chang and C.-C. Kuo, "Texture analysis and classification with tree-structured wavelet transform," IEEE Transactions on image processing, vol. 2, pp. 429-441, 1993.
[122] A. Materka and M. Strzelecki, "Texture analysis methods–a review," Technical university of lodz, institute of electronics, COST B11 report, Brussels, pp. 9-11, 1998.
[123] G. Castellano, L. Bonilha, L. Li, and F. Cendes, "Texture analysis of medical images," Clinical radiology, vol. 59, pp. 1061-1069, 2004.
[124] R. Bala, "Survey on Texture Feature Extraction Methods," International Journal of Engineering Science, vol. 7, pp. 10375-10377, 2017.

[125] G. Srinivasan and G. Shobha, "Statistical texture analysis," in Proceedings of world academy of science, engineering and technology, 2008, pp. 1264-1269.
[126] M. Kolekar, S. Talbar, and T. Sontakke, "Texture segmentation using fractal signature," IETE Journal of Research, vol. 46, pp. 319-323, 2000.
[127] A. K. Tiwari, V. Kanhangad, and R. B. Pachori, "Histogram refinement for texture descriptor based image retrieval," Signal Processing: Image Communication, vol. 53, pp. 73-85, 2017.
[128] I. Biederman, "Human image understanding: Recent research and a theory," Computer vision, graphics, and image processing, vol. 32, pp. 29-73, 1985.
[129] R. Srinivasan, Engineering materials and metallurgy: Tatas McGraw Hill Education Private Limited, 2010.
[130] stockphoto, "Free High Quality Photos Pexels.," Available: https://www.pexels.com, CC0 Public Domain.
[131] L. He, X. Ren, Q. Gao, X. Zhao, B. Yao, and Y. Chao, "The connected-component labeling problem: A review of state-of-the-art algorithms," Pattern Recognition, vol. 70, pp. 25-43, 2017.
[132] L. Cabaret, L. Lacassagne, and L. Oudni, "A review of world's fastest connected component labeling algorithms: Speed and energy estimation," in Conference on Design and Architectures for Signal and Image Processing, IEEE, 2014, pp. 1-6.
[133] R. F. Moghaddam and M. Cheriet, "AdOtsu: An adaptive and parameterless generalization of Otsu's method for document image binarization," Pattern Recognition, vol. 45, pp. 2419-2431, 2012.
[134] Unsplash, "coast-sea-marine-ocean-beach-1149735," Available: pixabay.com, CC0 Public Domain.
[135] Spotmatik, "Aerial view Kerid Crater Lake an extinct volcano Iceland," Available: http://cdn6.dissolve.com, CC0 Public Domain.
[136] F. E. Boas and D. Fleischmann, "CT artifacts: causes and reduction techniques," Imaging in Medicine, vol. 4, pp. 229-240, 2012.
[137] C. Ee, K. Sim, V. Teh, and F. Ting, "Estimation of window width setting for CT scan brain images using mean of greyscale level to standard deviation ratio," in Robotics, Automation and Sciences, International Conference, 2016, pp. 1-6.
[138] P. R. Ros and K. J. Mortele, CT and MRI of the abdomen and pelvis: a teaching file: Lippincott Williams & Wilkins, 2007.
[139] R. A. Zimmerman, W. A. Gibby, and R. F. Carmody, Neuroimaging: clinical and physical principles: Springer Science & Business Media, 2012.
[140] T. Malathi and M. K. Bhuyan, "Asymmetric occlusion detection using linear regression and weight-based filling for stereo disparity map estimation," IET Computer Vision, vol. 10, pp. 679-688, 2016.
[141] K. Somasundaram and P. Kalavathi, "Contour-based brain segmentation method for magnetic resonance imaging human head scans," Journal of computer assisted tomography, vol. 37, pp. 353-368, 2013.
[142] S. A. Kabara, Gabbouj, M. , Dastidar, P. , Cheikh, F.A. , Ryymin, P. , Laasonen, E. , "CT image texture analysis of intracerebral hemorrhage," in Finnish Signal Processing Symposium, 2003, pp. 190-194.
[143] A. R. Fallahi, M. Pooyan, and H. Khotanlou, "A new approach for classification of human brain CT images based on morphological operations," Journal of Biomedical Science and Engineering, vol. 3, pp. 78-82, 2010.
[144] M. M. Kyaw, "Computer-Aided Detection system for Hemorrhage contained region," International Journal of Computational Science and Information Technology, vol. 1, pp. 11-16, 2013.
[145] A. H. Ali, S. I. Abdulsalam, and I. S. Nema, "Detection and Segmentation of Hemorrhage Stroke using Textural Analysis on Brain CT Images," International Journal of Soft Computing and Engineering (IJSCE), pp. 2231-2307, 2015.

[146] V. B. Padole, "An Efficient Method for Detection of Brain Tumor in MRI Images," International Journal of Advanced Research in Computer Engineering & Technology (IJARCET), vol. 3, pp. 679-682, 2014.
[147] V. Chandran, D. Kumar, P. Geetha, and R. Nidhya, "Deep Learning Neural Network with Semi supervised Segmentation for Predicting Retinal and Cancer Cell Diseased Images," International Journal of Advanced Research in Computer Engineering & Technology (IJARCET), vol. 3, pp. 1280-1285, 2014.
[148] D. Liu and J. Yu, "Otsu method and K-means," in Hybrid Intelligent Systems 2009, Ninth International Conference, 2009, pp. 344-349.
[149] Y. G. Jung, M. S. Kang, and J. Heo, "Clustering performance comparison using K-means and expectation maximization algorithms," Biotechnology & Biotechnological Equipment, vol. 28, pp. S44-S48, 2014.
[150] F. Afrin, M. Al-Amin, and M. Tabassum, "Comparative Performance Of Using PCA With K-Means And Fuzzy C Means Clustering For Costomer Segmentation," International Journal Of Scientific & Technology Research, vol. 4, pp. 70-74, 2015.
[151] B. Shahangian and H. Pourghassem, "Automatic brain hemorrhage segmentation and classification in CT scan images," in Machine Vision and Image Processing, 8th Iranian Conference, 2013, pp. 467-471.
[152] K. E. Saatman, A.-C. Duhaime, R. Bullock, A. I. Maas, A. Valadka, and G. T. Manley, "Classification of traumatic brain injury for targeted therapies," Journal of neurotrauma, vol. 25, pp. 719-738, 2008.
[153] Y. Chang, D. Kumar, and N. Mahalingam, "Data compression for image recognition," in Speech and Image Technologies for Computing and Telecommunications, TENCON'97 IEEE Region 10 Annual Conference, 1997, pp. 399-402.
[154] D. ping Tian, "A review on image feature extraction and representation techniques," International Journal of Multimedia and Ubiquitous Engineering, vol. 8, pp. 385-396, 2013.
[155] L. Gool, P. Dewaele, and A. Oosterlinck, "Texture analysis anno 1983," Computer vision, graphics, and image processing, vol. 29, pp. 336-357, 1985.
[156] S. Roy, S. Nag, S. K. Bandyopadhyay, D. Bhattacharyya, and T.-H. Kim, "Automated brain hemorrhage lesion segmentation and classification from mr image using an innovative composite method," Journal of Theoretical & Applied Information Technology, vol. 78, pp. 34-45, 2015.
[157] G. Singh, A. Jati, A. Khasnobish, S. Bhattacharyya, A. Konar, D. Tibarewala, et al., "Object shape recognition from tactile images using regional descriptors," in Nature and Biologically Inspired Computing, 2012 Fourth World Congress, 2012, pp. 53-58.
[158] A. C. Phan, V. Q. Vo, and T. C. Phan, "Automatic Detection and Classification of Brain Hemorrhages," in Asian Conference on Intelligent Information and Database Systems, 2018, pp. 417-427.